

This is the accepted manuscript made available via CHORUS. The article has been published as:

Measurement of parity-violating asymmetry in electron-deuteron inelastic scattering

D. Wang *et al.* (The PVDIS Collaboration)

Phys. Rev. C **91**, 045506 — Published 16 April 2015

DOI: [10.1103/PhysRevC.91.045506](https://doi.org/10.1103/PhysRevC.91.045506)

Measurement of Parity-Violating Asymmetry in Electron-Deuteron Inelastic Scattering

(The PVDIS Collaboration)

D. Wang,¹ K. Pan,² R. Subedi,^{1,*} Z. Ahmed,³ K. Allada,⁴ K. A. Aniol,⁵ D. S. Armstrong,⁶ J. Arrington,⁷ V. Bellini,⁸ R. Beminiwattha,⁹ J. Benesch,¹⁰ F. Benmokhtar,^{11,†} W. Bertozzi,² A. Camsonne,¹⁰ M. Canan,¹² G. D. Cates,¹ J.-P. Chen,¹⁰ E. Chudakov,¹⁰ E. Cisbani,¹³ M. M. Dalton,¹ C. W. de Jager,^{10,1} R. De Leo,¹⁴ W. Deconinck,^{2,‡} X. Deng,¹ A. Deur,¹⁰ C. Dutta,⁴ L. El Fassi,¹⁵ J. Erler,¹⁶ D. Flay,¹⁷ G. B. Franklin,¹¹ M. Friend,¹¹ S. Frullani,¹³ F. Garibaldi,¹³ S. Gilad,² A. Giusa,⁸ A. Glamazdin,¹⁸ S. Golge,¹² K. Grimm,¹⁹ K. Hafidi,⁷ J.-O. Hansen,¹⁰ D. W. Higinbotham,¹⁰ R. Holmes,³ T. Holmstrom,²⁰ R. J. Holt,⁷ J. Huang,² C. E. Hyde,^{12,21} C. M. Jen,³ D. Jones,¹ Hoyoung Kang,²² P. M. King,⁹ S. Kowalski,² K. S. Kumar,²³ J. H. Lee,^{6,9} J. J. LeRose,¹⁰ N. Liyanage,¹ E. Long,²⁴ D. McNulty,^{23,§} D. J. Margaziotis,⁵ F. Meddi,²⁵ D. G. Meekins,¹⁰ L. Mercado,²³ Z.-E. Meziani,¹⁷ R. Michaels,¹⁰ M. Mihovilovic,^{26,¶} N. Muangma,² K. E. Mesick,^{27,**} S. Nanda,¹⁰ A. Narayan,²⁸ V. Nelyubin,¹ Nuruzzaman,²⁸ Y. Oh,²² D. Parno,¹¹ K. D. Paschke,¹ S. K. Phillips,²⁹ X. Qian,³⁰ Y. Qiang,³⁰ B. Quinn,¹¹ A. Rakhman,³ P. E. Reimer,⁷ K. Rider,²⁰ S. Riordan,¹ J. Roche,⁹ J. Rubin,⁷ G. Russo,⁸ K. Saenboonruang,^{1,††} A. Saha,^{10,‡‡} B. Sawatzky,¹⁰ A. Shahinyan,³¹ R. Silwal,¹ S. Širca,^{32,26} P. A. Souder,³ R. Suleiman,¹⁰ V. Sulkosky,² C. M. Suter,⁸ W. A. Tobias,¹ G. M. Urciuoli,²⁵ B. Waidyawansa,⁹ B. Wojtsekhowski,¹⁰ L. Ye,³³ B. Zhao,⁶ and X. Zheng¹

¹University of Virginia, Charlottesville, Virginia 22904, USA

²Massachusetts Institute of Technology, Cambridge, Massachusetts 02139, USA

³Syracuse University, Syracuse, New York 13244, USA

⁴University of Kentucky, Lexington, Kentucky 40506, USA

⁵California State University, Los Angeles, Los Angeles, California 90032, USA

⁶College of William and Mary, Williamsburg, Virginia 23187, USA

⁷Physics Division, Argonne National Laboratory, Argonne, Illinois 60439, USA

⁸Istituto Nazionale di Fisica Nucleare, Dipt. di Fisica dell'Univ. di Catania, I-95123 Catania, Italy

⁹Ohio University, Athens, Ohio 45701, USA

¹⁰Thomas Jefferson National Accelerator Facility, Newport News, Virginia 23606, USA

¹¹Carnegie Mellon University, Pittsburgh, Pennsylvania 15213, USA

¹²Old Dominion University, Norfolk, Virginia 23529, USA

¹³INFN, Sezione di Roma, gruppo Sanità and Istituto Superiore di Sanità, I-00161 Rome, Italy

¹⁴Università di Bari, I-70126 Bari, Italy

¹⁵Rutgers, The State University of New Jersey, Newark, New Jersey 07102, USA^{§§}

¹⁶Instituto de Física, Universidad Nacional Autónoma de México, 04510 México D.F., Mexico

¹⁷Temple University, Philadelphia, Pennsylvania 19122, USA^{¶¶}

¹⁸Kharkov Institute of Physics and Technology, Kharkov 61108, Ukraine

¹⁹Louisiana Technical University, Ruston, Louisiana 71272, USA

²⁰Longwood University, Farmville, Virginia 23909, USA

²¹Clermont Université, Université Blaise Pascal, CNRS/IN2P3, Laboratoire de Physique Corpusculaire, FR-63000 Clermont-Ferrand, France

²²Seoul National University, Seoul 151-742, South Korea

²³University of Massachusetts Amherst, Amherst, Massachusetts 01003, USA

²⁴Kent State University, Kent, Ohio 44242, USA

²⁵INFN, Sezione di Roma and Sapienza - Università di Roma, I-00161 Rome, Italy

²⁶Jožef Stefan Institute, SI-1000 Ljubljana, Slovenia

²⁷George Washington University, Washington, District of Columbia 20052, USA

²⁸Mississippi State University, Starkeville, Mississippi 39762, USA

²⁹University of New Hampshire, Durham, New Hampshire 03824, USA

³⁰Duke University, Durham, North Carolina 27708, USA

³¹Yerevan Physics Institute, Yerevan 0036, Armenia

³²University of Ljubljana, SI-1000 Ljubljana, Slovenia

³³China Institute of Atomic Energy, Beijing, 102413, P. R. China

(Dated: March 18, 2015)

The parity-violating asymmetries between a longitudinally-polarized electron beam and an unpolarized deuterium target have been measured recently. The measurement covered two kinematic points in the deep inelastic scattering region and five in the nucleon resonance region. We provide here details of the experimental setup, data analysis, and results on all asymmetry measurements including parity-violating electron asymmetries and those of inclusive pion production and beam-normal asymmetries. The parity-violating deep-inelastic asymmetries were used to extract the electron-quark weak effective couplings, and the resonance asymmetries provided the first evidence for quark-hadron duality in electroweak observables. These electron asymmetries and their interpretation were published earlier, but are presented here in more detail.

I. PHYSICS MOTIVATION

Parity symmetry implies that the physics laws behind a system remain the same when the system undergoes a space-reversal (parity) transformation. A simplified version of such transformation, in which only one dimension is reversed, mimics a mirror reflection, and thus parity symmetry is often called mirror symmetry. Among all known interactions of nature, electromagnetic, strong, and gravitational forces respect parity symmetry, but the weak force does not, as first postulated by Lee and Yang [1], and verified experimentally in nuclear β -decay by Wu *et al.* [2], in 1957.

For spin-1/2 elementary particles (elementary fermions), the standard scheme to describe how they violate parity symmetry is to use their chirality, an abstract concept defined by the γ^5 Dirac matrix, the chiral operator in quantum electrodynamics. In the ultra-relativistic limit or for massless particles, chirality becomes the experimentally accessible helicity: A particle is defined to be in a right(left)-handed helicity state, when its spin as defined by the right-hand rule is in the same (opposite) direction as its linear momentum. Since parity transformation changes a right-handed chiral state to left-handed and vice versa, parity violation implies that the fermion's weak charge must depend on the its chiral state. This feature is different from the electric charge for the electromagnetic interaction, the color charge for the strong nuclear force, and the energy-momentum tensor for gravity.

In the decade that followed the first observation of parity violation, many theories were proposed to explain this phenomenon. Among them is the Glashow-Weinberg-Salam (GWS) theory [3–5] of electroweak unification. In this theory, the charged-weak force behind β -decays only acts on left-handed spin-1/2 elementary particles (elementary fermions) and right-handed anti-fermions, thus violates parity to the maximal degree. The theory also predicted the existence of a new, neutral weak force carried by an electrically-neutral boson, the Z^0 . Unlike the W^\pm bosons that carry the charged-weak force, the Z^0 does interact with both chiral states of all fermions and anti-fermions. For neutral-weak interactions, the difference in the fermion's weak-interaction strengths between its left- and right-handed chiral states is described by the weak axial charge g_A , while the average of the two is called the weak vector charge g_V . In the GWS theory, g_A equals the particle's weak isospin T_3 : $g_A = T_3 = 1/2$ for up, charm, top quarks and neutrinos, and $-1/2$ for down, strange and bottom quarks and electrons; and g_V is related to the particle's T_3 and electric charge Q : $g_V = T_3 - 2Q \sin^2 \theta_W$, with θ_W the weak mixing angle, a parameter that describes how the electromagnetic interaction is unified with the weak force. Antiparticles have opposite weak isospin and electric charge, and thus opposite g_A and g_V as their particle counterparts. The fact that $g_A = \pm 1/2$ for elementary fermions implies that they all have a chirality preference in neutral-weak interactions.

The Z^0 was soon observed in the 1970's in both neutrino [6, 7] and electron scattering experiments [8, 9]. In electron scattering, parity violation is observed by a difference (an asymmetry) in the scattering cross sections between left- and right-handed electrons from an unpolarized target:

$$A_{PV} \equiv \frac{\sigma_R - \sigma_L}{\sigma_R + \sigma_L}. \quad (1)$$

In the most recent decades, parity-violating electron scattering (PVES) has been used primarily in the elastic scattering region. In elastic kinematic settings, the target nucleus remains whole during its interaction with the electron and the strong-interaction that binds quarks together to form the nucleon (or binds nucleons together to form the nucleus) is not disturbed. Elastic PVES asymmetry has been used to study the internal structure of the target that cannot be revealed through electromagnetic interactions. For example, elastic scattering from the proton and light nuclei has been used to study whether sea quarks contribute to the nucleon's structure, that is, whether the strange and the anti-strange quarks are distributed differently after their creation. Such nucleon strange form factor experiments have been carried out at many different facilities worldwide, such as the SAMPLE experiment [10–14] at MIT Bates, the A4 experiment at MAMI/Mainz [15–17], the HAPPEX experiments [18–23] in JLab Hall A, and the G0 experiment [24–26] in JLab Hall C. In the recent PREX experiment [27, 28], elastic scattering from ^{208}Pb has confirmed a difference in the spatial distributions between protons and neutrons inside this heavy nucleus.

On the other hand, of particular value to testing the Standard Model is the so-called deep inelastic scattering (DIS) regime, where the energy and momentum transferred from the electron to the target are so high that the quarks are probed directly, and that the strong interaction among quarks become negligible due to the so-called “asymptotic freedom” phenomenon. The

*now at Richland College, Dallas County Community College District, Dallas, Texas 75243, USA.

†now at Duquesne University, Pittsburgh, Pennsylvania 15282, USA.

‡now at College of William and Mary, Williamsburg, Virginia 23187, USA

§now at Idaho State University, Pocatello, Idaho 83201, USA.

¶Institut für Kernphysik, Johannes Gutenberg-Universität Mainz, DE-55099 Mainz, Germany

**now at Rutgers, The State University of New Jersey, Newark, New Jersey 07102, USA.

††now at Kasetsart University, Bangkok 10900, Thailand.

‡‡deceased.

§§now at Mississippi State University, Starkville, Mississippi 39762, USA

¶¶now at University of Massachusetts, Amherst, Massachusetts 01003, USA

parity-violating deep inelastic scattering (PVDIS) asymmetry is determined by the effective electron-quark couplings C_{1q} and C_{2q} , weighted by kinematic factors and the well-determined DIS structure functions. In the Standard Model tree-level diagram, the C_{1q} , C_{2q} couplings are the product of the electron and quark weak charges: $C_{1q} = 2g_A^e g_V^q$ (the effective electron-quark AV coupling), and $C_{2q} = 2g_V^e g_A^q$ (the effective electron-quark VA coupling).

The first PVES experiment [8, 9], E122 at the Stanford Linear Accelerator Center (SLAC) by Prescott *et al.*, was performed in the DIS region and provided the first definitive measurement of the weak mixing angle $\sin^2 \theta_W$. The E122 results were in good agreement with predictions from the GWS-theory, establishing it as a cornerstone of the now Standard Model of particle physics. The thirty years that followed witnessed a vast amount of Standard-Model-test experiments. Among those that determine the weak charges of elementary particles, the most precise measurement of the electron weak charges came from PVES on an electron target [29, 30] that provided $C_{2e} = 2g_V^e g_A^e$. The best result on the effective electron-quark AV couplings C_{1q} is from a combination [31] of elastic PVES [18–26] and atomic parity violation experiments [32–35].

On the other hand, determination of the C_{2q} couplings from PVES is difficult: For elastic scattering, the asymmetry component sensitive to the quark chirality (spin) is not directly determined by the C_{2q} , but by the nucleon’s axial form factor G_A . Extracting C_{2q} from G_A [11–14] depends on hadronic models and is subject to large uncertainties in the radiative corrections. For DIS, the quark-chirality-dependent C_{2q} contribution to the PVDIS asymmetry is kinematically suppressed because of angular momentum conservation, similar to the way in which the quark-spin-dependent contribution to the unpolarized cross section is suppressed. The small value of g_V^e further reduces the C_{2q} contribution to the PVDIS asymmetry. Until the experiment reported here was carried out, the only direct data on C_{2q} were from SLAC E122.

In addition to DIS and elastic scattering, another kinematic region accessible in electron scattering is the nucleon resonance region. In this region, the nucleon is excited by the energy and momentum transferred from the electron, but the strong interaction among quarks is not negligible (unlike in DIS). The nucleon resonance region therefore provides a transition between the quark and gluon degrees of freedom of DIS to hadron degrees of freedom of elastic scattering. Inclusive measurements in the nucleon resonance region have demonstrated a remarkable feature called “quark-hadron duality”, first pointed out by Bloom and Gilman [36], in which the low-energy (few GeV) cross sections averaged over the energy intervals of the resonance structures resemble those measured at asymptotically high energies of DIS. Over the past decade, duality has been verified in the unpolarized structure functions F_2 and F_L at four-momentum-transfer-squared Q^2 values below 1 (GeV/c)² [37–41], in the proton spin asymmetry A_1^p down to $Q^2 = 1.6$ (GeV/c)² [42], in the spin structure function g_1 down to $Q^2 = 1.7$ – 1.8 (GeV/c)² [43, 44], in the helicity-dependent structure functions $H_{1/2,3/2}$ [45], and for charged pion electroproduction in semi-inclusive scattering [46]. It was speculated that duality is a universal feature of the quark-hadron transition that should be exhibited not only in electromagnetic interactions, but also in charged lepton scattering via the weak interactions [47], and perhaps other processes as well.

We report here details of a PVDIS experiment that was carried out at the Thomas Jefferson National Accelerator Facility (Jefferson Lab, or JLab) in 2009, JLab E08-011. During this experiment, PVES asymmetries on a deuterium target were measured at two DIS and five nucleon resonance kinematic settings. The precision of the DIS measurement was higher than that of E122, and the kinematics were optimized for the extraction of the C_{2q} couplings. The DIS asymmetry and the C_{2q} couplings, published in Ref. [48], improved over previous data by a factor of five. Data taken at resonance settings had larger uncertainties, but nevertheless provided the first PVES data covering the whole nucleon resonance region. The resonance asymmetry results, published in Ref. [49], provided the first observation of quark-hadron duality on parity-violating observables. In this archival paper we first review the formalism for PVDIS, the SLAC E122 experiment, then describe the new JLab experiment E08-011 including its apparatus, data analysis, and all systematic uncertainties. In addition to PVES asymmetries, we report asymmetry results on inclusive pion production, pair-production, and beam-normal asymmetries. Finally, we provide interpretations of the electron asymmetries in DIS and the nucleon resonance regions.

A. Formalism for Parity-Violation in Electron Inelastic Scattering

For inelastic electron scattering off a nucleon or nuclear target, the parity-violating asymmetry originates from the interference between photon- and Z^0 -exchanges from the electron to the target (Fig. 1). This asymmetry can be written as [50]

$$A_{PV} = -\frac{G_F Q^2}{4\sqrt{2}\pi\alpha(Q^2)} [a_1(x, Q^2)Y_1(x, y, Q^2) + a_3(x, Q^2)Y_3(x, y, Q^2)] , \quad (2)$$

where G_F is the Fermi constant, $\alpha(Q^2)$ is the fine structure constant, $y = \nu/E = (E - E')/E$ is the fractional energy loss of the electron with E and E' the incident and the scattered electrons’ energy, $Q^2 \equiv -q^2$ is the negative of the four-momentum transferred from the electron to the target q , squared:

$$Q^2 = 2EE'(1 - \cos \theta) \quad (3)$$

with θ the electron scattering angle. The Bjorken scaling variable x is defined as

$$x \equiv Q^2/(2M\nu) , \quad (4)$$

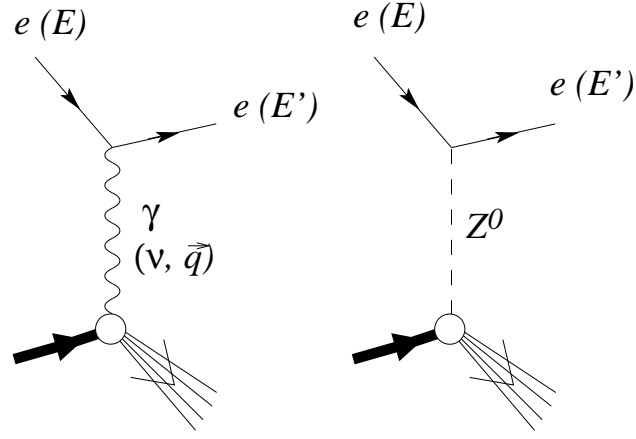


FIG. 1: The electron exchanges either a virtual photon (left) or a virtual Z^0 (right) with the target. The interference between these two processes leads to a parity-violating asymmetry between left- and right-handed electrons.

with M the proton mass. Another important variable is the invariant mass of the γ -nucleon (or Z^0 -nucleon) system, which for a fixed nucleon target is given by

$$W^2 = M^2 + 2M\nu - Q^2. \quad (5)$$

Typically, the region $M < W < 2 \text{ GeV}$ is the nucleon resonance region and $W > 2 \text{ GeV}$ corresponds to the DIS region.

The kinematic factors $Y_{1,3}$ are defined as

$$Y_1 = \left[\frac{1 + R^{\gamma Z}}{1 + R^\gamma} \right] \frac{1 + (1 - y)^2 - y^2 \left[1 - \frac{r^2}{1 + R^{\gamma Z}} \right] - xy \frac{M}{E}}{1 + (1 - y)^2 - y^2 \left[1 - \frac{r^2}{1 + R^\gamma} \right] - xy \frac{M}{E}} \quad (6)$$

and

$$Y_3 = \left[\frac{r^2}{1 + R^\gamma} \right] \frac{1 - (1 - y)^2}{1 + (1 - y)^2 - y^2 \left[1 - \frac{r^2}{1 + R^\gamma} \right] - xy \frac{M}{E}}, \quad (7)$$

where $r^2 = 1 + \frac{Q^2}{\nu^2}$, and $R^{\gamma(\gamma Z)}(x, Q^2)$ is the ratio of the longitudinal to transverse virtual photon electromagnetic absorption cross sections ($\gamma - Z^0$ interference cross sections). With some algebra, one can express the xyM/E term by r^2 and y^2 and Eqs.(6,7) change to (as in Ref. [51]):

$$Y_1 = \left[\frac{1 + R^{\gamma Z}}{1 + R^\gamma} \right] \frac{1 + (1 - y)^2 - \frac{y^2}{2} \left[1 + r^2 - \frac{2r^2}{1 + R^{\gamma Z}} \right]}{1 + (1 - y)^2 - \frac{y^2}{2} \left[1 + r^2 - \frac{2r^2}{1 + R^\gamma} \right]} \quad (8)$$

and

$$Y_3 = \left[\frac{r^2}{1 + R^\gamma} \right] \frac{1 - (1 - y)^2}{1 + (1 - y)^2 - \frac{y^2}{2} \left[1 + r^2 - \frac{2r^2}{1 + R^\gamma} \right]}. \quad (9)$$

To a good approximation $R^{\gamma Z}$ can be assumed to be equal to R^γ , resulting in $Y_1(x, y, Q^2) = 1$.

The $a_{1,3}$ terms in Eq. (2) are

$$a_1(x) = 2g_A^e \frac{F_1^{\gamma Z}}{F_1^\gamma}, \quad (10)$$

$$a_3(x) = g_V^e \frac{F_3^{\gamma Z}}{F_1^\gamma}, \quad (11)$$

where the structure functions, $F_{1,3}^{\gamma,\gamma Z}$, can be interpreted in the quark-parton model (QPM) in terms of the parton distribution functions (PDF) $q_i(x, Q^2)$ and $\bar{q}_i(x, Q^2)$ of the target:

$$F_1^\gamma(x, Q^2) = \frac{1}{2} \sum Q_{q_i}^2 [q_i(x, Q^2) + \bar{q}_i(x, Q^2)] , \quad (12)$$

$$F_1^{\gamma Z}(x, Q^2) = \sum Q_{q_i} g_V^i [q_i(x, Q^2) + \bar{q}_i(x, Q^2)] , \quad (13)$$

$$F_3^{\gamma Z}(x, Q^2) = 2 \sum Q_{q_i} g_A^i [q_i(x, Q^2) - \bar{q}_i(x, Q^2)] . \quad (14)$$

Here, Q_{q_i} denotes the quark's electric charge and the summation is over the quark flavors $i = u, d, s \dots$. Equations (11,14) show that the $a_3(x, Q^2)$ term involves the chirality of the quark (g_A^i) and therefore is suppressed by the kinematic factor Y_3 due to angular momentum conservation. It vanishes at the forward angle $\theta = 0$ or $y = 0$, and increases with θ or y at fixed x .

In most world parameterizations, it is common to fit the structure functions F_2 and R simultaneously to cross-section data. They are related through

$$F_2^{\gamma(\gamma Z)} = \frac{2x F_1^{\gamma(\gamma Z)} (1 + R^{\gamma(\gamma Z)})}{r^2} , \quad (15)$$

or equivalently:

$$F_1^{\gamma(\gamma Z)} = \frac{r^2 F_2^{\gamma(\gamma Z)}}{2x(1 + R^{\gamma(\gamma Z)})} . \quad (16)$$

In the QPM with the Bjorken scaling limit $Q^2 \rightarrow \infty$ at fixed x , the ratios $R^{\gamma(\gamma Z)}$ are zero, and $r = 1$. Hence one can construct the F_2 structure functions from PDFs as

$$F_2^\gamma(x) = 2x F_1^\gamma(x) = x \sum Q_{q_i}^2 [q_i(x) + \bar{q}_i(x)] , \quad (17)$$

$$F_2^{\gamma Z}(x) = 2x F_1^{\gamma Z}(x) = 2x \sum Q_{q_i} g_V^i [q_i(x) + \bar{q}_i(x)] . \quad (18)$$

Note that the use of the approximation $F_2 = 2x F_1$ does not affect the a_1 term of the asymmetry, since the extra terms r^2 and $2x$ in the numerator $F_1^{\gamma Z}$ and the denominator F_1^γ cancel.

For electron scattering, one defines the product of the electron and the quark weak couplings as the effective weak coupling constants $C_{1q,2q}$. In leading order of one-photon and one- Z^0 exchanges between the electron and the target (Fig. 1),

$$C_{1u} = 2g_A^e g_V^u , \quad C_{2u} = 2g_V^e g_A^u , \quad (19)$$

$$C_{1d} = 2g_A^e g_V^d , \quad C_{2d} = 2g_V^e g_A^d . \quad (20)$$

Using the appropriate electric charge and the weak isospin of quarks, they are related to the weak mixing angle θ_w as

$$C_{1u} = 2g_A^e g_V^u = 2 \left(-\frac{1}{2} \right) \left(\frac{1}{2} - \frac{4}{3} \sin^2 \theta_W \right) = -\frac{1}{2} + \frac{4}{3} \sin^2 \theta_W , \quad (21)$$

$$C_{2u} = 2g_V^e g_A^u = 2 \left(-\frac{1}{2} + 2 \sin^2 \theta_W \right) \left(\frac{1}{2} \right) = -\frac{1}{2} + 2 \sin^2 \theta_W , \quad (22)$$

$$C_{1d} = 2g_A^e g_V^d = 2 \left(-\frac{1}{2} \right) \left(-\frac{1}{2} + \frac{2}{3} \sin^2 \theta_W \right) = \frac{1}{2} - \frac{2}{3} \sin^2 \theta_W , \quad (23)$$

$$C_{2d} = 2g_V^e g_A^d = 2 \left(-\frac{1}{2} + 2 \sin^2 \theta_W \right) \left(-\frac{1}{2} \right) = \frac{1}{2} - 2 \sin^2 \theta_W . \quad (24)$$

In Standard-Model-test experiments, new physics that can be accessed by PVES asymmetries typically cannot be described by the one-boson exchange of Fig. 1 and Eq. (19-24) are no longer valid. In this case, one writes [91]

$$C_{1u} = g_{AV}^{eu} , \quad C_{2u} = g_{VA}^{eu} , \quad (25)$$

$$C_{1d} = g_{AV}^{ed} , \quad C_{2d} = g_{VA}^{ed} , \quad (26)$$

and the corresponding Feynman diagrams change from Fig. 1 to Fig. 2. The C_{1q}, C_{2q} couplings therefore provide information on new contact interactions beyond the Standard Model. Note that even though $C_{1,2}$ cannot be factorized into an electron and a target vertex, their chiral property remains the same.

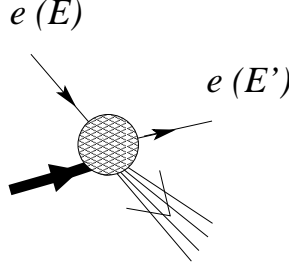


FIG. 2: Feynman diagram for contact interactions, used commonly to describe beyond-Standard-Model interactions.

The formalism of inelastic PV asymmetries, Eq. (2), can be simplified as follows: Defining $q_i^\pm(x) \equiv q_i(x) \pm \bar{q}_i(x)$, one has in the QPM

$$a_1(x) = 2 \frac{\sum C_{1i} Q_{q_i} q_i^+(x)}{\sum Q_{q_i}^2 q_i^+(x)}, \quad (27)$$

$$a_3(x) = 2 \frac{\sum C_{2i} Q_{q_i} q_i^-(x)}{\sum Q_{q_i}^2 q_i^+(x)}. \quad (28)$$

For an isoscalar target such as the deuteron, neglecting effects from charm and bottom quarks, and assuming $s = \bar{s}$, $c = \bar{c}$ and the isospin symmetry that $u^p = d^n$, $d^p = u^n$ [$u, d^{p(n)}$ are the up and down quark PDF in the proton (neutron)], the functions $a_{1,3}(x)$ simplify to

$$a_1(x) = \frac{6 [2C_{1u}(1 + R_C) - C_{1d}(1 + R_S)]}{5 + R_S + 4R_C}, \quad (29)$$

$$a_3(x) = \frac{6 (2C_{2u} - C_{2d}) R_V}{5 + R_S + 4R_C}, \quad (30)$$

where

$$R_C \equiv \frac{2(c + \bar{c})}{u + \bar{u} + d + \bar{d}}, \quad R_S \equiv \frac{2(s + \bar{s})}{u + \bar{u} + d + \bar{d}}, \quad \text{and} \quad R_V \equiv \frac{u - \bar{u} + d - \bar{d}}{u + \bar{u} + d + \bar{d}}. \quad (31)$$

The asymmetry then becomes

$$A_{PV} = \left(\frac{3G_F Q^2}{2\sqrt{2}\pi\alpha} \right) \frac{2C_{1u}[1 + R_C(x)] - C_{1d}[1 + R_S(x)] + Y_3(2C_{2u} - C_{2d})R_V(x)}{5 + R_S(x) + 4R_C(x)}. \quad (32)$$

The factor $Y_3 R_V$ is therefore crucial in accessing the C_{2q} .

If one neglects sea quarks completely ($R_C = R_S = 0$, $R_V = 1$), the deuteron becomes equal amount of up and down valence quarks only (the “valence quark only” picture). In this case no PDF is needed:

$$a_1(x) = \frac{6}{5} (2C_{1u} - C_{1d}), \quad a_3(x) = \frac{6}{5} (2C_{2u} - C_{2d}), \quad (33)$$

which lead to [52]

$$A_{PV} = \left(\frac{3G_F Q^2}{10\sqrt{2}\pi\alpha} \right) [(2C_{1u} - C_{1d}) + Y_3(2C_{2u} - C_{2d})]. \quad (34)$$

This expression can be used to estimate how the PDFs affect the interpretation of the asymmetry measurement.

B. Previous Data on Electron-Quark VA Coupling

The SLAC E122 experiment [8, 9] was the only PVDIS measurement before the present experiment. During the E122 experiment, a longitudinally polarized electron beam was scattered from 30-cm long unpolarized proton and deuteron targets

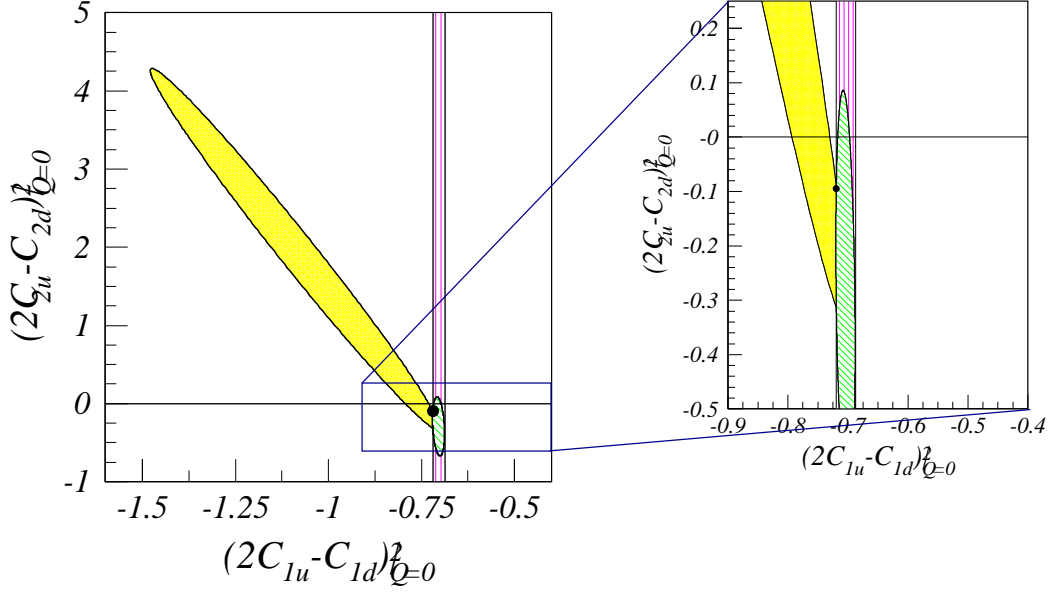


FIG. 3: (Color online) Previous data on C_{2q} , extrapolated to $Q^2 = 0$. The yellow ellipse represents a simultaneous fit to C_{1q} and C_{2q} using only the SLAC E122 asymmetries [9] re-analyzed using the latest PDF fits (see Appendix A). The magenta vertical band represents a fit to the best C_{1q} data [31], and the green ellipse the combined fit of the E122 asymmetries and the best C_{1q} . The right panel shows an enlarged view with the vertical and the horizontal axis at the same scale. The Standard Model value is shown as the black dot, where the size of the dot is for visibility.

at Q^2 values ranging from 1.05 to 1.91 $(\text{GeV}/c)^2$. Four beam energies: 16.2, 17.8, 19.4 and 22.2 GeV were used. Scattered electrons were collected in a magnetic spectrometer at 4° by integrating signals from a gas Cherenkov detector. Data from the two highest beam energies were published as [8] $A_{PV}/Q^2 = (-9.5 \pm 1.6) \times 10^{-5} (\text{GeV}/c)^{-2}$. The average y value was 0.21 and the average Q^2 was 1.6 $(\text{GeV}/c)^2$. The value of $\sin^2 \theta_W$ was extracted from the measured asymmetries. We re-analyzed the E122 kinematics [9] using the latest PDF fits (see Appendix A) and extracted the coupling combination $2C_{2u} - C_{2d}$ and $2C_{1u} - C_{1d}$ from their asymmetry results. These results are shown as the yellow ellipse in Fig. 3. Also shown in Fig. 3 is the most recent fit [31] to C_{1q} data from all elastic PVES and Cs atomic parity violation experiments. One can see that the uncertainty on the $2C_{2u} - C_{2d}$ is nearly two orders of magnitude larger than on $2C_{1u} - C_{1d}$.

II. APPARATUS

The experiment was performed in experimental Hall A at JLab. The floor plan for Hall A is shown schematically in Fig. 4. A $105\ \mu\text{A}$ longitudinally polarized electron beam was incident on a 20-cm long liquid deuterium target, and scattered electrons were detected by the two High Resolution Spectrometers (HRS) [53] in inclusive mode. A series of beam diagnostic devices was used to measure the beam energy, position, and current. A Luminosity Monitor was located downstream from the target to monitor target density fluctuation and possible false asymmetries. For DIS measurements the beam energy used was 6 GeV, the highest achievable with the continuous electron beam accelerator facility (CEBAF) of JLab before its 12 GeV Upgrade.

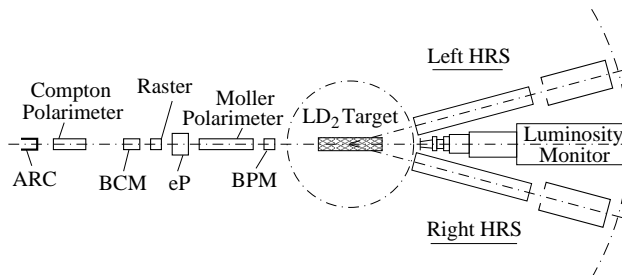


FIG. 4: Schematic floor plan of the 6 GeV PVDIS experiment in Hall A at JLab. The electron beam enters from the left, passes through a series of monitoring devices such as the ARC and the eP for energy measurement, Compton and Møller polarimeters for polarization measurement, the beam charge monitor (BCM) and the beam position monitor (BPM), then scatters from a liquid D_2 target in the middle of the hall. The scattered electrons were detected in the HRS pair in inclusive mode.

The experimental techniques for measuring small asymmetries of order 1 part per million (ppm) or less have been successfully used in the HAPPEX experiments [18–23] and the PREx [27] experiment in JLab Hall A. These two experiments had maintained systematic uncertainties associated with beam helicity reversal at the 10^{-8} level. The asymmetries sought for in this experiment were of order 10^2 ppm with required statistical accuracies at the $(3 - 4)\%$ level, which were two orders of magnitude larger than the systematic uncertainty established in the recent PVES experiments. The main challenge of the experiment was a reliable rejection of the large pion electro- and photo-production background (that is only present in inelastic scattering) while identifying electrons at high rates. While the standard HRS detector package and data acquisition (DAQ) system routinely provide high particle identification (PID) performance, they are based on full recording of the detector signals and are limited to event rates of 4 kHz. This is not sufficient for the few-hundred kHz rates expected for the present experiment. A new DAQ electronic system was built to count event rates up to 600 kHz with hardware-based particle identification. See Ref. [54] for a complete report on the DAQ design, its PID performance, deadtime effects, and the quality of the asymmetry measurement. The standard DAQ of the HRS will be referred to as the HRS DAQ hereafter.

The apparatus and its effect on the measured asymmetry are presented in this section. The polarized electron beam will be described first (section II A), followed by descriptions of the beam monitors (section II B), the beam polarimetry (section II C), the target system (section II D), and the spectrometers and detectors (section II E).

A. Polarized Electron Beam

The electron beam was produced from a strained superlattice GaAs/GaAsP photocathode illuminated by circularly polarized laser light [55]. The laser polarization is controlled by a Pockels cell. By reversing the high voltage on the Pockels cell, the sign of the laser circular polarization flips and the direction of the electron spin at the target is reversed every 33 ms [56]. These 33-ms periods are called “beam helicity windows” or simply “windows”. Data collected in the first 0.5 ms of each window are rejected to allow the Pockels cell to settle. During this experiment, the helicity of the electron beam was controlled by a helicity signal, and followed a quartet structure of either “RLLR” or “LRRL”, with each state lasting 33 ms and the first state of each quartet selected from a pseudorandom sequence [19–22]. The helicity signal was sent to the data acquisition system after being delayed by eight helicity states (two quartets). This delayed helicity sequence controlled the data collection. The helicity signal was line-locked to the 60 Hz line, thus ensuring a good cancellation of the power-line noise.

To reduce possible systematic errors, a half-wave plate (HWP) was inserted intermittently into the path of the polarized laser, which resulted in a reversal of the actual beam helicity while keeping the helicity signal sequence unchanged. Roughly equal statistics were accumulated with opposite HWP states for the measured asymmetry, which suppressed many systematic effects. The expected sign flips in the measured asymmetries between the two beam HWP configurations were observed.

The direction of the beam polarization could also be controlled by a Wien filter and solenoidal lenses near the injector [57].

After accelerating, the beam was directed into Hall A, where its intensity, energy and trajectory on target were inferred from the response of several monitoring devices. The beam monitors and the scattered electron trigger signals from the DAQ were integrated over the helicity window and digitized, from which raw cross-sectional asymmetries A^{raw} were formed, see section III A. To keep spurious beam-induced asymmetries under control at well below the ppm level, careful attention was given to the design and configuration of the laser optics leading to the photocathode. A specialized DAQ system (called the HAPPEX DAQ) [18–23] was used to provide feedback at the photocathode to minimize these beam asymmetries [56]. Measurement of the polarization of the beam will be described in section II C and the polarization results in section III D.

B. Beam Monitoring and Rastering

As a direct input to the asymmetry extraction, the beam intensity was measured by two microwave cavity Beam Current Monitors (BCMs) and an Unser monitor located 25 m upstream of the target [53]. In addition, helicity correlations in the beam properties such as energy and position could add systematic uncertainties and widen the uncertainty of A^{raw} , and thus are a primary concern for parity-violation experiments. At JLab, the beam position is measured by “stripline” monitors [58], each of which consists of a set of four thin wires placed symmetrically around the beam pipe. The wires act as antennae that provide a signal, modulated by the microwave structure of the electron beam, that is proportional to the beam position as well as intensity. Two such Beam Position Monitors (BPMs) are available in Hall A, located 7.524 m (BPMA) and 1.286 m (BPMB) upstream of the target center. Beam positions measured at BPMA and BPMB were extrapolated to provide the position and the incident angle at the target. An additional BPM (BPM12x) is available in the arc section of the beamline just before it enters the hall to monitor changes in the beam energy.

The electron beam at JLab has a nominal spot size of 100–200 μm (root-mean-square or rms value). To avoid over-heating the target, the beam is routinely moved at 20 kHz by a rastering system consists of two sets of steering magnets located 23 m upstream of the target. This fast rastering system can deliver beam with a uniform elliptical or rectangular distribution of size between 100 μm and several mm at the target. A square distribution of approximately $4 \times 4 \text{ mm}^2$ was used for this experiment. The exact correspondence between BPM signals and the actual beam position at the target varies with beam energy and must be calibrated. In addition, the BPM information is not fast enough to provide event-by-event information and the raster currents must be used to calculate real-time beam position on the target. Establishing the relation between BPM signals and beam positions, and between raster currents and the beam positions, is part of the BPM calibration described in section III E 1.

C. Beam Polarimetry

Three beam polarimetry techniques were available for the present experiment: a Mott polarimeter in the injector of the linac, and a Møller and a Compton polarimeter in Hall A. The Mott and the Møller measurements must be done separately from production data taking, while Compton measurements are non-intrusive. The Mott polarimeter [59–62] is located near the injector to the first linac where the electrons have reached 5 MeV in energy. During the beam normal asymmetry A_n measurement, it was used for setting up the transversely-polarized beam and verifying that the beam polarization was fully in the vertical direction. In the following we will describe the principle of only the Møller and Compton polarimeters. For production runs, since the Mott polarimeter measures only the polarization at the injector which can differ from the beam polarization in the experimental hall, its results were not used directly in our analysis.

1. Møller Polarimeter

A Møller polarimeter [53] measures the beam polarization via a measurement of the asymmetry in $\vec{e} - \vec{e}$ (Møller) scattering, which depends on the beam and target polarizations P^{beam} and $P_{\text{Møller}}^{\text{targ}}$, as well as on the Møller scattering analyzing power A_M^{th} :

$$A_M = \sum_{i=X,Y,Z} (A_{Mi}^{\text{th}} \cdot P_{i,\text{Møller}}^{\text{targ}} \cdot P_i^{\text{beam}}). \quad (35)$$

Here, $i = X, Y, Z$ defines the projections of the polarizations with Z parallel to the beam and OXZ the Møller scattering plane. The analyzing powers A_{Mi}^{th} depend on the scattering angle in the $\vec{e} - \vec{e}$ center-of-mass (CM) frame, θ_{CM} , and are calculable in QED. The longitudinal analyzing power is

$$A_{MZ}^{\text{th}} = -\frac{\sin^2 \theta_{\text{CM}} (7 + \cos^2 \theta_{\text{CM}})}{(3 + \cos^2 \theta_{\text{CM}})^2}. \quad (36)$$

The absolute value of A_{MZ}^{th} reaches a maximum of 7/9 at $\theta_{\text{CM}} = 90^\circ$. At this angle the transverse analyzing powers are $A_{MX}^{\text{th}} = -A_{MY}^{\text{th}} = A_{MZ}^{\text{th}}/7$.

The Møller polarimeter target was a ferromagnetic foil magnetized in a magnetic field of 24 mT along its plane. The target foil can be oriented at various angles in the horizontal plane, providing both longitudinal and transverse polarization measurements. The asymmetry was measured at two target angles ($\pm 20^\circ$) and the average taken, which cancels contributions from transverse components of the beam spin and thus reduces the uncertainties from target angle measurements. At a given target angle, two sets of measurements with oppositely-signed target polarizations were made which cancels some systematic effects such as those from beam current asymmetries. The Møller target polarization was approximately 8%.

The Møller-scattered electrons were detected in a magnetic spectrometer consisting of three quadrupoles and a dipole [53]. The spectrometer selects electrons in a range of $75^\circ \leq \theta_{\text{CM}} \leq 105^\circ$ and $-5^\circ \leq \phi_{\text{CM}} \leq 5^\circ$ where ϕ_{CM} is the azimuthal angle in the CM frame. The detector consisted of lead-glass calorimeter modules in two arms to detect the electrons in coincidence. The Møller measurements must be performed separately from production runs, and each measurement takes approximately 4 hours including setting up the magnets to direct the electron beam to the Møller target. The statistical uncertainty of the Møller measurements is negligible compared to the approximately 2% systematic error which is dominated by the uncertainty in the foil polarization.

2. Compton Polarimeter

The Compton polarimeter [53, 63–65] is based on scattering of the polarized electron beam from a polarized laser beam in a beam chicane. For this experiment, the beam polarization was extracted from the backscattered photon signals detected in a GSO ($\text{Gd}_2\text{SiO}_5\text{:Ce}$) crystal in the integrated mode [65]. Scattered electrons can be detected either in the inclusive mode or in coincidence with the backscattered photons, but electron detection was not used in this experiment.

The Compton asymmetry $A_C = (n_C^R - n_C^L)/(n_C^R + n_C^L)$ was measured, where $n_C^R(n_C^L)$ refers to the scattered photon counting rate for right (left) electron helicity normalized to the beam intensity. This asymmetry is related to the electron beam polarization via

$$P_e = \frac{A_C}{P_\gamma A_C^{\text{th}}}, \quad (37)$$

where P_γ is the photon polarization and A_C^{th} the Compton analyzing power. At typical JLab energies (a few GeV), the Compton cross-section asymmetry is only a few percent. To compensate for the small asymmetry, a Fabry-Perot cavity [66] was used to amplify the photon density from a standard low-power Nd:YAG laser ($\lambda = 1064$ nm) such that high statistics can be obtained within one to a few hours. An average power of 1200 W was accumulated inside the cavity with a photon beam waist of the order of $150 \mu\text{m}$ and a photon polarization above 99%, monitored online at the exit of the cavity [67]. When extracting the beam polarization from Compton data, a GEANT4-based simulation [68] was performed to reproduce the measured photon energy distribution and to extract the analyzing power. For the present experiment the systematic uncertainty of Compton measurement was approximately 1.92% relative and was dominated by the understanding of the analyzing power (1.75% relative) and the laser polarization (0.8% relative).

D. Target System

The Hall A cryogenic target system [53] was used for this experiment. We used a 20-cm long deuterium target cell for the main production data-taking. Solid targets were used for evaluating backgrounds, studying the spectrometer optics, and checking beam centering. The target cell and a solid target ladder sit in an evacuated cylindrical scattering chamber of 104 cm diameter, centered on the pivot for the spectrometers. Also located inside the scattering chamber were subsystems for cooling, temperature and pressure monitoring, target motion, gas-handling and controls. The scattering chamber was maintained under a 10^{-6} Torr (10^{-4} Pa) vacuum. The exit windows on the scattering chamber allowed scattered particles to reach the spectrometers. These windows were made of 0.406-mm thick Al foil.

Figure 5 shows a schematic diagram of the target ladder arrangement used during this experiment. Of the three cryogenic loops, only loop 1 was used for the liquid deuterium. It was operated at a temperature of 22 K and a pressure of 25 psia (1.7×10^5 Pa), leading to a density of about 0.1676 g/cm^3 . The diameter of the cell was 2.0 cm. The thicknesses of its walls and of the solid targets are summarized in Table I.

When using a fluid target for electron scattering, the energy deposit of the electron beam in the target can cause local density fluctuations. This will add noise to the measurement that cannot be improved by increasing statistics. This systematic effect, often called the “target boiling effect” although it is not related to an actual phase change of the target, was measured at the

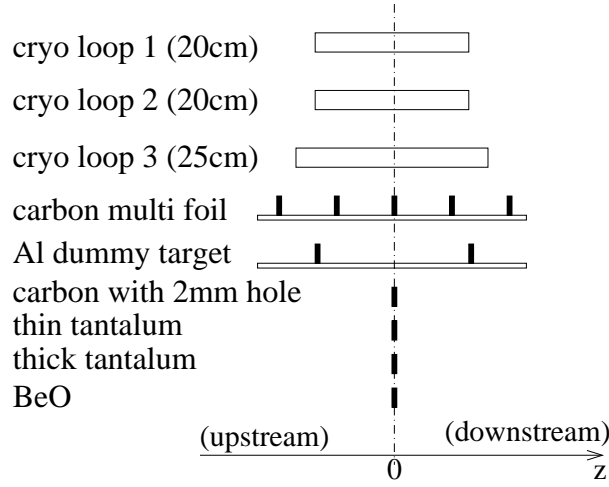


FIG. 5: Schematic diagram of the target ladder arrangement used during the experiment. The electron beam is along the horizontal direction (the z -axis) and is incident from the left on the target. The carbon multi foils were located at $z = (-15, -7.5, 0, 7.5, 15)$ cm and the Al dummy foils were located at $z = (-10, 10)$ cm. All other solid targets were located at $z = 0$ cm and were about 1 inch apart in the vertical direction.

Target	Position along z	Purity	Thickness
cryo-loop 1 ^a	Entrance window, -10 cm		$0.126 \pm 0.011 \pm 0.003$ mm ^c
	Exit window, +10 cm		$0.100 \pm 0.008 \pm 0.003$ mm
	Wall, beam left upstream		$0.313 \pm 0.008 \pm 0.003$ mm
	Wall, beam left middle		$0.317 \pm 0.002 \pm 0.003$ mm
	Wall, beam left downstream		$0.323 \pm 0.003 \pm 0.003$ mm
	Wall, beam right upstream		$0.340 \pm 0.002 \pm 0.003$ mm
	Wall, beam right middle		$0.336 \pm 0.007 \pm 0.003$ mm
	Wall, beam right downstream		$0.313 \pm 0.008 \pm 0.003$ mm
Carbon multi foil	$(-15, -7.5, 0, 7.5, 15)$ cm	99.5%	0.042 ± 0.001 g/cm ² (all foils)
Al Dummy ^{a, b}	-10 cm		0.359 ± 0.0003 g/cm ²
	+10 cm		0.367 ± 0.0003 g/cm ²
Carbon hole ^b	0 cm	99.95%	0.08388 ± 0.00012 g/cm ²
Tantalum Thin	0 cm	99.9%	0.021487 ± 0.000078 g/cm ²
Tantalum Thick	0 cm	99.9%	0.12237 ± 0.000341 g/cm ²
BeO	0 cm	99.0%	0.149 ± 0.001 g/cm ²

^a All aluminum used for the cryo-target and the Al Dummy are made from Al 7075 T-6 plates.

^b Both Al Dummy and Carbon Hole targets had a 2-mm hole to calibrate the target motion relative to the beam position.

^c The first error bar comes from the standard deviation of multiple measurements at different positions on the target, and the second error is from calibration of the instrument.

TABLE I: Position, material, and thickness of the target system used in this experiment. The position is defined along the beam direction with respect to the hall center, see Fig. 5.

beginning of the experiment for different beam transverse sizes and target cooling conditions (see section III C). During production data taking, the transverse size of the beam was controlled such that the boiling effect did not visibly widen the statistical uncertainty of the asymmetry measurement.

E. Spectrometers, Detectors, and DAQ

The Hall A high resolution spectrometers (HRS) are a pair of identical spectrometers whose magnet system each consists of one dipole and three focusing quadrupoles in a $Q_1 Q_2 D Q_3$ sequence [53]. The spectrometer and their standard detector package served to select for and to measure the kinematics quantities (E' , θ) while suppressing backgrounds originating from

the target. The spectrometers were designed to have a reasonable acceptance with excellent angle and momentum resolutions, high accuracy in the reconstructed kinematic variables of the events and precise normalization of the cross section.

Figure 6 shows a sideview of the HRS and its detector package. In each HRS, two layers of scintillators provide fast timing

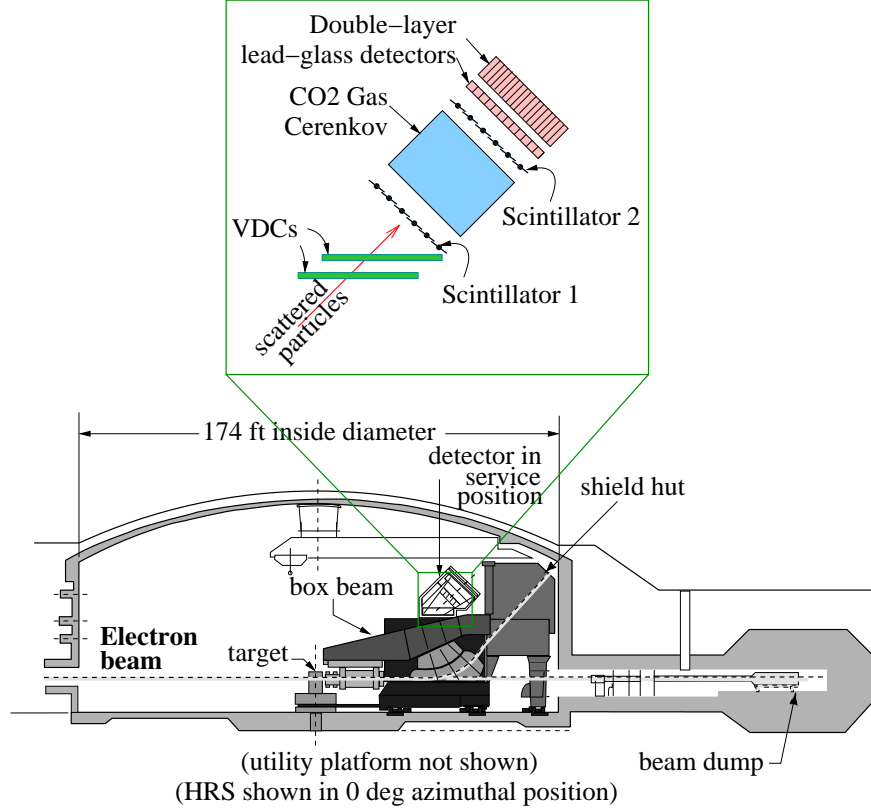


FIG. 6: (Color online) Bottom: Schematic diagram for the HRS in Hall A of JLab, figure taken from Ref. [53]. Top: Zoom-in view of the detector package in the HRS.

information of the scattered particles, vertical drift chambers (VDCs) provide tracking information, and a gas Cherenkov and a double-layered lead glass detector provide the particle identification (PID).

To achieve high resolution and accuracy in determining the event position, scattering angle and momentum, the HRS features an optics focusing system that can be described as a simple matrix operation between the original interaction point at the target $(x_{tg}, y_{tg}, \theta_{tg}, \phi_{tg})$ (in the target coordinate system [53, 69]) and the positions and angles of the particle detected at the focal plane (x, θ, y, ϕ) [53, 69], where the focal plane refers to the first of the four high-voltage wire planes of the VDC. This optics matrix varies with the beam energy and the spectrometer angle and momentum settings, and must be calibrated every time these conditions are changed. The optics calibration directly affects the determination of the Q^2 -values of the present experiment and will be described in Sec. III E.

The DAQ [54] of this experiment utilized signals from the two scintillator planes, the CO_2 gas Cherenkov counter and the double-layered lead glass detector. Both electron and pion triggers were formed. To better understand the counting deadtime of the DAQ, two sets of electronics were formed for each trigger, which were expected to differ only in the deadtime. These two sets of triggers will be referred to as the “narrow” and the “wide” paths, with the narrow path exhibiting less deadtime loss. The electron and pion triggers were sent to digital scalars where they were integrated over each helicity window of the electron beam. The standard tracking detector (the VDCs) was turned off during production data taking because it might not endure the expected high event rates. During low-rate calibration runs, the VDCs were turned on to study the efficiencies of the triggering detectors. Efficiencies of the electron and pion triggers, the background contamination in each trigger, and the counting loss due to deadtime were analyzed in detail and reported in Ref. [54].

III. DATA ANALYSIS

The experiment ran between October 26th and December 22nd, 2009. Data were taken first with a 6-GeV beam at two DIS settings at $Q^2 = 1.085$ and 1.901 (GeV/c)². These were the main production kinematics and will be referred to as DIS#1 and DIS#2, respectively. Due to limitations in the spectrometer magnets, DIS#1 was taken only on the Left HRS, while DIS#2 was taken on both Left and Right HRSs. A total of 1.02×10^7 beam helicity pairs were selected to form the final electron sample for $Q^2 = 1.085$ (GeV/c)², and 2.5×10^7 pairs for the $Q^2 = 1.901$ (GeV/c)² measurement. The statistical precision achieved was 3% at $Q^2 = 1.1$ (GeV/c)² and 4% at $Q^2 = 1.9$ (GeV/c)². The systematic uncertainty achieved was smaller than 3%.

Data were taken at five additional nucleon resonance settings to provide inputs for electromagnetic radiative corrections. Resonance setting IV was taken with the 6 GeV beam on the left HRS, between data taking of DIS#1 and #2. Setting V was taken over a short period before IV due to difficulties in rotating the HRS to the desired angle. It had low statistics and, with W greater than 2 GeV, was not strictly speaking in the resonance region. However we refer to it as setting RES V for convenience and present its result for completeness. Three more resonance settings (RES I, II and III) were taken with a 4.8 GeV beam at the end of the experiment, on either Left or Right HRS. For RES I which was taken on the left HRS only, the Q_1 and the dipole magnets were set at 4.00 GeV/c, but its Q_2 and Q_3 were limited to 3.66 GeV/c due to a power supply malfunction. Dedicated measurements for the beam transverse asymmetry – also called the normal asymmetry A_n – were carried out at DIS #1 and #2 in which the beam spin was directed fully perpendicular to the scattering plane. An overview of the beam energy and spectrometer settings for each kinematics, the observed scattered electron rate and the ratio of π^-/e rates is shown in Table II in chronological order.

HRS	Date	Kine#	E_b (GeV)	θ_0	E'_0 (GeV)	R_e (kHz)	R_π/R_e
Left	11/04-12/01/2009	DIS#1	6.0674	12.9°	3.66	≈ 210	≈ 0.5
	12/01-12/02/2009	A_n	6.0674	12.9°	3.66	≈ 210	≈ 0.5
	12/02/2009	RES V	6.0674	14°	3.66	≈ 130	< 0.7
	12/03/2009	RES IV	6.0674	15°	3.66	≈ 80	< 0.6
	12/04-12/17/2009	DIS#2	6.0674	20.0°	2.63	≈ 18	≈ 3.3
	12/17-12/19/2009	RES I	4.8674	12.9°	4.0	≈ 300	< 0.25
	12/19-12/22/2009	RES II	4.8674	12.9°	3.55	≈ 600	< 0.25
Right	11/04-12/01/2009	DIS#2	6.0674	20.0°	2.63	≈ 18	≈ 3.3
	12/01-12/02/2009	A_n	6.0674	20.0°	2.63	≈ 18	≈ 3.3
	12/02-12/17/2009	DIS#2	6.0674	20.0°	2.63	≈ 18	≈ 3.3
	12/17-12/22/2009	RES III	4.8674	12.9°	3.1	≈ 400	< 0.4

TABLE II: Overview of kinematics settings of this experiment and the observed scattered electron rate R_e and the charged pion to electron rate ratio R_π/R_e . The kinematics include the beam energy E_b , and the spectrometer central angle θ_0 and central momentum E'_0 . Measurement of the transverse asymmetry A_n was performed at the production DIS settings on December 1-2. For RES#I which was taken on the left HRS only, the Q_1 and the dipole magnets were set at 4.00 GeV/c, but its Q_2 and Q_3 were limited to 3.66 GeV/c due to a power supply malfunction. The electron rate R_e was obtained directly from the DAQ, while the pion rate was the rate recorded by the DAQ corrected for trigger efficiency and background contamination.

In this section the procedure for the data analysis will be described. The extraction of the raw asymmetries A^{raw} from the DAQ count rates will be described first, followed by beam charge (intensity) normalization and its effect on the measured asymmetry. Then, corrections due to fluctuations in the beam position, angle and energy (section III B) are applied to extract the beam-corrected raw asymmetries $A^{\text{bc,raw}}$. Results on the target boiling effect are presented next (section III C). Results on beam polarization are presented in section III D which constitute a major normalization to the asymmetry, leading to the preliminary physics asymmetry $A^{\text{phys}}_{\text{prel}}$. Calibrations of the beam position and HRS optics are crucial for evaluation of the event kinematics (section III E), and a full scale simulation of the HRS transport functions was carried out to confirm our understanding of the kinematics resulting from these calibrations (section III F). Next, corrections to the preliminary physics asymmetries due to various backgrounds will be presented in detail (section III G). Radiative corrections due to energy losses of the incident and the scattered electrons will be presented (section III H), followed by corrections due to the higher-order $\gamma\gamma$ box diagrams (section III I). After all corrections are applied, the preliminary physics asymmetries become the final physics asymmetry results presented in section IV A.

A. Forming Raw Asymmetries

The scattered electrons and pions were counted by the DAQ for each 33 ms helicity window. The response of each beam monitor, including the BCM and all BPMs, was digitized and integrated over the same helicity windows and recorded. For each window pair i , the pair-wise raw electron cross-section asymmetry A_i^{raw} in each HRS was computed from the the DAQ counts $c_i^{+(-)}$ normalized to the integrated beam intensity $I_i^{+(-)}$ in the positive (negative) helicity window:

$$A_i^{\text{raw}} = \left(\frac{\frac{c_i^+}{I_i^+} - \frac{c_i^-}{I_i^-}}{\frac{c_i^+}{I_i^+} + \frac{c_i^-}{I_i^-}} \right). \quad (38)$$

If the noise from beam fluctuations and the target boiling effect is negligible, the uncertainty is given by the purely statistical value:

$$\delta A_{i,\text{stat}}^{\text{raw}} = \sqrt{\frac{1}{c_i^+ + c_i^-}}. \quad (39)$$

If a total of n window pairs have been collected, the average raw asymmetry A^{raw} was formed by

$$A^{\text{raw}} = \langle A_i^{\text{raw}} \rangle \equiv \frac{\sum_{i=1}^n A_i^{\text{raw}} / (\delta A_{i,\text{stat}}^{\text{raw}})^2}{\sum_{i=1}^n 1 / (\delta A_{i,\text{stat}}^{\text{raw}})^2}, \quad (40)$$

and its statistical uncertainty is

$$\delta A_{\text{stat}}^{\text{raw}} = \sqrt{\frac{1}{N^+ + N^-}} \approx \frac{\delta A_{i,\text{stat}}^{\text{raw}}}{\sqrt{n}}, \quad (41)$$

where $N^\pm = \sum_{i=1}^n c_i^\pm$ refer to the total electron counts from the n window pairs and the approximation is valid if the beam current remains constant during the data taking.

When forming raw asymmetries, loose requirements were imposed on the beam quality: periods with low beam current or with the energy measured in BPM12x differing by more than 10σ from its nominal value were rejected, removing about 10% of the total data sample. No beam-helicity-dependent cuts were applied. The uncertainty in A^{raw} could be enlarged by helicity-dependent fluctuations in the beam intensity, position, angle, energy, and target boiling, causing a non-statistical contribution to the measurement. Therefore, an important criterion for a successful asymmetry measurement is to control non-statistical noise to a negligible level, which ensures that the main source of the uncertainty is the well-understood statistical fluctuation, and minimizes the run time.

B. Beam Intensity Normalization, Beam Corrections, and Their Systematic Fluctuations

For all PVES experiments at JLab, the polarized beam and the target were designed such that the fluctuations in the helicity difference in the signal between a pair of successive windows were dominated by scattered electron counting statistics. An example of possible non-statistical contributions is a window-to-window relative beam intensity asymmetry $A_I \equiv (I^+ - I^-)/(I^+ + I^-)$ with an uncertainty $\delta(A_I)$. During the PVDIS experiment, A_I for a 30 ms beam window at a 100 μA current was measured to be below 4×10^{-5} , with δA_I between 2×10^{-4} and 2×10^{-3} depending on the quality of the laser and the beam tune. At a 1-MHz counting rate the counting statistics for each 66-ms beam helicity pair is $\delta(A_i^{\text{raw}}) = 0.00387$ [Eq. (39)]. The actual value was larger because the rate was lower than 1 MHz (Table II). Therefore, the small $\delta(A_I)$ of the polarized beam at JLab guaranteed $\delta(A_I) \ll \delta A_{i,\text{stat}}^{\text{raw}}$ for this experiment. Thanks to the feedback control to the laser at the polarized source, the cumulative average for A_I throughout the experiment was below 0.1 ppm.

Beam properties other than the intensity do not enter the direct asymmetry evaluation, but they might affect the asymmetry measurement. To study how such beam properties affect the measured asymmetry, we first write Eq. (38) as

$$A_i^{\text{raw}} \approx \left(\frac{c^+ - c^-}{c^+ + c^-} \right)_i - \left(\frac{I^+ - I^-}{I^+ + I^-} \right)_i = A_{i,c}^{\text{raw}} - \left(\frac{1}{I^+ + I^-} \right)_i \Delta I_i, \quad (42)$$

where $A_{i,c}^{\text{raw}}$ is the raw count asymmetry and $\Delta I_i \equiv (I^+ - I^-)_i$. This approximation is valid for $A_I \ll 1$ which was true as stated in the previous paragraph. Similarly, the raw asymmetry might be affected by fluctuations in beam energy, position and angle. These beam-related corrections (bc) can be parametrized as:

$$(A^{\text{bc,raw}})_i = A_i^{\text{raw}} - \sum_j [\alpha_j (\Delta X_j)_i]. \quad (43)$$

Here, X_j denote beam parameters such as energy, position and angle, $\Delta X_j \equiv X_j^+ - X_j^-$ their corresponding helicity fluctuation, and α_j their coefficients that depend on the kinematics of the specific reaction being studied as well as the detailed spectrometer and detector geometry of the experiment.

The five BPMs equipped during this experiment: BPMA-X (horizontal), BPMA-Y (vertical), BPMB-X,Y, and BPM12x allowed measurements of the relative change in the beam energy, position and angle within one helicity window pair. One can then write

$$(A^{\text{bc,raw}})_i = A_i^{\text{raw}} - \sum_j [c_j(\Delta x_j)_i], \quad (44)$$

where x_j is the beam position measured by the five BPMs (BPMA-X,Y, BPMBX,Y, BPM12x) and $c_j \equiv \alpha_j \partial X_j / \partial x_j$. It is worth noting that this approach of making corrections window by window automatically accounts for occasional random instabilities in the accelerator.

If one corrects the pair-wise asymmetry for the beam fluctuations based on Eq. (44), the resulting asymmetry averaged over a certain number of helicity pairs can be written as

$$A^{\text{bc,raw}} \equiv \langle A_i^{\text{bc,raw}} \rangle = \langle A_i^{\text{raw}} \rangle - \sum_j c_j \langle \Delta x_j \rangle = A^{\text{raw}} - \sum_j \Delta A_{x_j} \quad (45)$$

where $\Delta A_{x_j} \equiv c_j \langle (x_j^+ - x_j^-) \rangle$ represents the correction needs to be applied to the raw asymmetry due to helicity-dependent fluctuation in x_j .

For this experiment, the values of c_j were obtained using two methods: The first one is called the “dithering” method [19], in which the beam position, angle, and energy were modulated periodically during data taking. The values of c_j were then calculated from the resulting variation in the measured asymmetry recorded for each of the five BPM variables. The energy of the beam was varied by applying a control voltage to a vernier input on a cavity in the accelerator’s South Linac. The beam positions and angles were modulated using seven air-core corrector coils in the Hall A beamline upstream of the dispersive arc [19]. Because these modulation periods represent quality data, they were included in the production data sample with the appropriate corrections made. In the second method the values of c_j were evaluated utilizing only natural fluctuations of the beam position, angle, and energy. This is called the “regression” method. The difference in the corrected asymmetry between the dithering and the regression method was used as the uncertainty in the beam-corrected raw asymmetries $A^{\text{bc,raw}}$.

To control the beam position differences at BPMA and BPMB, the feedback system controlled by the HAPPEX DAQ made adjustments of the circular polarization of the laser beam. The resulting beam position differences were in the range $(0.01 - 0.1)\mu\text{m}$ at the target for the majority of the data taking period. Based on the measured c_j values this resulted in ΔA_{x_j} in the range $(0.1 - 1)$ ppm. The cumulative averages for ΔA_{x_j} were found to be below 0.1 ppm integrated over the whole experiment. The measured asymmetry was found to be much less sensitive to beam energy fluctuations than to those of the beam position. Table III shows the corrections due to fluctuations in the five measured beam positions using the dithering method. The beam-corrected asymmetries based on both the dithering and regression methods, $A_{\text{dit}}^{\text{bc,raw}}$ and $A_{\text{reg}}^{\text{bc,raw}}$, are shown in Table IV. The narrow and the wide paths of the DAQ produced very similar results, with slight differences in their event collection due to DAQ deadtime and different timing alignment between electronic modules, resulting in a slightly better PID performance of the wide-paths [54]. In addition, dithering and regression methods are in principle equivalent. Still, the narrow-path asymmetry results with the beam corrections applied using the dithering method were used to produce the physics results of the present experiment because of the smaller deadtime.

Compared to the uncertainties from counting statistics, one can see that overall the corrections due to beam fluctuation were quite small, and their uncertainties are negligible. The asymmetry measurement was completely dominated by the counting statistics of the scattered electrons [54].

C. Target boiling effect on the measured asymmetry

As described in section IID, the electron beam deposited energy in the liquid deuterium target and caused additional noise to the measurement. This target boiling effect would manifest itself as an increase in the standard deviation of the measured pair-wise asymmetry A^{raw} above that expected from the counting statistics of Eq. (39,41). Rastering the beam to larger transverse sizes reduces the beam heating and thus the boiling effect.

Studies of the target boiling effect was performed. For each measurement a Gaussian was fitted to the distribution of the pair-wise asymmetries with δA given by the fitted width. Figure 7 shows the measured δA , taken at kinematics DIS #2 for various raster sizes at two beam currents 100 and 115 μA .

Results of δA in Fig. 7 were fitted with the functional form $p_0 x^{p_1} + p_2$ where x is the raster size in mm. The parameter p_2 represents the purely statistical fluctuation that depends only on the beam current, while the term $p_0 x^{p_1}$ is an empirical term that

Monitor	Left DIS#1 ΔA_{dit} (ppm)		Left DIS#2 ΔA_{dit} (ppm)		Right DIS# 2 ΔA_{dit} (ppm)	
DAQ path	narrow	wide	narrow	wide	narrow	wide
BPM4AX	0.173	0.179	0.513	0.569	-0.172	-0.182
BPM4AY	0.001	-0.010	0.286	0.262	-0.021	-0.027
BPM4BX	-0.152	-0.159	-0.368	-0.430	0.226	0.237
BPM4BY	-0.028	-0.020	-0.262	-0.243	-0.008	-0.003
BPM12x	0.000	0.000	0.024	0.022	-0.003	-0.003
Total	-0.006	-0.010	0.193	0.180	0.022	0.022

Monitor	RES I ΔA_{dit} (ppm)		RES II ΔA_{dit} (ppm)		RES III ΔA_{dit} (ppm)		RES IV ΔA_{dit} (ppm)		RES V ΔA_{dit} (ppm)	
DAQ path	narrow	wide	narrow	wide	narrow	wide	narrow	wide	narrow	wide
BPM4AX	-0.175	-0.178	0.313	0.320	-0.013	0.000	-1.004	-1.192	-3.708	-3.631
BPM4AY	0.230	0.224	0.096	0.107	0.047	0.046	0.328	0.328	0.400	0.317
BPM4BX	0.369	0.375	-0.568	-0.582	0.020	-0.005	1.398	1.596	4.754	4.603
BPM4BY	-0.139	-0.133	-0.132	-0.143	-0.038	-0.037	-0.235	-0.250	-0.265	-0.183
BPM12x	-0.010	-0.011	0.045	0.045	-0.005	-0.005	0.002	0.003	-0.035	-0.036
Total	0.275	0.277	-0.246	-0.253	0.011	-0.001	0.489	0.485	1.146	1.070

TABLE III: Corrections to DIS (top) and resonance (bottom) asymmetries evaluated using the dithering method, ΔA_{dit} . The “narrow” and “wide” refer to the DAQ trigger type [54]. The corrections were applied as $A_{\text{dit}}^{\text{bc,raw}} = A^{\text{raw}} - \Delta A_{\text{dit}}$ [Eq. (45)].

	Left DIS#1	Left DIS#2	Right DIS#2
A^{raw} , narrow (ppm)	-78.4 ± 2.7	-140.5 ± 10.4	-139.9 ± 6.6
$A_{\text{dit}}^{\text{bc,raw}}$, narrow (ppm)	-78.5 ± 2.7	-140.3 ± 10.4	-139.8 ± 6.6
$A_{\text{reg}}^{\text{bc,raw}}$, narrow (ppm)	-78.5 ± 2.7	-140.5 ± 10.4	-140.3 ± 6.6
$ A_{\text{dit}}^{\text{bc,raw}} - A_{\text{reg}}^{\text{bc,raw}} $, narrow (ppm)	0.1	0.2	0.5
A^{raw} , wide (ppm)	-78.2 ± 2.7	-140.3 ± 10.4	-140.9 ± 6.6
$A_{\text{dit}}^{\text{bc,raw}}$, wide (ppm)	-78.3 ± 2.7	-140.1 ± 10.4	-140.9 ± 6.6
$A_{\text{reg}}^{\text{bc,raw}}$, wide (ppm)	-78.3 ± 2.7	-140.3 ± 10.4	-141.4 ± 6.6
$ A_{\text{dit}}^{\text{bc,raw}} - A_{\text{reg}}^{\text{bc,raw}} $, wide (ppm)	0.1	0.1	0.5

	Left RES I	Left RES II	Right RES III	Left RES IV	Left RES V
A^{raw} , narrow (ppm)	-55.4 ± 6.8	-63.5 ± 5.9	-54.4 ± 4.5	-104.5 ± 15.3	-69.0 ± 21.3
$A_{\text{dit}}^{\text{bc,raw}}$, narrow (ppm)	-55.1 ± 6.8	-63.8 ± 5.9	-54.4 ± 4.5	-104.0 ± 15.3	-67.9 ± 21.3
$A_{\text{reg}}^{\text{bc,raw}}$, narrow (ppm)	-55.2 ± 6.8	-63.6 ± 5.9	-54.6 ± 4.5	-104.3 ± 15.3	-68.6 ± 21.2
$ A_{\text{dit}}^{\text{bc,raw}} - A_{\text{reg}}^{\text{bc,raw}} $, narrow (ppm)	0.1	0.2	0.2	0.3	0.7
A^{raw} , wide (ppm)	-54.9 ± 6.8	-63.6 ± 5.9	-54.0 ± 4.5	-105.0 ± 15.3	-69.0 ± 21.5
$A_{\text{dit}}^{\text{bc,raw}}$, wide (ppm)	-54.6 ± 6.8	-63.9 ± 5.9	-54.0 ± 4.5	-104.6 ± 15.3	-67.9 ± 21.5
$A_{\text{reg}}^{\text{bc,raw}}$, wide (ppm)	-54.6 ± 6.8	-63.7 ± 5.9	-54.2 ± 4.5	-104.9 ± 15.2	-68.7 ± 21.4
$ A_{\text{dit}}^{\text{bc,raw}} - A_{\text{reg}}^{\text{bc,raw}} $, wide (ppm)	0.1	0.2	0.2	0.3	0.8

TABLE IV: Measured raw asymmetries from the narrow and the wide triggers after applying corrections from beam energy and position changes using the dithering and the regression methods. The asymmetry errors shown are statistical only. The differences between the two corrected asymmetries, $|A_{\text{dit}}^{\text{bc,raw}} - A_{\text{reg}}^{\text{bc,raw}}|$, were used as the uncertainty from beam corrections. The dithering-corrected asymmetries were used in further analysis, although dithering and regression methods are in principle equivalent. The narrow and the wide paths of the DAQ produced very similar results, with slight differences in their event collection due to DAQ deadtime and different timing alignment between electronic modules. The narrow-path asymmetry results ($A_{\text{dit}}^{\text{bc,raw}}$, narrow) were used in further analysis to produce the physics results because of their smaller deadtime [54].

describes the size of target boiling. Using the approximate electron rate (Table II), the purely statistical uncertainty for 66-ms wide beam helicity pairs is 0.029 at 100 μA and 0.027 at 115 μA . The fit results for p_2 agree with the expectation very well. The fit results for p_0 and p_1 show that the broadening due to boiling at a $4 \times 4 \text{ mm}^2$ raster size, $p_0 x^{p_1}$ with $x = 4$, is at the level

of 569 ppm for 100 μA and 1407 ppm for 115 μA . This is quite small compared to the value from purely statistical fluctuations ($p_0 \sim 10^4$ ppm), and thus the boiling effect did not contribute significantly to the uncertainty of the asymmetry measurement.

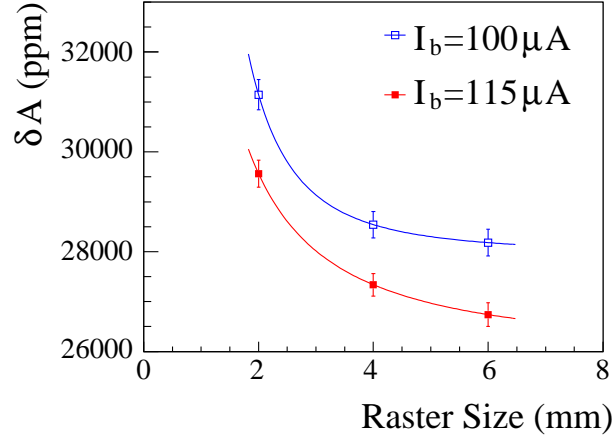


FIG. 7: (Color online) Measured standard deviation of the pair-wise asymmetries at kinematics DIS# 2, for various raster sizes and two beam currents 100 and 115 μA . The curves show the results of the fit $\delta A = p_0 x^{p_1} + p_2$ where x is the raster size in mm. The parameter p_2 represents the purely statistical fluctuation that depends only on the beam current and not the raster size, while the term $p_0 x^{p_1}$ is an empirical term that describes the size of target boiling. The fit results for 100 μA are $p_0 = (1.77 \pm 1.94) \times 10^4$, $p_1 = -2.48 \pm 1.85$, $p_2 = 27973.0 \pm 681.7$; and for 115 μA are $p_0 = (9.40 \pm 3.78) \times 10^3$, $p_1 = -1.37 \pm 1.09$, $p_2 = 25941.0 \pm 1433.4$. At a raster size of $4 \times 4 \text{ mm}^2$ ($x = 4$), the boiling noise is at the level of 569 ppm for 100 μA and 1407 ppm for 115 μA , and is negligible compared to the value from purely statistical fluctuations.

Figure 8 shows the measured δA for various beam currents I performed with a $4 \times 4 \text{ mm}^2$ square raster. If the measurement is dominated by statistical uncertainty, one expects $\delta A \propto \sqrt{I}$. Fit results of the measured δA indeed agree very well with this expectation, indicating that boiling effects at the running condition of this experiment was negligible.

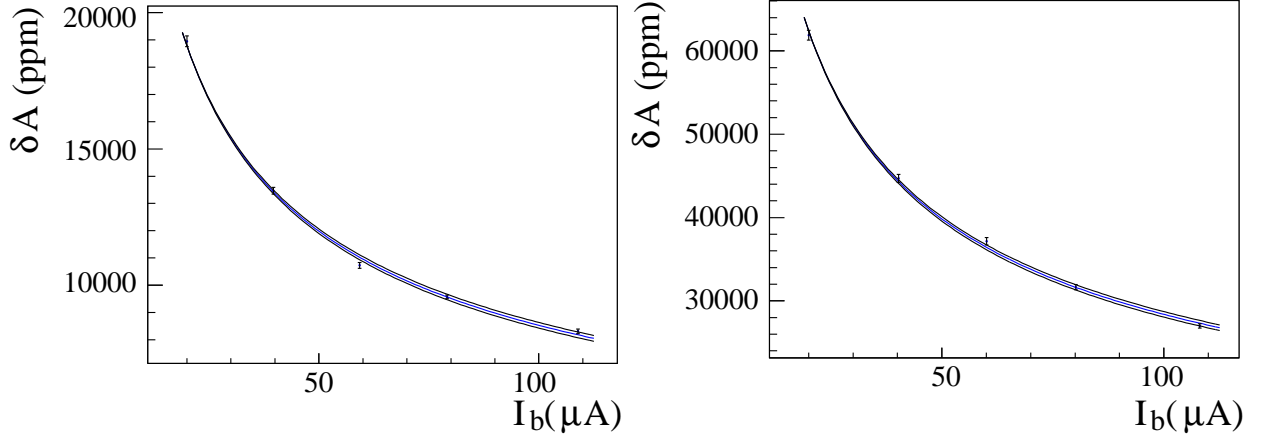


FIG. 8: [Color online] Measured standard deviation of the pair-wise asymmetries at various beam currents for DIS# 1 (left) and # 2 (right), with a $4 \times 4 \text{ mm}^2$ square raster. The curves show the results of the fit $\delta A \propto I^{p_3}$ and its error band. The fit results are $p_3 = 0.4900 \pm 0.0076$ and $p_3 = 0.4897 \pm 0.0072$ for DIS# 1 and # 2 respectively. These results are in good agreement with pure counting statistics ($\delta A \propto \sqrt{I}$).

D. Beam Polarization

As described in the previous section, the electron raw asymmetry was first corrected for the beam intensity and other beam-related properties such as position, angle and energy. The resulting asymmetry $A^{\text{bc,raw}}$ is then referred to as the measured asymmetry, A^{meas} , and must be corrected for the beam polarization P_e :

$$A_{\text{prel.}}^{\text{phys}} = A^{\text{meas}} / P_e, \quad (46)$$

to obtain the preliminary physics asymmetry $A_{\text{prel.}}^{\text{phys}}$. Both Compton and Møller polarimeters described in section II C were used.

During our experiment, the Møller polarimeter was available the entire time, while the Compton polarimeter initially suffered from a high background and only produced results in the last three weeks of the 2-month 6-GeV run period. The Compton polarimeter was also not available during the 4.8-GeV run period. Figure 9 shows the Møller polarimetry measurements taken with the 6 GeV beam. During the three weeks when both polarimeters were functioning, the average beam polarization from constant fits is 88.74% for Møller and 89.45% for Compton. The results from the two polarimeters are compared in Fig. 10. Note that the beam polarization can fluctuate over time due to motion of the laser position on the photocathode and photocathode aging.

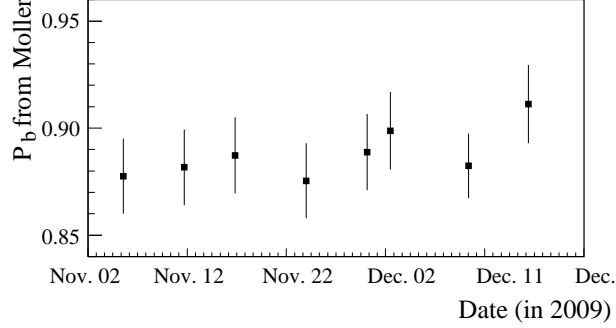


FIG. 9: Polarization results from the Møller polarimeter measurements taken with a beam energy of 6.067 GeV. The error bars represent the quadratic sum of the statistical and systematic errors. However, for each measurement the statistical uncertainty was in the order of 0.1%, much smaller than the systematic error. An additional measurement was done with a beam energy of 4.867 GeV at the end of the run period, which gave a similar polarization.

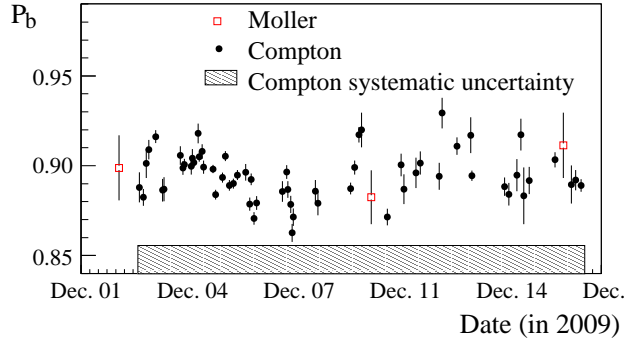


FIG. 10: (*Color online*) Comparison between Compton (black solid circles) and Møller (red open squares) measurements taken during the time period when both polarimeters were available. The beam energy was 6.067 GeV. The error bars for Møller represent the quadratic sum of the statistical and systematic errors, with the statistical error is smaller than the systematic by one order of magnitude. For Compton measurement, the statistical error are plotted with the data points and the systematic error (1.92% relative) are plotted along the horizontal axis. A constant fit to Compton measurements gave an average of 89.45% while the average of Møller results was 88.74%.

The experimental asymmetries were corrected for the beam polarization as follows:

1. When the Compton polarimeter was not available (before Dec. 2nd and after Dec. 17th, 2009), only Møller results were used. Each Møller result was used until the next measurement was available.
2. When there were both Compton and Møller measurements (from Dec. 2nd to Dec. 17th, 2009), the Compton data were averaged first for the time interval between two Møller measurements, then was averaged with the corresponding Møller measurement from the beginning of the interval. The averages were weighted by the statistical error. The systematic uncertainty of the combined polarization was obtained from that of each method as

$$(\Delta P_b/P_b)_{\text{syst,combined}} = 1/\sqrt{(\Delta P_b/P_b)_{\text{syst,compton}}^{-2} + (\Delta P_b/P_b)_{\text{syst,moller}}^{-2}}, \quad (47)$$

thus was smaller than the systematic uncertainty of either polarimetry. Each combined result was used until a next Møller measurement was available.

3. The beam polarization was corrected run by run for DIS#1 and #2. For resonance kinematics, the run period was short and a single correction was used for each kinematics.

The average beam polarization corrections are shown in Table V for all kinematics.

	Left DIS#2	Right DIS#2	RES IV and V
Combined P_e (syst.)	$(89.29 \pm 1.19)\%$	$(88.73 \pm 1.50)\%$	$(89.65 \pm 1.24)\%$

	Left DIS#1	RES I, II and III
Møller P_e (syst.)	$(88.18 \pm 1.76)\%$	$(90.40 \pm 1.54)\%$

TABLE V: Average beam polarization P_e for each kinematics. These are either the combined results of Compton and Møller measurements (top), or results from Møller alone (bottom), depending on which polarimeter was available during the corresponding run period. For DIS#1 and #2 the corrections were applied run-by-run and the statistically-averaged value of P_e is shown. The uncertainties shown here are dominated by the systematic uncertainty, which for the combined results were obtained using Eq. (47). For all resonance kinematics which had short running period, a single value was used for each setting.

E. Calibration of the HRS Optics

To accurately determine the kinematics (Q^2, x, W) of each event, one must determine the absolute beam position on the target, and reconstruct the vertex position, the scattering angle and the scattered electron's momentum. These are provided by beam position calibration and the HRS optics calibration, as described below.

1. Beam Position Calibration

As described in Sec. II B, the beam position information for each event was obtained from the raster current rather than from the delayed BPM information. Calibrations between the raster current and the beam position thus became necessary. The BPM calibration can be described as:

$$\text{bpm } x = \langle \text{bpm offset } x \rangle + \langle \text{raster current } x \rangle \times \frac{\sigma_{\text{bpm},x}}{\sigma_{\text{raster current}}}, \quad (48)$$

$$\text{bpm } y = \langle \text{bpm offset } y \rangle + \langle \text{raster current } y \rangle \times \frac{\sigma_{\text{bpm},y}}{\sigma_{\text{raster current}}}. \quad (49)$$

Figure 11 shows the beam spot distributions projected to the target using the calibrated BPMA and BPMB information.

2. Optics Calibration Procedure and the Resulting Uncertainties in Q^2 Determination

The trajectory and momentum of each electron detected was determined by calibration of the transport functions (optics) of each HRS. During optics calibration runs, the VDCs were turned on to provide precise information on the particle trajectory, from which the hit position and angles at the focal plane (x, θ, y, ϕ) can be determined [53, 69]. The next step is to reconstruct the interaction position, angle, and momentum at the target from these focal plane variables, i.e., to determine the inverse of the HRS optical transport matrix. In practice, instead of a matrix operation, a set of tensors up to the 5th order were used to calculate the target variables from the focal plane values.

The target coordinates of the scattering event, $(x_{tg}, y_{tg}, \theta_{tg}, \phi_{tg})$, are defined in the target coordinate system (TCS) [69] with respect to the spectrometer central ray direction, see Fig. 12. Here the angles θ_{tg} and ϕ_{tg} refer to the tangent of the vertical and horizontal angles relative to the HRS central ray. The spectrometer pointing D is the distance at which the spectrometer misses the Hall center in the direction perpendicular to the spectrometer central ray. The sieve plane corresponds to the entrance of the spectrometer which is located at $L = 1.12$ m from the TCS origin. The particle hit position and the angles at the sieve plane can be directly calculated from the focal plane variables.

The calibration procedure involves three separate steps:

1. The vertex position along the beam, z_{react} , is related to y_{tg}, ϕ_{tg} in the TCS as well as the pointing D of the spectrometer. The vertex calibration was done by taking data on the multi-foil carbon target with known foil positions. The foil positions

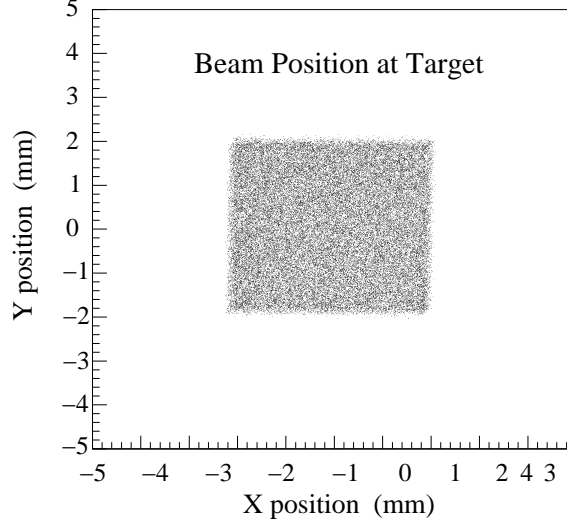


FIG. 11: Calibrated beam spot distribution at the target.

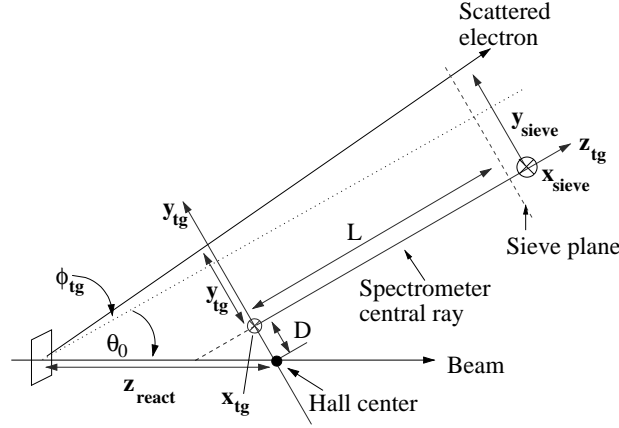


FIG. 12: Topview of the target coordinate system (TCS) (x_{tg}, y_{tg}, z_{tg}) and the sieve plane coordinate system (x_{sieve}, y_{sieve}) . The z_{tg} axis is along the HRS central ray, the y_{tg} axis is pointing to the left, the x_{tg} axis is pointing vertically down, and the origin of the TCS is the point along the HRS central ray that is the closest to the Hall center. The ϕ_{tg} is the tangent of the in-plane angle and θ_{tg} is the tangent of the out-of-plane angle (not shown) w.r.t. the spectrometer central ray. The sieve plane is located at a drift distance $L = 1.12$ m from the TCS origin, with the y_{sieve} axis pointing to the left of the spectrometer entrance and the x_{sieve} axis pointing vertically down. The pointing of the HRS, D , describes how much the HRS central ray misses the Hall center, and θ_0 is the angle of the HRS central ray w.r.t. the beamline. Figure reproduced from Refs. [53, 69]

were determined from data using the HRS optics matrix, the focal plane variables, and D . The precision on z_{react} in the direction perpendicular to the spectrometer central ray is given by

$$\Delta(z_{react} \sin \theta_0) = \sqrt{(\Delta z_{foil} \sin \theta_0)^2 + (\Delta z_{foil \text{ data}} \sin \theta_0)^2 + (\Delta D)^2}. \quad (50)$$

Here $\Delta z_{foil} = \pm 2.5$ mm is the uncertainty of the actual foil position caused by possible shifts of the target ladder during the target cool-down. The quantity $\Delta z_{foil \text{ data}}$ is the discrepancy in oil positions obtained from calibration data and the expected values. If the discrepancy is found to be consistent with zero, the value ± 0.1 mm is used. The uncertainty ΔD can be obtained from a spectrometer pointing survey with a typical precision of ± 0.5 mm. If a survey was not available, the value of D can be derived from surveys performed at a previous spectrometer angle setting. In this case, one compares the multi-carbon-foil data before and after the spectrometer rotation: if the observed shifts in z in all foil positions can be explained consistently by a global change in D , then the shift is added to the value of D from the previous survey

and the uncertainty of D is taken as ± 0.5 mm. If neither carbon foil data nor a survey was available, ΔD is taken to be ± 5 mm which is the limit of how much the spectrometer can physically miss the Hall center. At last, the uncertainty in the scattering angle due to the vertex calibration is

$$\Delta\phi_{tg} = \Delta(z_{\text{react}} \sin \theta_0)/L. \quad (51)$$

2. The scattering angles, θ_{tg}, ϕ_{tg} , were calibrated by inserting a so-called “sieve slit” plate – a 0.5-mm thick tungsten plate with an array of pinholes – at the entrance of the spectrometer. Reconstruction of hole positions depends on the angle elements of the optical matrix. The angle uncertainties from sieve slit calibrations are:

$$\Delta\theta_{tg} = \sqrt{(\Delta x_{\text{hole}})^2 + (\Delta x_{\text{hole data}})^2}/L, \quad (52)$$

$$\Delta\phi_{tg} = \sqrt{(\Delta y_{\text{hole}})^2 + (\Delta y_{\text{hole data}})^2}/L, \quad (53)$$

where the in-plane angle ϕ_{tg} affects the scattering angle θ directly, while the out-of-plane angle θ_{tg} affects θ only in the second order and the effect is small. The quantities $\Delta x_{\text{hole}}, \Delta y_{\text{hole}}$ are uncertainties in the actual hole position in the sieve plane. The most straightforward way to determine $x_{\text{hole}}, y_{\text{hole}}$ is by a survey of the sieve slit plate. The survey uncertainty is ± 0.5 mm for both directions. However survey was not always done for each kinematic setting. Past experience has shown that the horizontal position y_{hole} is highly reproducible, to ± 0.1 mm, and the vertical position x_{hole} is reproducible to ± 0.5 mm due to the fact that this is the direction in which the sieve plate is moved into or out of the HRS entrance. Thus if no survey was available, results from earlier surveys were used with these additional uncertainties added. The quantities $\Delta x_{\text{hole data}}, \Delta y_{\text{hole data}}$ are the discrepancy between the hole position obtained from calibration data and the expected values. In the case where no sieve slit calibration data was taken, the angle calibration of a preceding experiment can be used based on the high reliability of the HRS. In this case, an additional ± 0.5 mrad of uncertainty should be added to both $\Delta\theta_{tg}, \Delta\phi_{tg}$ to account for possible changes in the optics.

3. The most precise way to calibrate the momentum is to use elastic scattering from a carbon target or the proton inside a water target. With a water target, the relative momentum $\delta \equiv dp/p$ with p the HRS central momentum setting can be determined to $\pm 1 \times 10^{-4}$. Due to the high beam energy used, elastic measurement was not possible for the present experiment. However, water target calibration was performed during the preceding experiment (HAPPEX-III) [23]. The HAPPEX-III water calibration results were used for the present experiment with an uncertainty $\delta = \pm 5 \times 10^{-4}$ thanks to the established high stability of the HRS magnets and transport system.

The three calibration steps described above are assumed to be independent from each other, i.e., matrix elements related to position reconstruction have little dependence on those related to angle reconstruction, etc. For all calibrations, the optics tensor coefficients were determined from a χ^2 minimization procedure in which the events were reconstructed as close as possible to the known position of the corresponding foil target or the sieve-slit hole.

3. Optics Calibration Results

During the PVDIS experiment, there were seven kinematics settings in total with one of them carried out on both Left and Right HRS, thus there were a total of eight HRS+kinematics combinations: Left HRS DIS #1, Left and Right HRS DIS #2, Left HRS Resonance (RES) I, Left HRS RES II, Right HRS RES III, Left HRS RES IV, and Left HRS RES V. Either vertex or angle calibrations, or both, were carried out for all eight settings except RES IV and V. The vertex calibration for Left DIS#1 and the angle calibration results for Left RES II are shown in Fig. 13.

4. Q^2 Uncertainties

The Q^2 of each event was calculated using Eq. (3). The uncertainty in Q^2 is determined by the uncertainties in θ, E and E' , but is dominated by the scattering angle uncertainty. The scattering angle is calculated as [53]:

$$\theta = \cos^{-1} \left(\frac{\cos \theta_0 - \phi_{tg} \sin \theta_0}{\sqrt{1 + \theta_{tg}^2 + \phi_{tg}^2}} \right), \quad (54)$$

thus calibration of the horizontal angle ϕ_{tg} dominates the angle uncertainty. The total uncertainty on the scattering angle is the combination of the vertex calibration Eqs. (50-51) and $\Delta\phi_{tg}$ from the angle calibration:

$$\Delta\theta \approx \sqrt{(\Delta D/L)^2 + (\Delta z_{\text{foil}} \sin \theta_0/L)^2 + (\Delta z_{\text{foil data}} \sin \theta_0/L)^2 + (\Delta\phi_{tg})^2}. \quad (55)$$

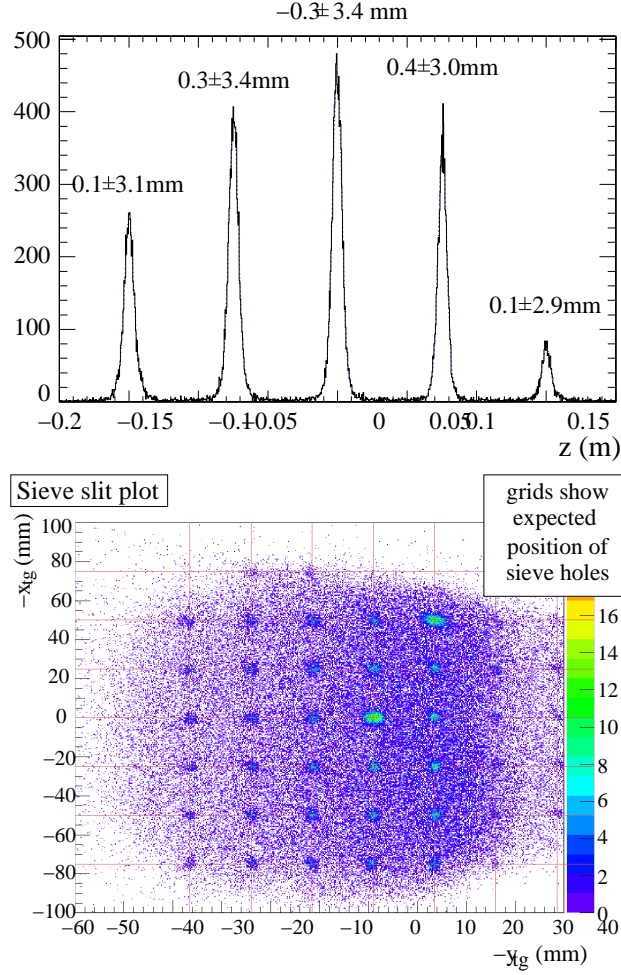


FIG. 13: (Color online) Top: vertex reconstruction for Left DIS#1. The number above each foil is $\Delta z_{\text{foil data}}$, defined as how much the observed foil position misses the expected value. The blue dotted lines are fits to the peak position. For all foils we have $\Delta z_{\text{foil data}} \leq 0.4$ mm. Bottom: reconstruction of the sieve hole positions for Left RES II. The data are shown as scattered points and are compared to the expected positions (grids). No obvious discrepancy is seen. The axes are oriented such that the sieve hole pattern is as if viewed when facing the spectrometer entrance. Two of the sieve holes are larger than others to allow identifying the center and the orientation of the sieve plate.

where $\Delta\phi_{tg}$ is either from Eq. (53) if a sieve slit calibration was available, or from previous calibrations with a 0.5 mrad additional uncertainty added. Here the drift distance is $L = 1.12$ m as shown in Fig. 12.

For some settings during PVDIS, there were both angle and vertex calibrations (Left RES I and II), or only the vertex but not the angle calibration (Left DIS#1, Left DIS#2, Right DIS#2, Right RES III), or neither (Left RES IV and V). For both vertex and angle calibrations, the optics database and some survey results from the HAPPEX-III experiment that ran immediately before this experiment were used. For RES#I which was taken on the left HRS only, the Q_1 and the dipole magnets were set at 4.00 GeV/c, but its Q_2 and Q_3 were limited to 3.66 GeV/c due to a power supply malfunction. This added complexity to the optical calibration for RES#I but did not affect the HRS acceptance and the quality of the optical calibration results. Taking all uncertainties into account, the uncertainty in Q^2 due to HRS optics calibration is summarized in Table VI.

F. HRS Simulations

For the present experiment, a simulation package called “HAMC” (Hall A Monte Carlo) was used to simulate the transport function and the acceptance of HRS. The simulation was then used to calculate the effect of electromagnetic radiative corrections and particle identification efficiency. To ensure that HAMC works correctly, we simulated the kinematics (Q^2, W, x) of the scattering, and it is expected that the simulated values should agree with the measured ones within the uncertainty of the optics calibration, Table VI.

HRS	Left HRS						Right HRS	
Kinematics	DIS#1	RES V	RES IV	DIS#2	Res I	Res II	DIS#2	Res III
$\theta_0(^{\circ})$	12.9	14.0	15.0	20	12.9	12.9	20	12.9
E_b (GeV)	6.067	6.067	6.067	6.067	4.867	4.867	4.867	4.867
E'_0 (GeV)	3.66	3.66	3.66	2.63	4.0 ^a	3.66	2.63	3.1
HRS pointing survey?	Y	N	N	Y	N	N	Y	N
δD (survey)(mm)	0.5			0.5			0.5	
Carbon multi foil data available?	Y	N	N	Y	Y	Y	Y	Y
δD (from data, no survey) (mm)					0.5	0.5	0.5	0.5
δD (no survey, no data)(mm)		5.0	5.0					
$\delta z_{\text{foil data}}$ (mm)	0.4	N/A	N/A	0.4	2.0	0.3	0.7	1.1
δz_{foil}	2.5	N/A	N/A	2.5	2.5	2.5	2.5	2.5
$\Delta\theta$ from vertex calibration (mrad), Eq. (51)	0.676	4.464	4.464	0.893	0.779	0.672	0.901	0.704
sieve survey	N	N	N	N	N	N	N	N
sieve data	N	N	N	N	Y	Y	N	N
Δx_{hole} , from prior survey (mm)	0.51	0.51	0.51	0.51	0.51	0.51	0.51	0.51
$\Delta x_{\text{hole data}}$ (mm)	0.1	N/A	N/A	0.1	0.1	0.1	0.1	0.1
additional $\Delta\phi_{tg}$ (mrad)	0.5 ^b	0.5 ^b	0.5 ^b	0.5 ^b	none	none	0.5 ^c	0.5 ^c
$\Delta\theta$ from angle calibration (mrad), Eq. (53)	0.682	0.676	0.676	0.682	0.464	0.464	0.676	0.676
Total $\Delta\theta$ (mrad)	0.960	4.515	4.515	1.124	0.907	0.816	1.134	0.976
Total $\Delta\theta/\theta$ (%)	0.426	1.848	1.725	0.322	0.403	0.363	0.325	0.434
$\Delta E'_0/E'_0$	5×10^{-4}							
Total $\Delta Q^2/Q^2$ (%) ^d	0.853	3.696	3.449	0.644	0.805	0.725	0.650	0.867

^a For RES#I which was taken on the left HRS only, the Q_1 and the dipole magnets were set at 4.00 GeV/c, but its Q_2 and Q_3 were limited to 3.66 GeV/c due to a power supply malfunction;

^b Due to using sieve calibration taken at Left RES#I;

^c Due to using optics database from HAPPEX-III;

^d Including uncertainties due to both scattering angle $\Delta\theta$ and momentum $\Delta E'$, but is dominated by the former.

TABLE VI: Uncertainty in Q^2 determination derived from optics calibration. For each HRS, the kinematics are shown from left to right in the chronological order.

In HAMC, events were generated with a uniform distribution along the beam direction and within a given raster size and the solid angle $d\Omega = \sin(\theta) d\theta d\phi$, then transported through the HRS magnets using a set of polynomials that model the electrons' trajectories through the magnetic fields. For RES #I, a separate set of polynomials were developed for the mismatching fields of Q_2 and Q_3 . Events that passed all magnet entrance and exit apertures fall within the HRS acceptance and are recorded. An average energy loss of 3 MeV was used for the incident electron beam to account for the effect of traversing all material along the beamline to the target center. Multiple scattering in the target material, energy loss due to external and internal Brehmstrahlung and ionization loss, and the 200 μm resolution of the VDC wires were also taken into account in HAMC. The physical differential cross section $d^2\sigma/(dE' d\Omega)$ and the parity-violating asymmetry were calculated using the MSTW PDF parametrization for each simulated event.

Because the DAQ used in the present experiment relied on hardware-based PID, PID calibration runs were carried out daily to monitor the detector and the DAQ performance. It was found that the electron efficiency varied with the particle's hit position in the vertical (dispersive) direction on the lead-glass detector. This variation could cause a shift in the Q^2 value of the measurement and must be incorporated into HAMC. In HAMC, the hit position on the lead-glass detector was calculated from the focal plane coordinates, such that the PID efficiency measured from data can be applied to each simulated event. The efficiency could drift due to electronic module malfunction and drifts in the discriminator thresholds. For most of kinematics, such a drift was gradual and daily calibrations were sufficient to correct for its effect.

In general, the acceptance of the HRS is defined by combining the opening geometry of the intermediate apertures, whose nominal settings were documented in Ref. [53]. The real acceptance however can be different from the nominal settings. The HRS acceptance of the simulation was fine-tuned by matching these apertures to the cross-section-weighted event distributions obtained from data. This process is illustrated in Fig. 14.

Once all magnet apertures were optimized, the kinematics (Q^2, x) were calculated from HAMC using Eqs. (3,4), the beam energy E (minus 3 MeV as mentioned earlier), and the E' and the scattering angles of the simulated events. Similarly, we calculated the (Q^2, x) values from data using the vertex coordinates ($x_{tg}, y_{tg}, \theta_{tg}, \phi_{tg}$) reconstructed from the detected focal

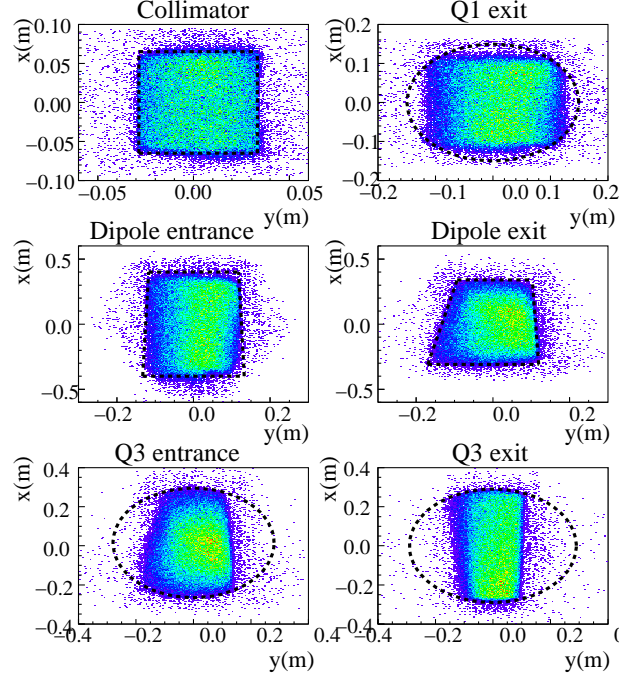


FIG. 14: (*Color online*) Fine-tuning of the HRS acceptance in HAMC. Event distributions from data are plotted at the collimator (entrance of the HRS Q_1), Q_1 exit, entrances and exits of the dipole and Q_3 . From these distribution, the best estimate of the position and the size of the apertures were determined (black dashed lines and curves). These were then used as aperture or acceptance cuts in HAMC. The axes are oriented such that the distributions are as viewed along the particle trajectory, with y the horizontal and x the vertical (dispersive) directions, respectively.

plane variables, based on HRS transport functions. The agreement between the HAMC (Q^2, x) and those reconstructed from the data thus provides a measure of how well the simulation works.

Figure 15 shows comparisons between data and simulation for all four target variables, Q^2 and x , for Left HRS DIS #1 and Right HRS DIS #2. A summary of the comparison for all kinematics is given in Table VII. The observed differences in Q^2 are consistent with the uncertainties shown in Table VI for most of the kinematics. For RES III, there is a two-standard-deviation disagreement in Q^2 , but is still negligible compared to the statistical uncertainty at this kinematics. In addition, since we interpret the asymmetry results at the measured Q^2 , not the simulated value, this disagreement does not affect the final result or its uncertainty evaluation and interpretation.

Kinematics	HAMC			data			relative difference in Q^2
	$\langle Q^2 \rangle$	$\langle x \rangle$	$\langle W^2 \rangle$	$\langle Q^2 \rangle$	$\langle x \rangle$	$\langle W^2 \rangle$	
	(GeV/c) ²		GeV ²	(GeV/c) ²		GeV ²	
Left HRS DIS#1	1.084	0.241	4.294	1.085	0.241	4.297	< 0.1%
Left+Right HRS DIS#2	1.892	0.294	5.424	1.901	0.295	5.430	0.5%
Left HRS RES I	0.956	0.571	1.600	0.950	0.571	1.595	0.6%
Left HRS RES II	0.832	0.336	2.528	0.831	0.335	2.530	0.1%
Right HRS RES III	0.745	0.225	3.443	0.757	0.228	3.450	1.6%
Left HRS RES IV	1.456	0.324	3.925	1.472	0.326	3.923	1.1%
Left HRS RES V	1.268	0.282	4.109	1.278	0.283	4.122	0.8%

TABLE VII: Comparison of Q^2 , x , and W^2 between HAMC and data for all kinematics. The Left and the Right DIS#2 have been combined. The difference in Q^2 between HAMC and data is smaller than Table VI for most of the kinematic settings.

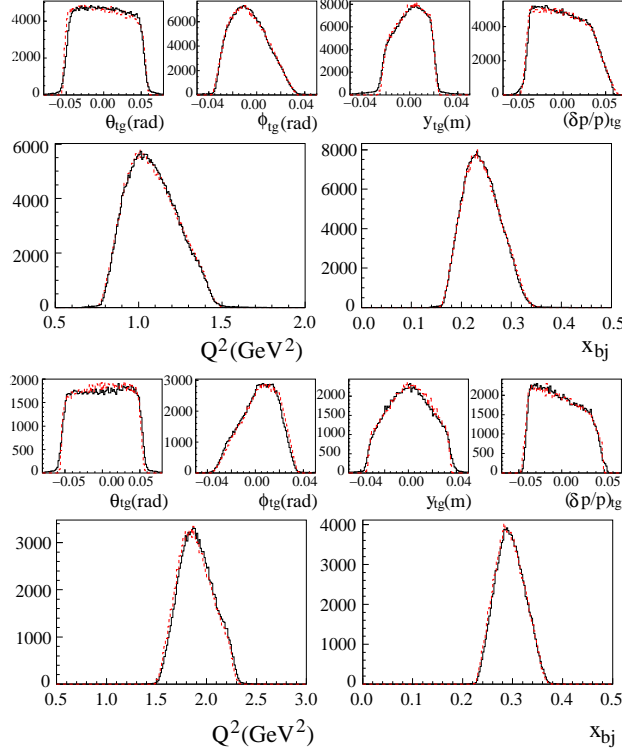


FIG. 15: (Color online) Comparison between HAMC (red, dashed) and data (black, solid). From top to bottom: target variables – θ_{tg} , ϕ_{tg} , y_{tg} and $(\delta p/p)_{tg}$ – for Left HRS DIS#1; Q^2 and x for Left HRS DIS#1; target variables for Right HRS DIS#2; Q^2 and x for Right HRS DIS#2.

G. Background Analysis

In this section we analyze all backgrounds that affect the extracted PV electron asymmetry. Assuming each background has an asymmetry A_i and affects the electron sample with a fraction f_i , the correction can be applied as

$$A^{\text{phys}} = \frac{\left(\frac{A^{\text{bc,raw}}}{P_b} - \sum_i A_i f_i \right)}{1 - \sum_i f_i}, \quad (56)$$

where $A^{\text{bc,raw}}$ is the measured asymmetry with helicity-dependent beam corrections applied, and P_b is the beam longitudinal polarization presented in section III D. When all f_i are small with A_i comparable to or no larger than $A^{\text{bc,raw}}$, one can define

$$\bar{f}_i = f_i \left(1 - \frac{A_i}{A^{\text{bc,raw}}} P_b \right) \quad (57)$$

and approximate

$$A^{\text{phys}} \approx \frac{A^{\text{bc,raw}}}{P_b} \Pi_i (1 + \bar{f}_i), \quad (58)$$

i.e., all background corrections can be treated as multiplicative. As can be seen from Eq. (58), the order of the corrections is flexible and the corrections can be applied to the measured asymmetry $A^{\text{bc,raw}}$ before normalizing to the beam polarization. The uncertainty of the correction \bar{f}_i causes directly a relative uncertainty on the electron asymmetry

$$\frac{\Delta A_e}{A_e} = \Delta \bar{f}_i. \quad (59)$$

Some effects, such as charged pion and pair-production background, are very small such that corrections [Eq. (58)] are not necessary. For those cases only the uncertainty $\Delta \bar{f}_i$ or $\Delta A_e/A_e$ is presented. The prescription of Eq. (58) was also used for the treatment of the Q^2 -uncertainty and radiative corrections (sections III F, III H and III I).

1. Charged Pion Background

Charged pions are produced in the decays of nucleon resonances created by electro- or photo-production. Since photo-production typically dominates (which has a much smaller parity-violating asymmetry than electroproduction), they have a smaller parity-violating asymmetry than DIS electrons. This has been confirmed by the asymmetry of the pion triggers measured during the experiment. The charged pion background thus reduces the magnitude of the measured asymmetry, and the effect is the largest if the charged pions did not carry asymmetry at all. Furthermore, the high particle identification performance of the DAQ limited the pion contamination in the electron trigger to the level of $f_{\pi/e} < 2 \times 10^{-4}$ and $< 4 \times 10^{-4}$ for the three DIS kinematics and the five resonance kinematics, respectively [54]. Due to the small contamination, no correction to the measured electron asymmetries was made. The total systematic uncertainty on the measured electron asymmetry due to pion contamination and pion asymmetry is:

$$\left(\frac{\Delta A_e}{A_e}\right)_{\pi^-} = \sqrt{(\Delta f_{\pi/e})^2 + \left(f_{\pi/e} \frac{|A_\pi| + \Delta A_\pi}{A_e}\right)^2}, \quad (60)$$

where $f_{\pi/e}$ and $\Delta f_{\pi/e}$ are the event fraction of the electron trigger that is from actual pions and its uncertainty, A_π is the measured pion asymmetry with ΔA_π its uncertainty, and A_e is the measured electron asymmetry. The term $|A_\pi| + \Delta A_\pi$ corresponds to how much the pion asymmetry could differ from zero at the 68.3% confidence level. As inputs to the background correction, the extraction of pion asymmetries is described below.

pion asymmetry measurement

The PID performance of both electron and pion triggers of the DAQ was reported in Ref. [54]. To properly extract pion asymmetries from the trigger, one must account for the effect of electron contamination in the pion triggers, $f_{e/\pi}$. Because $f_{e/\pi}$ was relatively high and the electron asymmetries are larger than those of pions, corrections were applied to the asymmetries extracted from the pion triggers using

$$A_\pi^{\text{meas}} = \frac{A_{\pi,\text{dit}}^{\text{bc,raw}} - f_{e/\pi} A_{e,\text{dit}}^{\text{bc,raw}}}{1 - f_{e/\pi}}, \quad (61)$$

where $A_{\pi,\text{dit}}^{\text{bc,raw}}$ and $A_{e,\text{dit}}^{\text{bc,raw}}$ are asymmetries extracted from pion and electron triggers, respectively, with beam corrections applied using the dithering method. Then the measured pion asymmetries were normalized with the beam polarization, giving physics asymmetry results for pion inclusive production:

$$A_\pi^{\text{phys}} = \frac{A_\pi^{\text{meas}}}{P_b}. \quad (62)$$

Results for pion asymmetries in the DIS and resonance kinematics are given in Tables VIII and IX. As described in Ref. [54], the narrow-path triggers of the DAQ had smaller counting deadtime than the wide-path triggers, but slightly lower PID performance. As a result the narrow pion triggers had more electron contamination than the wide triggers and requires a larger correction, which causes a larger uncertainty in the extracted pion asymmetry.

electron asymmetry uncertainty due to pion contamination The measured pion and electron asymmetries are listed in Tables X and XI for the two DIS and the five resonance kinematics, respectively, together with the total uncertainty due to pion contamination in the electron asymmetry as calculated with Eq. (60). The values listed for the pion contamination in the electron triggers $f_{\pi/e}$ and the electron contamination in pion triggers $f_{e/\pi}$ and their total uncertainties are from Ref. [54]. The narrow-path triggers have larger uncertainty due to charged pion background because of the slightly lower pion rejection performance. Overall, the uncertainty due to charged pion background is very low, at the 10^{-4} level for all kinematics.

2. Pair Production Background

The pair production background results from nucleon resonance production when the resonance decays into neutral pions (π^0) that then decay into e^+e^- pairs. Pair production from bremsstrahlung photons is not significant in the kinematics of this experiment because pair production is highly forward-peaked. Therefore, one expects that the effect from pair-production background to have a similar effect as that from charged pions and the prescription of Eq. (60) can be used by replacing A_π with A_{e^+} and $f_{\pi/e}$ with the fractional contribution of pair production to the main electron trigger f_{e^+/e^-} . For the pair-production asymmetry, we expect it to be determined by the π^0 photo- and electroproduction and thus comparable to that of the charged pion asymmetry. The contamination factor f_{e^+/e^-} was determined for the two DIS kinematics by reversing the HRS polarity

HRS, Kinematics	Left DIS#1	Left DIS#2	Right DIS#2
narrow path			
$A_{\pi,\text{dit}}^{\text{bc,raw}} \pm \Delta A_{\pi,\text{dit}}^{\text{bc,raw}} (\text{stat.}) (\text{ppm})$	-57.3 ± 8.0	-26.0 ± 14.9	-21.5 ± 4.2
$f_{e/\pi} \pm \Delta f_{e/\pi} (\text{total})$	0.2653 ± 0.0603	0.0331 ± 0.0034	0.0103 ± 0.0013
$A_{\pi}^{\text{meas}} \pm \Delta A_{\pi}^{\text{meas}} (\text{total}) (\text{ppm})$	-48.8 ± 14.0	-22.0 ± 21.4	-20.3 ± 6.0
$A_{\pi}^{\text{phys}} \pm \Delta A_{\pi}^{\text{phys}} (\text{total}) (\text{ppm})$	-55.3 ± 15.9	-24.6 ± 24.0	-22.9 ± 6.8
wide path			
$A_{\pi,\text{dit}}^{\text{bc,raw}} \pm \Delta A_{\pi,\text{dit}}^{\text{bc,raw}} (\text{stat.}) (\text{ppm})$	-49.6 ± 7.7	-27.0 ± 14.9	-21.4 ± 4.2
$f_{e/\pi} \pm \Delta f_{e/\pi} (\text{total})$	0.2176 ± 0.0573	0.0281 ± 0.0037	0.0091 ± 0.0013
$A_{\pi}^{\text{meas}} \pm \Delta A_{\pi}^{\text{meas}} (\text{total}) (\text{ppm})$	-41.3 ± 12.8	-23.7 ± 21.4	-20.3 ± 6.0
$A_{\pi}^{\text{phys}} \pm \Delta A_{\pi}^{\text{phys}} (\text{total}) (\text{ppm})$	-46.8 ± 14.6	-26.5 ± 24.0	-22.9 ± 6.8

TABLE VIII: For DIS kinematics: beam-corrected pion asymmetries $A_{\pi,\text{dit}}^{\text{bc,raw}}$ with their statistical uncertainties, electron contamination in the pion triggers $f_{e/\pi}$, pion asymmetry results after being corrected for electron contamination A_{π}^{meas} , and physics asymmetry results for pion inclusive production A_{π}^{phys} . As described in Ref. [54], the narrow-path triggers had higher electron contamination, thus required a larger correction and had a larger uncertainty in the extracted pion asymmetry.

HRS	Left RES I	Left RES II	Right RES III	Left RES IV	Left RES V
narrow path					
$A_{\pi,\text{dit}}^{\text{bc,raw}} \pm \Delta A_{\pi,\text{dit}}^{\text{bc,raw}} (\text{stat.}) (\text{ppm})$	-44.2 ± 40.1	-69.8 ± 26.5	-17.1 ± 8.5	21.8 ± 47.7	-46.7 ± 64.0
$f_{e/\pi} \pm \Delta f_{e/\pi} (\text{total})$	0.4114 ± 0.0201	0.3155 ± 0.0163	0.0849 ± 0.0030	0.1852 ± 0.0073	0.1871 ± 0.0077
$A_{\pi}^{\text{meas}} \pm \Delta A_{\pi}^{\text{meas}} (\text{total}) (\text{ppm})$	-33.7 ± 88.6	-73.2 ± 48.8	-13.5 ± 12.7	52.2 ± 76.2	-41.5 ± 102.4
$A_{\pi}^{\text{phys}} \pm \Delta A_{\pi}^{\text{phys}} (\text{total}) (\text{ppm})$	-37.3 ± 98.0	-81.0 ± 54.0	-14.9 ± 14.0	58.2 ± 85.0	-46.3 ± 114.2
wide path					
$A_{\pi,\text{dit}}^{\text{bc,raw}} \pm \Delta A_{\pi,\text{dit}}^{\text{bc,raw}} (\text{stat.}) (\text{ppm})$	-45.4 ± 39.4	-69.2 ± 26.1	-18.3 ± 8.5	30.9 ± 47.6	-51.0 ± 64.9
$f_{e/\pi} \pm \Delta f_{e/\pi} (\text{total})$	0.3423 ± 0.0231	0.2409 ± 0.0200	0.0633 ± 0.0060	0.1661 ± 0.0080	0.1598 ± 0.0086
$A_{\pi}^{\text{meas}} \pm \Delta A_{\pi}^{\text{meas}} (\text{total}) (\text{ppm})$	-39.8 ± 74.9	-71.0 ± 43.7	-15.8 ± 12.4	58.8 ± 74.7	-47.7 ± 101.4
$A_{\pi}^{\text{phys}} \pm \Delta A_{\pi}^{\text{phys}} (\text{total}) (\text{ppm})$	-44.0 ± 82.9	-78.5 ± 48.4	-17.5 ± 13.7	65.6 ± 83.3	-53.2 ± 113.1

TABLE IX: For resonance kinematics: beam-corrected pion asymmetries $A_{\pi,\text{dit}}^{\text{bc,raw}}$ with their statistical uncertainty, electron contamination in the pion triggers $f_{e/\pi}$, pion asymmetry results after being corrected for electron contamination A_{π}^{meas} , and physics asymmetry results for pion inclusive production A_{π}^{phys} . As described in Ref. [54], the narrow-path triggers had higher electron contamination, thus required a larger correction and had a larger uncertainty in the extracted pion asymmetry.

HRS, Kinematics	Left DIS#1	Left DIS#2	Right DIS#2
narrow path			
$A_{\pi}^{\text{meas}} \pm \Delta A_{\pi}^{\text{meas}} (\text{total}) (\text{ppm})$	-48.8 ± 14.0	-22.0 ± 21.4	-20.3 ± 6.0
$A_{e,\text{dit}}^{\text{bc,raw}} \pm A_{e,\text{dit}}^{\text{bc,raw}} (\text{stat.}) (\text{ppm})$	-78.5 ± 2.7	-140.3 ± 10.4	-139.8 ± 6.6
$f_{\pi/e} \pm \Delta f_{\pi/e} (\text{total}) (\times 10^{-4})$	(1.07 ± 0.24)	(1.97 ± 0.18)	(1.30 ± 0.10)
$\left(\frac{\Delta A_e}{A_e}\right)_{\pi^-,n}$	0.89×10^{-4}	0.63×10^{-4}	0.27×10^{-4}
wide path			
$A_{\pi}^{\text{meas}} \pm \Delta A_{\pi}^{\text{meas}} (\text{total}) (\text{ppm})$	-41.3 ± 12.8	-23.7 ± 21.4	-20.3 ± 6.0
$A_{e,\text{dit}}^{\text{bc,raw}} \pm \Delta A_{e,\text{dit}}^{\text{bc,raw}} (\text{stat.}) (\text{ppm})$	-78.3 ± 2.7	-140.2 ± 10.4	-140.9 ± 6.6
$f_{\pi/e} \pm \Delta f_{\pi/e} (\text{total}) (\times 10^{-4})$	(0.72 ± 0.22)	(1.64 ± 0.17)	(0.92 ± 0.13)
$\left(\frac{\Delta A_e}{A_e}\right)_{\pi^-,w}$	0.54×10^{-4}	0.55×10^{-4}	0.21×10^{-4}

TABLE X: For DIS kinematics: pion asymmetry results A_{π}^{meas} , beam-corrected electron raw asymmetry $A_e^{\text{bc,raw}}$, pion contamination in electron triggers $f_{\pi/e}$, and total uncertainties on the electron asymmetry results due to pion background $(\Delta A_e/A_e)_{\pi^-,n}$ and $(\Delta A_e/A_e)_{\pi^-,w}$, all at the 10^{-4} level.

HRS	Left RES I	Left RES II	Right RES III	Left RES IV	Left RES V
narrow path					
$A_{\pi}^{\text{meas}} \pm \Delta A_{\pi}^{\text{meas}}$ (total) (ppm)	-33.7 ± 88.6	-73.2 ± 48.8	-13.5 ± 12.7	52.2 ± 76.2	-41.5 ± 102.4
$A_{e,\text{dit}}^{\text{bc,raw}} \pm \Delta A_{e,\text{dit}}^{\text{bc,raw}}$ (stat.)	-55.1 ± 6.8	-63.8 ± 5.9	-54.4 ± 4.5	-104.0 ± 15.3	-67.9 ± 21.3
$f_{\pi/e} \pm \Delta f_{\pi/e}$ (total) ($\times 10^{-4}$)	(0.79 ± 0.11)	(2.40 ± 0.20)	(3.82 ± 0.23)	(0.26 ± 0.03)	(0.45 ± 0.03)
$\left(\frac{\Delta A_e}{A_e}\right)_{\pi^-,n}$	1.75×10^{-4}	4.60×10^{-4}	1.85×10^{-4}	0.32×10^{-4}	0.96×10^{-4}
wide path					
$A_{\pi}^{\text{meas}} \pm \Delta A_{\pi}^{\text{meas}}$ (total) (ppm)	-39.8 ± 74.9	-71.0 ± 43.7	-15.8 ± 12.4	58.8 ± 74.7	-47.7 ± 101.4
$A_{e,\text{dit}}^{\text{bc,raw}} \pm \Delta A_{e,\text{dit}}^{\text{bc,raw}}$ (stat.) (ppm)	-54.6 ± 6.8	-63.9 ± 5.9	-54.0 ± 4.5	-104.6 ± 15.3	-67.9 ± 21.5
$f_{\pi/e} \pm \Delta f_{\pi/e}$ (total) ($\times 10^{-4}$)	(0.54 ± 0.15)	(1.50 ± 0.25)	(2.14 ± 0.48)	(0.22 ± 0.03)	(0.32 ± 0.04)
$\left(\frac{\Delta A_e}{A_e}\right)_{\pi^-,w}$	1.13×10^{-4}	2.71×10^{-4}	1.22×10^{-4}	0.28×10^{-4}	0.71×10^{-4}

TABLE XI: For resonance kinematics: pion asymmetry results A_{π}^{meas} , beam-corrected electron raw asymmetry $A_e^{\text{bc,raw}}$, pion contamination in electron triggers $f_{\pi/e}$, and total uncertainties on the electron asymmetry results due to pion background $(\Delta A_e/A_e)_{\pi^-,n}$ and $(\Delta A_e/A_e)_{\pi^-,w}$, all at the 10^{-4} level.

and measure the rate of positrons from the π^0 decay. Due to the low rate of positron events the HRS DAQ could be used for these studies with the VDC and a well-understood PID. However, the statistical uncertainties in the positron asymmetry were quite large due to the very low positron rate. Moreover, the π^+ contamination in the positron trigger was quite high, estimated to be 11% and 20% for the Left DIS#1 and Right DIS#2, respectively, assuming the PID performance of the detector does not depend on the sign of the particles' charge. The measured asymmetry of the pair-production background could not be corrected for the π^+ contamination due to the lack of knowledge on the π^+ asymmetry.

Asymmetries extracted from positive polarity runs are shown in Table XII without corrections for the π^+ background or beam polarization.

HRS	Left DIS#1	Right DIS#2
$A_{e^+}^{\text{raw}}$ (ppm), narrow	$723.2 \pm 1154.7(\text{stat.})$	$1216.0 \pm 1304.5(\text{stat.})$
$A_{e^+}^{\text{raw}}$ (ppm), wide	$742.4 \pm 1151.5(\text{stat.})$	$1199.0 \pm 1304.5(\text{stat.})$

TABLE XII: Raw positron asymmetry results. No correction for the beam position, energy, and polarization, or the π^+ background was made.

Because the statistical uncertainties in the positron asymmetry are so large, we relied on the fact that π^0 must have similar asymmetries as π^- . We assume the π^0 asymmetry to be no larger than twice that of the π^- asymmetry and estimated the uncertainty in the electron asymmetry due to pair production to be:

$$\left(\frac{\Delta A_e}{A_e}\right)_{\text{pair}} = \sqrt{(\Delta f_{e^+/e^-})^2 + \left(f_{e^+/e^-} \frac{\Delta A_{e^+}}{A_e}\right)^2}, \quad (63)$$

where ΔA_{e^+} describes how much A_{e^+} differs from zero and the value $2(|A_{\pi^-}| + \Delta A_{\pi^-})$ was used. Results for f_{e^+/e^-} and their statistical uncertainties are shown in Table XIII, and a 30% uncertainty was used for $\Delta f_{e^+/e^-}$ to account for possible systematic effects in positron identification due to the high π^+ background in the rate evaluation. Results for the electron asymmetry uncertainty due to pair production background are also shown in Table XIII.

There was no measurement for the pair production rate for any resonance kinematics. The value 3×10^{-3} (the average of the uncertainty at DIS#2) was used as the relative uncertainty due to pair production for all resonance asymmetry results. This is a conservative estimate because the π^-/e rate ratios for resonance settings were similar to DIS #1 and are about one order of magnitude smaller than that of DIS#2 (see Table II),

3. Target EndCap Corrections

Electrons scattered off the target aluminum endcaps (Al 7075) cannot be separated from those scattered off the liquid deuterium. The parity-violating asymmetries from aluminum and the alloying elements differ slightly from that of deuterium and a

HRS	Left DIS#1	Left DIS#2	Right DIS#2
$f_{e^+/e^-} \pm \Delta f_{e^+/e^-} \text{ (stat.)}$	$(2.504 \pm 0.007) \times 10^{-4}$	$(5.154 \pm 0.001) \times 10^{-3}$	$(4.804 \pm 0.001) \times 10^{-3}$
$\left(\frac{\Delta A_e}{A_e}\right)_{\text{pair,narrow}}$	4.1×10^{-4}	3.5×10^{-3}	2.3×10^{-3}
$\left(\frac{\Delta A_e}{A_e}\right)_{\text{pair,wide}}$	3.5×10^{-4}	3.7×10^{-3}	2.3×10^{-3}

TABLE XIII: Results for pair production (positron) contamination in the electron trigger f_{e^+/e^-} and its statistical uncertainty, and the total uncertainty on electron asymmetry due to pair production background, $\left(\frac{\Delta A_e}{A_e}\right)_{\text{pair}}$. Only DIS kinematics are shown. The errors shown for f_{e^+/e^-} are statistical only, and a 30% systematic uncertainty on f_{e^+/e^-} was used in the evaluation of $\frac{\Delta A_e}{A_e}$.

correction must be made. Because the Al 7075 alloy is made of $\approx 90\%$ aluminum, we calculate the effect from the aluminum asymmetry below, and the effect from other non-isoscalar elements ($\approx 6\%$ Zn and $\approx 1.4\%$ Cu) was estimated to be $< 8\%$ of that of Al. Based on Eqs. (2-14), the value of parity-violating (PV) asymmetry from e -Al scattering was calculated as

$$A_{\text{Al}} = \frac{13A_p\sigma_p + 14A_n\sigma_n}{13\sigma_p + 14\sigma_n}, \quad (64)$$

where $\sigma_{p(n)}$ is the cross section and $A_{p(n)}$ is the PV asymmetry for scattering off the proton (neutron). The cross sections $\sigma_{p(n)}$ were calculated using a fit to world resonance and DIS data [70]. The asymmetries $A_{p(n)}$ were calculated using Eq. (34):

$$A_p = \left(-\frac{3G_F Q^2}{2\sqrt{2}\pi\alpha}\right) \frac{Y_1 [2C_{1u}(u^+ + c^+) - C_{1d}(d^+ + s^+)] + Y_3 [2C_{2u}(u^-) - C_{2d}(d^-)]}{4(u^+ + c^+) + (d^+ + s^+)}, \quad (65)$$

$$A_n = \left(-\frac{3G_F Q^2}{2\sqrt{2}\pi\alpha}\right) \frac{Y_1 [2C_{1u}(d^+ + c^+) - C_{1d}(u^+ + s^+)] + Y_3 [2C_{2u}(u^-) - C_{2d}(d^-)]}{4(d^+ + c^+) + (u^+ + s^+)}, \quad (66)$$

with $u^\pm \equiv u \pm \bar{u}$, $d^\pm \equiv d \pm \bar{d}$, $s^\pm \equiv s \pm \bar{s}$ and $c^\pm \equiv c \pm \bar{c}$.

The actual aluminum asymmetries A_{Al} may differ from the values calculated using Eq. (64) due to effects such as resonance structure (for resonance kinematics), and nuclear effects similar to the EMC effect of the unpolarized, parity-conserving structure functions $F_{1,2}$ [71].

The EMC effect on aluminum was studied by several experiments [72–74], and data on various nuclei were extrapolated to infinite nuclear matter [75]. (For a recent review of EMC effects see Ref. [76].) For the two DIS kinematics ($x = 0.2 - 0.3$) the EMC effect for Al is approximately 3%. A conservative relative uncertainty of 10% was used for A_{Al} in the DIS kinematics. For resonance kinematics, the EMC effect for Al is in the range (3 – 14)%, and even larger for higher x values. On the other hand, the measured electron asymmetry at all five resonance kinematics were found to be in good agreement (at the 10-15% level) with the values calculated using PDFs [49], and we expect that the uncertainty in A_{Al} due to resonance structure cannot exceed this level. Adding the nuclear and the resonance effects in quadrature, a 20% relative uncertainty was used for A_{Al} in the resonance kinematics.

The fractional event rate from the aluminum endcaps, $\alpha_{\text{Al/D}}$, was calculated as

$$\alpha_{\text{Al/D}} = \eta_{\text{Al/D}} \frac{\sigma_{\text{Al}}}{\sigma_{\text{D}}} \quad (67)$$

where $\eta_{\text{Al/D}}$ is the ratio of the endcap to liquid deuterium thicknesses, and $\sigma_{\text{Al}}/\sigma_{\text{D}}$ is the Al to deuterium per-nucleon cross-sectional ratio from previous measurements [72–74] without the isoscalar correction. The target used for this experiment had entrance and exit endcaps measured to be $0.126 \pm 0.011 \pm 0.003$ mm and $0.100 \pm 0.008 \pm 0.003$ mm thick, respectively (see Table I), with the first error bar from the standard deviation of multiple measurements at different positions on the endcap, and the second error from calibration of the instrument. The ratio $\eta_{\text{Al/D}}$ is $\eta_{\text{Al/D}} = (0.126 + 0.100) \text{ mm} \times (2.7 \text{ g/cm}^3) / (20 \text{ cm} \times 0.167 \text{ g/cm}^3) = 1.827\%$ with an uncertainty of $\Delta\eta_{\text{Al/D}} = 0.115\%$.

The correction to the electron PVDIS asymmetry was applied as

$$A_e^{\text{Al-corrected}} = A_e(1 + \bar{f}_{\text{Al}}), \quad (68)$$

$$\text{with } \bar{f}_{\text{Al}} = -(\alpha_{\text{Al/D}}) \frac{A_{\text{Al}} - A_{\text{D}}}{A_{\text{D}}}. \quad (69)$$

The total uncertainty due to target endcaps is

$$\left(\frac{\Delta A_e}{A_e}\right)_{\text{Al}} = \sqrt{\left(\Delta\alpha_{\text{Al/D}} \frac{A_{\text{Al}} - A_{\text{D}}}{A_{\text{D}}}\right)^2 + [(\delta_{A_{\text{Al}}})\alpha_{\text{Al/D}}]^2} \quad (70)$$

where $\alpha_{\text{Al/D}}$ is from Eq. (67), $\Delta\alpha_{\text{Al/D}} = (\Delta\eta_{\text{Al/D}}/\eta_{\text{Al/D}})\alpha_{\text{Al/D}} = 0.063\alpha_{\text{Al/D}}$, A_{Al} from Eqs.(64-66), A_D from Eq. (32), and $\delta_{A_{\text{Al}}}$ is the maximal relative difference in the Al vs. D₂ PV asymmetries caused by an EMC-like medium modification effect and resonance structures. As stated above, the values $\delta_{A_{\text{Al}}} = 10\%$ for DIS and $= 20\%$ for resonance kinematics were used. Results for the endcap correction \bar{f}_{Al} and the uncertainty on the corrected electron asymmetry are listed in Table XIV. As one can see, the correction due to aluminum is at the 10^{-4} level. The effect from other non-isoscalar alloying elements in Al 7075 was estimated to be at the 10^{-5} level and was neglected in the analysis.

Kinematics	DIS#1	DIS#2	RES I	RES II	RES III	RES IV	RES V
$(A_{\text{Al}} - A_D)/A_D$	0.567%	0.727%	1.335%	0.800	0.510	0.799	0.691
$\alpha_{\text{Al/D}}$	2.0%	2.0%	2.0%	2.0%	2.0%	2.0%	2.0%
$\bar{f}_{\text{Al}} (\times 10^{-4})$	-1.2	-1.5	-2.7	-1.6	-1.0	-1.6	-1.4
$(\Delta A_e/A_e)_{\text{Al}}$	0.24%	0.24%	0.43%	0.43%	0.43%	0.43%	0.43%

TABLE XIV: Target endcap correction for all kinematics. Shown here are the relative differences between calculated Al and D₂ asymmetries, $(A_{\text{Al}} - A_D)/A_D$, the fractional event rate from Al endcaps $\alpha_{\text{Al/D}}$, corrections applied to measured electron asymmetries \bar{f}_{Al} using Eq. (69), and the relative uncertainty in the corrected electron asymmetry due to endcap corrections $(\Delta A_e/A_e)_{\text{Al}}$ using Eq. (70). Here, the Al and D₂ asymmetries were calculated using Eqs. (64,65,66) and the MSTW2008 NLO PDF [87]. Corrections from other non-isoscalar alloying elements in Al 7075 was estimated to be at the 10^{-5} level or smaller, and thus were neglected in the analysis.

Events were also taken on a thick, “dummy” target consisting of two aluminum foils with their thickness approximately 10 times that of the liquid deuterium cell. The thickness was chosen such that the total radiation length of the dummy target matches that of the liquid D₂ target. However, due to limited beam time, the asymmetry uncertainty collected from the aluminum dummy target was not precise enough to reduce the systematic uncertainty due to target endcaps.

4. Beam Transverse Asymmetry Correction

Transverse asymmetry background, also called the beam normal asymmetry background, describes the effect of the electron beam spin polarized in the direction normal to the scattering plane defined by the momentum vectors of the incident and the scattered electrons \vec{k}_e and \vec{k}'_e [77]. This beam normal asymmetry is parity-conserving and must be treated as a background of the measurement. Calculations at the pure partonic level show that this asymmetry is between 0.1-0.2 ppm at the kinematics of this experiment, but mechanisms beyond the parton level can enhance the asymmetry by 1-2 orders of magnitude [78]. The contribution from the beam normal asymmetry A_n to the measured asymmetry can be expressed as

$$\delta A = (A_n) \vec{S} \cdot \hat{k}_n \quad \text{with} \quad \vec{k}_n \equiv \hat{k}_e \times \hat{k}'_e \quad \text{and} \quad \hat{k}_n = \vec{k}_n/|\vec{k}_n|, \quad (71)$$

where A_n is the beam-normal asymmetry and \vec{S} is the beam polarization vector. Denoting θ_0 the central scattering angle of the spectrometer and θ_{tr} the vertical angle of the scattered electron w.r.t. the nominal setting of the spectrometer (see Fig. 16), one has $\hat{k}_e = (0, 0, 1)$ and $\hat{k}'_e = (\sin \theta_0 \cos \theta_{tr}, \sin \theta_0 \sin \theta_{tr}, \cos \theta_0)$, giving $\vec{k}_n = (-\sin \theta_0 \sin \theta_{tr}, \sin \theta_0 \cos \theta_{tr}, 0)$ and $\hat{k}_n = (-\sin \theta_{tr}, \cos \theta_{tr}, 0)$, thus

$$\delta A = A_n [-S_H \sin \theta_{tr} + S_V \cos \theta_{tr}], \quad (72)$$

where $S_{V,H,L}$ are respectively the electron polarization components in the vertical (perpendicular to the nominal scattering plane defined by the electron beam and the central ray of the spectrometer), horizontal (within the nominal plane but transverse to the beam), and longitudinal directions. The value of S_L is thus the beam longitudinal polarization P_b . During the experiment the beam spin components were controlled to $|S_H/S_L| \leq 27.4\%$ and $|S_V/S_L| \leq 2.5\%$ and the average value of θ_{tr} was found from data to be less than 0.01 rad. Therefore the beam vertical spin dominates this background:

$$(\Delta A_e)_{A_n} \approx A_n S_V \cos \theta_{tr} \approx A_n S_V \leq (2.5\%) P_b A_n. \quad (73)$$

During the experiment, the size of the beam normal asymmetry A_n was measured for DIS kinematics during dedicated “transverse runs” where the beam was fully polarized in the vertical direction, $S_H^T = S_L^T \approx 0$ and $S_V = P_{b0}^T$ where the superscript T stands for transverse asymmetry measurement and P_{b0}^T is the maximum beam polarization during such measurement. Asymmetries measured during these runs are thus $A_n^{\text{meas}} = A_n P_{b0}^T$. Because the maximum beam polarization is the same for production and transverse asymmetry running, one has $P_{b0}^T = S_0 \equiv \sqrt{S_L^2 + S_V^2 + S_H^2} = \sqrt{1 + (0.274)^2 + (0.025)^2} S_L = 1.037 S_L$ and the total uncertainty in the electron asymmetry can be calculated as

$$\left(\frac{\Delta A_e}{A_e} \right)_{A_n} = \frac{A_n S_V}{A_e^{\text{meas}}} = \frac{(A_n^{\text{meas}}/S_0) S_V}{A_e^{\text{meas}}} = \frac{A_n^{\text{meas}}}{A_e^{\text{meas}}} \frac{S_V}{S_0} \leq 2.4\% \frac{A_n^{\text{meas}}}{A_e^{\text{meas}}}. \quad (74)$$

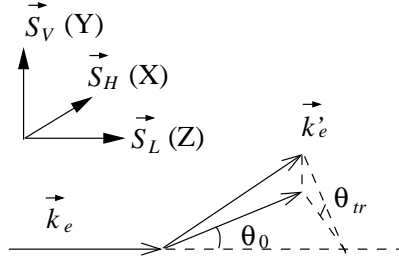


FIG. 16: Kinematics of the beam normal asymmetry background. The incident and the scattered electrons' momenta are \vec{k}_e and \vec{k}'_e , and $\vec{S}_{V,H,L}$ denote respectively the incident electron's spin polarization components in the vertical, horizontal, and longitudinal directions. The central scattering angle setting of the spectrometer is θ_0 and the scattered electron's momentum has an out-of-plane angle denoted by θ_{tr} .

For DIS kinematics, we denote δA_n^{meas} as how much A_n could differ from zero to account for the uncertainty of the A_n measurement, and write

$$\left(\frac{\Delta A_e}{A_e} \right)_{A_n, \text{DIS}} \leq 2.4\% \frac{\delta A_n^{\text{meas}}}{A_e^{\text{meas}}}. \quad (75)$$

If the measured A_n is consistent with zero, the statistical uncertainty of the measurement $\Delta A_n^{\text{meas}}(\text{stat.})$ is taken as δA_n^{meas} , otherwise the value of $(|A_n^{\text{meas}}| + \Delta A_n^{\text{meas}})$ is used as δA_n^{meas} .

Results for the beam transverse asymmetry measurements are shown in Table XV for the two DIS kinematics along with the resulting uncertainty on the electron PVDIS asymmetry due to beam transverse polarizations.

Kinematics Q^2 (GeV/c) ²	Left DIS#1 1.085	Right DIS#2 1.907
$A_n^{\text{meas}} \pm \Delta A_n^{\text{meas}}(\text{stat.})$ (ppm, narrow)	-24.15 ± 15.05	23.49 ± 44.91
A_e^{meas} (ppm, narrow)	78.45	-139.97
$\left(\frac{\Delta A_e}{A_e} \right)_{A_n, \text{narrow}}$	1.18%	0.76%
$A_n^{\text{meas}} \pm \Delta A_n^{\text{meas}}(\text{stat.})$ (ppm, wide)	-24.66 ± 15.01	24.60 ± 44.90
A_e^{meas} (ppm, wide)	78.27	-140.67
$\left(\frac{\Delta A_e}{A_e} \right)_{A_n, \text{wide}}$	1.20%	0.76%

TABLE XV: The measured beam transverse asymmetry together with the resulting uncertainty on the electron asymmetry. The dithering-corrected values were used for both A_e^{meas} and A_n^{meas} . For DIS#2, the electron asymmetry is the combined value from the Left and the Right HRS.

Beam transverse asymmetry measurements were not performed for the resonance kinematics. However, A_n measured in the DIS region has a similar Q^2 dependence and magnitude as that measured in previous elastic electron scattering from the proton and heavier nuclei [77]. This indicates the size of A_n to be determined predominantly by Q^2 , and that the response of the target (elastic vs. DIS) only affects A_n at higher orders. Based on this observation, we used Ref. [77] to calculate A_n for all resonance kinematics. We found A_n to be between -38 and -80 ppm depending on the value of Q^2 , and are always smaller than that of the electron asymmetry. Therefore the uncertainty due to A_n was estimated for resonance kinematics as

$$\left(\frac{\Delta A_e}{A_e} \right)_{A_n, \text{RES}} \approx \left| \frac{A_n S_V}{A_e^{\text{meas}}} \right| = \left| \frac{S_V A_n}{P_b A_e^{\text{phys}}} \right| \leq |S_V / P_b| = |S_V / S_L| = 2.5\%. \quad (76)$$

5. Target Purity, Density Fluctuation and Other False Asymmetries

The liquid deuterium used contained [79] 1889 ppm HD (hydrogen deuteride), < 100 ppm H₂, 4.4 ppm N₂, 0.7 ppm O₂, 1.5 ppm CO, < 1 ppm methane and 0.9 ppm CO₂. The only non-negligible effect on the measured asymmetry comes from the proton in HD. Since the proton asymmetry as given by Eq. (65) differs from the asymmetry of the deuteron by no more than $\pm(15 - 30)\%$, the proton in HD contributes an uncertainty of $(\Delta A_e / A_e)_{\text{HD}} < 0.06\%$ to the measured electron asymmetry.

6. Rescattering and Poletip Scattering Background

In this section, two kinds of backgrounds from rescattering inside the HRS spectrometers are considered. The first is due to electrons from outside the HRS momentum acceptance which rescatter into the detector. The second effect is called “poletip scattering”, which refers to electrons which scattered from polarized electrons (Møller scattering) in the magnetized iron in the HRS dipoles. These backgrounds are suppressed by a factor of 10 compared to the estimates given in Ref. [19] because of our trigger threshold for the lead-glass detector.

Using Eq. (57), the correction to our asymmetry for both cases can be written as

$$\bar{f}_{rs} = -\frac{f_{rs}\Delta A}{A^{\text{meas}}}, \quad (77)$$

where f_{rs} is the fraction of the rescattering background and $\Delta A = A^{\text{bgr}} - A^{\text{meas}}$ is the difference between the background's asymmetry and the measured asymmetry. The correction can be evaluated by integrating over the energy that contribute to this background:

$$f_{rs}\Delta A = \frac{1}{\Delta E_{\text{HRS}}} \int_{\text{outside}} dE \frac{P_{rs}(E) P_{\text{thr}}\left(\frac{d\sigma}{d\Omega dE}\right)_{\text{outside}} (A^{\text{bgr}} - A^{\text{meas}})}{\left(\frac{d\sigma}{d\Omega dE}\right)_{\text{inside}}}, \quad (78)$$

where ΔE_{HRS} is the HRS energy acceptance, P_{rs} is the rescattering probability that describes the relative contribution of rescattered events among all events that reach the detectors, P_{thr} is the probability for rescattered events that reach the detectors to pass the trigger threshold and cause an electron trigger, and $\left(\frac{d\sigma}{d\Omega dE}\right)_{\text{inside(outside)}}$ is the scattering cross section inside (outside) the HRS acceptance. The integration is done from just outside the spectrometer acceptance (beyond $\pm 4\%$) to up to $\pm 20\%$ of the nominal setting E'_0 . The upper limit of 20% is used because the function $P_{rs}(E)$ becomes negligible beyond this range.

The rescattering probability $P_{rs}(E)$ was measured by the HAPPEX experiment [19], and the results are shown in Fig. 17. The probability drops to below 10^{-3} just outside the HRS acceptance (4%) and quickly to 10^{-6} at 20%. Although only the positive detune ($\delta p/p > 0$) was measured, we assumed the distribution is symmetric around the nominal momentum of the spectrometer. The trigger threshold factor $P_{\text{thr}} \approx 0.1$ is estimated from the location of the trigger threshold for our lead glass detector. The

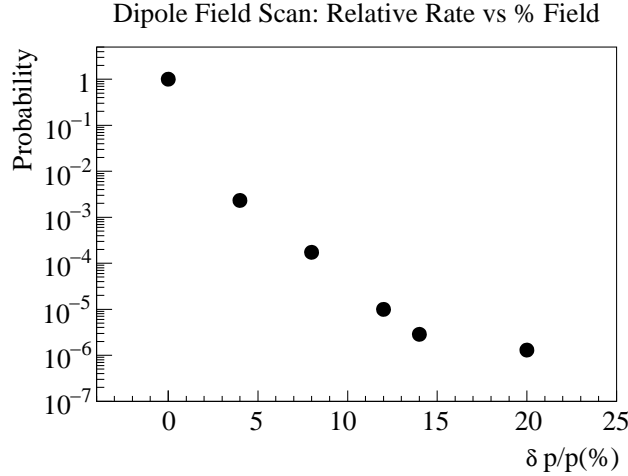


FIG. 17: The function $P_{rs}(E)$ determined from HAPPEX data.

parity-violating asymmetry scales with Q^2 and we found that $\bar{f}_{rs} \ll 2 \times 10^{-5}$.

In Ref. [19] an upper bound for the poletip scattering effect was found. Using that analysis, and without accounting for the further suppression by our trigger thresholds, we estimate that

$$\bar{f}_{\text{pole-tip}} < \frac{0.3 \text{ ppm}}{A^{\text{meas}}}. \quad (79)$$

Because the effects from rescattering and pole-tip scattering are both small, no correction to the asymmetry was made and these two effects were counted as additional systematic uncertainties.

H. Electromagnetic Radiative Corrections

Electrons undergo radiative energy losses due to interactions such as internal and external bremsstrahlung and ionization loss, both before and after the scattering. This causes two effects on the measurement: 1) There is a small beam depolarization effect associated with the energy loss of incident electrons; 2) the energy loss of both incident and scattered electrons would cause a difference between the kinematics reconstructed from the detected signals and what really happened at the interaction point. We discuss these two effects separately.

1. Beam Depolarization Effect in Bremsstrahlung

The depolarization of electron from bremsstrahlung radiation was calculated based on Ref. [80] and the formalism is provided in Appendix B. We define a depolarization correction

$$f_{\text{depol}} = \frac{\langle A_e D \rangle}{\langle A_e \rangle} \quad (80)$$

where D is the beam depolarization factor (with zero depolarization corresponding to $D = 100\%$) and the average of a quantity $\langle a \rangle$ ($a = A_e$ or $A_e D$) is taken over the spectrometer acceptance and the cross section σ :

$$\langle a \rangle \equiv \frac{\int_{\text{HRS}} a \cdot \sigma \cdot (\text{acceptance})}{\int_{\text{HRS}} \sigma \cdot (\text{acceptance})}. \quad (81)$$

The measured asymmetry should be corrected as

$$A^{\text{depol-corrected}} = A_e^{\text{meas}} (1 + \bar{f}_{\text{depol}}), \quad (82)$$

where $\bar{f}_{\text{depol}} \equiv (1/f_{\text{depol}}) - 1 \approx \langle A_e \rangle / \langle A_e D \rangle - 1$. An HAMC simulation was done to determine the value of \bar{f}_{depol} and the results are shown in Table XVI.

Kinematics	DIS#1	DIS#2	RES I	RES II	RES III	RES IV	RES V
\bar{f}_{depol}	0.096%	0.209%	0.005%	0.028%	0.093%	0.061%	0.081%

TABLE XVI: Beam depolarization correction \bar{f}_{depol} for all kinematics.

2. Corrections for Vertex versus Detected Kinematics

Due to energy losses of the electrons, the kinematics at the interaction vertex is not the same as those calculated from the initial beam energy and the electron's momentum detected by the spectrometer. This effect is illustrated in Fig. 18: since the shift between detected and vertex kinematics relies heavily on the experimental setup, it is desired to correct the measured asymmetry for this effect such that the corrected values can be compared to theoretical expectations in an unambiguous way. This correction factor is defined as:

$$1 + \bar{f}_{\text{rc}} = \frac{A(\langle Q_{\text{det}}^2 \rangle, \langle x_{\text{det}} \rangle)}{\langle A(Q_{\text{vtx}}^2, x_{\text{vtx}}) \rangle}, \quad (83)$$

and is applied to the measured asymmetry as:

$$A_e^{\text{rad-corrected}} = A_e^{\text{meas}} (1 + \bar{f}_{\text{rc}}). \quad (84)$$

Here $A(\langle Q_{\text{det}}^2 \rangle, \langle x_{\text{det}} \rangle)$ is the asymmetry calculated at the cross-section- and acceptance-weighted values [see Eq. (81)] of Q_{det}^2 and x_{det} , evaluated from the initial beam energy and the detected electrons momentum, and $\langle A(Q_{\text{vtx}}^2, x_{\text{vtx}}) \rangle$ is the asymmetry still averaged over all detected electrons following Eq. (81), but now calculated using the vertex kinematics Q_{vtx}^2 and x_{vtx} of each event. Since the value $\langle A(Q_{\text{vtx}}^2, x_{\text{vtx}}^2) \rangle$ is the expected value of what was actually measured in the experiment (A_e^{meas}), the result $A_e^{\text{rad-corrected}}$ can be treated as the value corresponding to $\langle Q_{\text{det}}^2 \rangle$ and $\langle x_{\text{det}} \rangle$. The value of $A_e^{\text{rad-corrected}}$ can thus be compared with theoretical calculations evaluated at $\langle Q_{\text{det}}^2 \rangle$ and $\langle x_{\text{det}} \rangle$ to extract physics results.

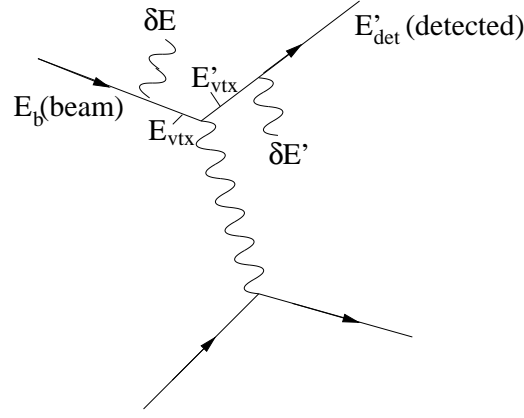


FIG. 18: Kinematics used in HAMC to correct energy losses δE and $\delta E'$ for the incoming and outgoing electrons respectively. The kinematics reconstructed from the data corresponds to E_{beam} and E'_{det} , while the vertex kinematics corresponds to E_{vtx} and E'_{vtx} .

The radiative correction was evaluated using HAMC which calculates both the numerator and the denominator of Eq. (83). Therefore, we expect that any small imperfection in the understanding of the HRS acceptance or cross-section calculation, such as that indicated by the 2 standard-deviation disagreement in Q^2 between HAMC and data for RES III, would cancel out to the first order, and does not lead to a larger uncertainty in the radiative correction for this kinematics. The treatment of radiative effects was based on the prescription of Mo & Tsai [81]. The detailed procedure is described below.

For each simulated event, the scattering angle θ and the momentum of the scattered electron E'_{vtx} at the vertex were generated randomly. The energy loss of incoming and outgoing electrons δE and $\delta E'$ were then calculated using the formula given on page 5-7 of Ref. [82], which includes external bremsstrahlung, internal bremsstrahlung using the effective radiator formula, and ionization loss. Next, the incoming electron's energy at the vertex is calculated as $E_{\text{vtx}} = E_b - \delta E$ where E_b is the (fixed) initial beam energy and the detected momentum of the scattered electron calculated as $E'_{\text{det}} = E'_{\text{vtx}} - \delta E'$. If θ and E'_{det} fell within the spectrometer acceptance, the cross section and the PV asymmetry were calculated using both the detected ($E_b, E_{\text{det}}, \theta$) and the vertex kinematics ($E_{\text{vtx}}, E'_{\text{vtx}}, \theta$) and were stored.

The vertex kinematics ($Q^2_{\text{vtx}}, W_{\text{vtx}}$) calculated using ($E_{\text{vtx}}, \theta, E'_{\text{vtx}}$) is shown in Fig. 19 for the two DIS kinematics. One can see that the vertex kinematics of an event could fall into one of the following categories: $e^-^2\text{H}$ elastic ($W < M$ with M the proton mass, quasi-elastic ($W \approx M$), nucleon resonances ($M \lesssim W < 2 \text{ GeV}$), and DIS ($W > 2 \text{ GeV}$). To evaluate the PV

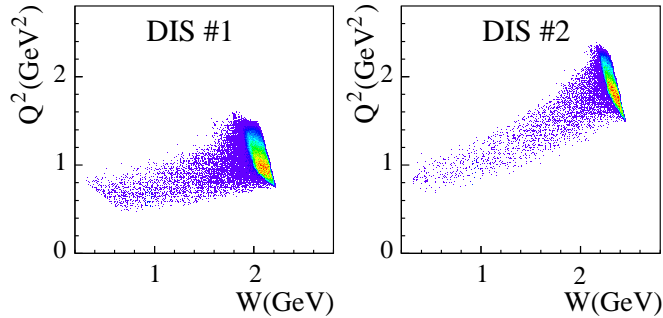


FIG. 19: (Color online) Simulated vertex kinematics of the two DIS kinematics #1 (left) and #2 (right).

asymmetries for different vertex kinematics, the following prescription was used:

1. For $e^-^2\text{H}$ elastic scattering, the method from the SAMPLE experiment [14] was used, where the cross section was based on Ref. [83] and the PV asymmetry was based on a simple model that compares well to the calculation of Ref. [84]. The strange magnetic form factor G_M^s in this method was taken to be zero.
2. For quasi-elastic scattering, the cross section and the asymmetry were calculated using the elastic scattering formula and elastic form factors for the neutron and the proton [see Section VII of Ref. [19]], then smeared for their Fermi motion following the algorithm of Ref. [70]. The quasi-elastic (qe) PV asymmetry was then calculated as $A_d^{\text{qe}} =$

$(A_p^{\text{el}}\sigma_p^{\text{el}} + A_n^{\text{el}}\sigma_n^{\text{el}})/(\sigma_p^{\text{el}} + \sigma_n^{\text{el}})$ where $A_{p(n)}^{\text{el}}$ and $\sigma_{p(n)}^{\text{el}}$ are the elastic asymmetry and cross section for the proton (neutron), respectively.

3. For the nucleon resonance region ($1 \lesssim W < 2$ GeV), the cross section was based on Ref. [70], and the asymmetries were calculated from three models: one theoretical model for the $\Delta(1232)$ [85], a second theoretical model that covers the whole resonance region [86], and one “cross-section-scaling model” where $A_{\text{res}} = \frac{\sigma_{\text{res}}}{\sigma_{\text{dis}}} A_{\text{dis}}$ was used. Here A_{dis} was calculated from Eqs. (2, 6,7,10,11,12, 13,14) with MSTW2008 PDFs [87], σ_{dis} was calculated using the NMC fit of F_2 [88] structure functions and R from Ref. [70], and σ_{res} was from Ref. [70] which exhibits distinct resonance structures; The cross-section-scaling model was used only when the theoretical models do not cover the kinematics of a particular event.
4. For DIS ($W > 2$ GeV), the cross section was calculated using Bosted’s fits [70] and the PV asymmetry was calculated using Eqs. (2, 6,7,10,11,12, 13,14) with MSTW2008 PDFs [87]. For R in Eq. (7) again Ref. [70] was used.

The physics inputs to HAMC for $e-^2\text{H}$ elastic, quasi-elastic, DIS, as well as the cross sections were all based on existing data and the uncertainties are small. The uncertainty of the correction was thus dominated by that from the resonance asymmetry models. The validity of these models were evaluated by comparing the measured asymmetries from the resonance kinematics, RES I through IV, with calculations from these models. The kinematic coverage of resonance measurements is shown in Fig. 20. These resonance asymmetries were reported in Ref. [49], and it was found that the data agree well with both resonance models [85, 86] except RES I. Results at RES I agreed with the two models at the two standard deviation level. The uncertainty from the resonance models was taken to be either the observed difference between resonance data and model, or the statistical uncertainty of the resonance asymmetry measurement, whichever is larger. This gives different model uncertainties as follows:

- For $W^2 < 1.96$ (GeV)² or the $\Delta(1232)$ region: RES I locates primarily in this region. The observed 25% relative discrepancy between RES I data and the calculation was used as the model uncertainty in this region;
- For $1.96 < W^2 < 3.0$ (GeV)²: RES II locates primarily in this region. Since the RES II asymmetry result agreed well with both models, the 10.0% relative statistical uncertainty of the RES II asymmetry was used as the model uncertainty in this region.
- For $3.0 < W^2 < 4.0$ (GeV)²: Both RES III and IV locate in this region. Since the agreement with the calculations was well within the statistical uncertainties, the relative uncertainties for RES III and IV (8.9% and 15.4% respectively) were combined, and the resulting value of 7.7% was used as the model uncertainty in this region.

For radiative corrections at DIS kinematics, the resonance models affect the denominator, but not the numerator of Eq. (83). Therefore the above model uncertainty affects directly the DIS corrections. These uncertainties were combined with the fractional events whose vertexes fell within the corresponding W region to estimate the uncertainty on $\langle A(Q_{\text{vtx}}^2, x_{\text{vtx}}) \rangle$ and \bar{f}_{rc} . For radiative corrections at resonance kinematics, the resonance models affect both the denominator and the numerator of Eq. (83). The uncertainty of the model itself therefore cancels out in principle in the correction factor \bar{f}_{rc} . For resonance kinematics, a conservative 20% relative uncertainty was used for \bar{f}_{rc} .

The radiative correction factor $1 + \bar{f}_{\text{rc}}$ obtained from the above procedure is shown in Table XVII for the two models separately. The average value of the two models were applied to the measured asymmetries of this experiment.

I. Box Diagram Corrections

Box diagram corrections refer to effects that arise when the electron simultaneously exchanges two bosons ($\gamma\gamma$, γZ , or ZZ box) with the target, and are dominated by the $\gamma\gamma$ and the γZ box diagrams. For PVES asymmetries, the box diagram effects include those from the interference between Z -exchange and the $\gamma\gamma$ box, the interference between γ -exchange and the γZ box, and the effect of the $\gamma\gamma$ box on the electromagnetic cross sections. It is expected that there is at least partial cancellation among these three terms. The box-diagram corrections were applied as

$$A^{\text{box-corrected}} = (1 + \bar{f}_{\text{box}}) A_e^{\text{meas}}. \quad (85)$$

Corrections for the $\gamma\gamma$ box effect to the measured electron asymmetry were estimated to be $\bar{f}_{\gamma\gamma\text{box}} = -0.002$ and -0.003 for DIS #1 and #2, respectively. For these DIS kinematics, the effects of the γZ and ZZ boxes were treated as part of the electroweak radiative corrections and will be described in Sec. IV D 1 [Eqs. (86-89)]. For resonance kinematics, the combined corrections for $\gamma\gamma$ and γZ boxes (i.e. the full box correction) were estimated to be $\bar{f}_{\gamma\gamma, \gamma Z\text{boxes}} = +0.005$. A relative 100% uncertainty was used for all box-diagram corrections.

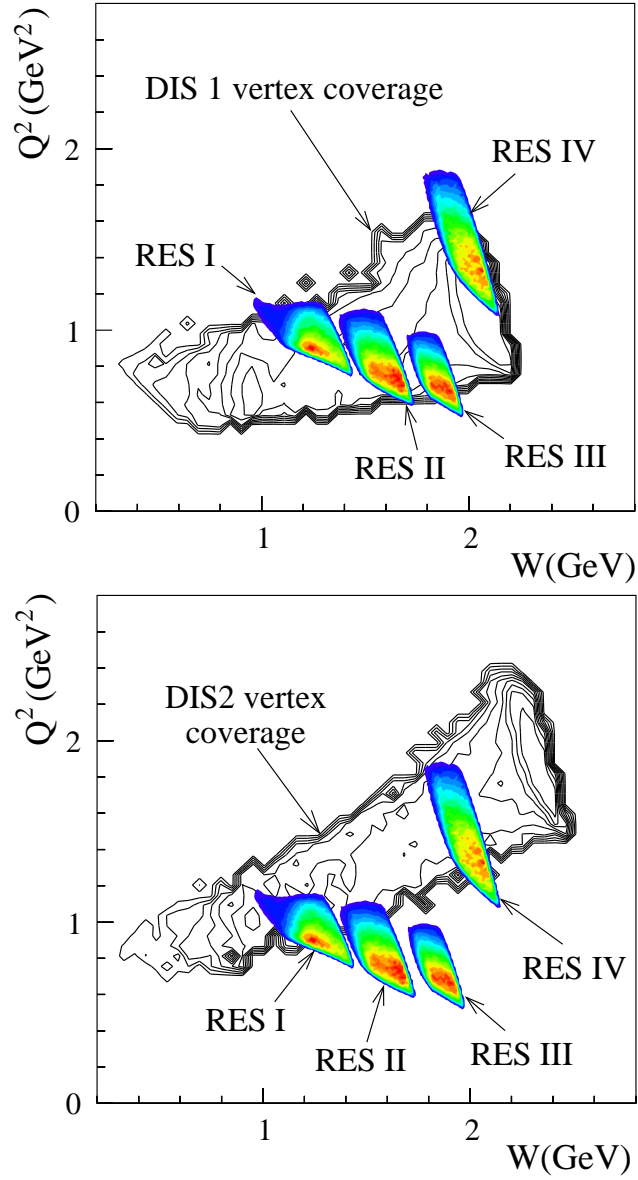


FIG. 20: (*Color online*) Kinematics coverage of the four resonance measurements (colored contours), compared with the DIS vertex kinematics (black contours).

IV. RESULTS

A. Asymmetry results for both DIS and resonance settings

Table XVIII presents the measured asymmetries along with their kinematics, all corrections, and the final physics asymmetry results. The x and Q^2 values were obtained from the data and therefore were weighted by the scattering cross section. The dithering-corrected asymmetries were used as $A^{\text{bc,raw}}$ and the difference between dithering and regression methods were used as the systematic uncertainty of $A^{\text{bc,raw}}$ (see Table IV). In addition to the corrections and uncertainties presented in Sections III E through III I, deadtime corrections from Ref. [54] were also applied to the asymmetries. We chose asymmetries measured by the narrow triggers of the DAQ as $A^{\text{bc,raw}}$ because of the smaller counting deadtime and the associated uncertainty. All corrections were applied using Eq. (58). The largest corrections are due to beam polarization, DAQ deadtime, and electromagnetic radiative corrections. The largest uncertainties come from the beam normal asymmetry and determination of the Q^2 values. We also note that the pair-production background, though very small for the present experiment, causes an uncertainty typically one order of

Kinematics	Resonance Models used	$A(\langle Q_{\text{det}}^2 \rangle, \langle x_{\text{det}}^2 \rangle)$ ppm	$\langle A(Q_{\text{vtx}}^2, x_{\text{vtx}}^2) \rangle$ ppm	$1 + \bar{f}_{rc}$	$1 + \bar{f}_{rc}$ average
DIS #1	Ref. [85]	-88.6	-86.8	1.021 ± 0.020	1.015 ± 0.021
	Ref.[86]	-88.6	-87.8	1.009 ± 0.020	
DIS #2	Ref. [85]	-159.6	-156.6	1.019 ± 0.004	1.019 ± 0.0043
	Ref.[86]	-159.6	-156.7	1.019 ± 0.004	
RES I	Ref. [85]	-93.4	-82.2	1.137 ± 0.027	1.1095 ± 0.0352
	Ref.[86]	-89.0	-82.2	1.082 ± 0.016	
RES II	Ref. [85]	-65.5	-65.5	1.0002 ± 0.0000	1.0205 ± 0.0207
	Ref.[86]	-71.1	-68.3	1.0408 ± 0.0082	
RES III	Ref. [85]	-58.6	-59.1	0.9930 ± 0.0014	1.0005 ± 0.0076
	Ref.[86]	-62.5	-62.0	1.0079 ± 0.0016	
RES IV	Ref. [85]	-117.5	-116.7	1.0063 ± 0.0013	1.0170 ± 0.0112
	Ref.[86]	-123.7	-120.4	1.0276 ± 0.0055	
RES V	Ref. [85]	-103.9	-101.4	1.0241 ± 0.0048	1.0134 ± 0.0110
	Ref.[86]	-103.9	-103.6	1.0027 ± 0.0005	

TABLE XVII: Radiative correction factors. For each kinematics, the simulated asymmetries using two resonance models are shown. In kinematic regions where the resonance models are not available, the cross-section-scaling model was used. These asymmetries were input to Eq. (83) to obtain the radiative correction factors. Results from the two models were averaged to provide the final correction $1 + \bar{f}_{rc}$, and the difference between the two was combined with uncertainties of resonance models themselves to provide the total uncertainty on \bar{f}_{rc} .

magnitude larger than that from the charged pion background because one cannot reject pair-production background with PID detectors.

B. Group trigger asymmetry results for resonance kinematics

The asymmetry data taken in the resonance region are of particular value: they provided the first PVES asymmetries over the complete nucleon resonance region, and the first test of quark-hadron duality for electroweak observables. For nucleon resonance studies, fine-binning in W is often desired to reveal detailed resonance structure. As described in Ref. [54], in addition to the so-called global electron triggers that lead to the main results presented in the previous section, the detector package was divided into groups, for which group electron triggers were constructed, and data recorded in the same way as global triggers. Settings RES I, II, IV and V on the left HRS had six groups, while setting RES III on the right HRS had eight groups. The kinematics coverage varies between group triggers, providing different coverage in W . Figure 21 shows the Q^2 and W coverage of the six groups for setting RES I. As one can see, the Q^2 range is similar but the W coverages of the six groups are different.

Because there were overlaps in the detector grouping of the DAQ (that is, some lead glass blocks were used as inputs to two group triggers), approximately (10-30)% events were recorded simultaneously by two adjacent groups and the group trigger events were not completely uncorrelated. Nevertheless, asymmetries extracted for individual groups allowed a study of the W -dependence of the asymmetry. Corrections to the raw asymmetry from group triggers were applied in the same manner presented in the previous section. Among all corrections, two corrections were expected to vary among groups to an observable level, and must be evaluated carefully for individual groups: deadtime (rate-dependent) and electromagnetic radiative corrections (kinematic-dependent). All other corrections either do not depend on groups, or their kinematic variation is expected to be well below the statistical uncertainty of the measurement.

Tables XIX and XX show respectively for the left and the right HRS: the average kinematics $\langle W \rangle$ and $\langle Q^2 \rangle$, the raw measured asymmetries, the two group-dependent corrections for individual groups, and the physics asymmetry results. Corrections and uncertainties that do not depend on groups are the same as in Table XVIII. Similar to DIS results, we used the dithering-corrected asymmetries measured from the narrow path triggers of the DAQ as raw-asymmetry inputs to the analysis because the narrow path had smaller counting deadtime and associated uncertainties.

C. Test of quark-hadron duality using resonance PV asymmetries

Figure 22 shows the W -dependence of the group-trigger resonance asymmetry results A_{PV}^{phys} of Tables XIX and XX, scaled by $1/Q^2$. The data of adjacent bins in each kinematics typically have a 20-30% overlap and are thus correlated, while the lowest

Kinematics								
	DIS#1	Left DIS#2	Right DIS#2	RES I	RES II	RES III	RES IV	RES V
E_b (GeV)	6.067	6.067		4.867	4.867	4.867	6.067	6.067
θ_0	12.9°	20.0°		12.9°	12.9°	12.9°	15.0°	14.0°
E'_0 (GeV)	3.66	2.63		4.00	3.66	3.10	3.66	3.66
$\langle Q^2 \rangle_{\text{data}} [(\text{GeV}/c)^2]$	1.085	1.901		0.950	0.831	0.757	1.472	1.278
$\langle x \rangle_{\text{data}}$	0.241	0.295		0.571	0.335	0.228	0.326	0.283
$\langle W \rangle_{\text{data}}$ (GeV)	2.073	2.330		1.263	1.591	1.857	1.981	2.030
Y_3	0.434	0.661		0.340	0.353	0.411	0.467	0.451
R_V	0.808	0.876		—	—	—	—	—
$Y_3 R_V$	0.351	0.579		—	—	—	—	—
$A^{\text{bc,raw}}$ (ppm)	−78.45	−140.30	−139.84	−55.11	−63.75	−54.38	−104.04	−67.87
(stat.)	±2.68	±10.43	±6.58	±6.77	±5.91	±4.47	±15.26	±21.25
(syst.)	±0.07	±0.16	±0.46	±0.10	±0.15	±0.24	±0.26	±0.72
Corrections with systematic uncertainties								
P_b	88.18%	89.29%	88.73%	90.40%	90.40%	90.40%	89.65%	89.65%
ΔP_b	±1.76%	±1.19%	±1.50%	±1.54%	±1.54%	±1.54%	±1.24%	±1.24%
$1 + \bar{f}_{\text{depol}}$	1.0010	1.0021		1.0005	1.0003	1.0009	1.0006	1.0008
(syst.)	$< 10^{-4}$	$< 10^{-4}$		$< 10^{-4}$	$< 10^{-4}$	$< 10^{-4}$	$< 10^{-4}$	
$1 + \bar{f}_{\text{Al}}$	0.9999	0.9999	0.9999	0.9997	0.9998	0.9999	0.9998	0.9999
(syst.)	±0.0024	±0.0024	±0.0024	±0.0043	±0.0043	±0.0043	±0.0043	±0.0043
$1 + \bar{f}_{\text{dt}}$	1.0147	1.0049	1.0093	1.0148	1.0247	1.0209	1.0076	1.0095
(syst.)	±0.0009	±0.0004	±0.0013	±0.0006	±0.0023	±0.0041	±0.0004	0.0007
$1 + \bar{f}_{\text{rc}}$	1.015	1.019		1.1095	1.0205	1.0005	1.0170	1.0134
(syst.)	±0.020	±0.004		±0.0352	±0.0207	±0.0076	±0.0112	0.0110
$1 + \bar{f}_{\gamma\gamma\text{box}}$	0.998	0.997	—	—	—	—	—	—
$1 + \bar{f}_{\gamma\gamma,\gamma Z\text{boxes}}$	—	—	1.005	1.005	1.005	1.005	1.005	1.005
(syst.)	±0.002	±0.003	±0.005	±0.005	±0.005	±0.005	±0.005	±0.005
Systematic uncertainties $\Delta A^{\text{phys}}/A^{\text{phys}}$ with no correction								
charged pion	±9 × 10 ^{−5}	±6 × 10 ^{−5}	±3 × 10 ^{−5}	±1.8 × 10 ^{−4}	±4.6 × 10 ^{−4}	±1.9 × 10 ^{−4}	±3 × 10 ^{−5}	±1.0 × 10 ^{−4}
pair production	±0.0004	±0.004	±0.002	±0.003	±0.003	±0.003	±0.003	±0.003
beam A_n	±0.025	±0.025	±0.025	±0.025	±0.025	±0.025	±0.025	±0.025
Q^2	±0.0085	±0.0064	±0.0065	±0.0081	±0.0073	±0.008	±0.035	±0.037
rescattering	≪ 0.002	≪ 0.002	≪ 0.002	≪ 0.002	≪ 0.002	≪ 0.002	≪ 0.002	≪ 0.002
target impurity	±0.0006	±0.0006	±0.0006	±0.0006	±0.0006	±0.0006	±0.0006	±0.0006
Asymmetry Results								
A^{phys} (ppm)	−91.10	−160.80		−68.62	−73.75	−61.49	−118.97	−77.50
(stat.)	±3.11	±6.39		±8.43	±6.84	±5.05	±17.45	±24.27
(syst.)	±2.97	±3.12		±3.26	±2.78	±2.06	±5.54	±3.84
(total)	±4.30	±7.12		±9.04	±7.38	±5.46	±18.31	±24.57

TABLE XVIII: Asymmetry results on $\bar{e}-^2\text{H}$ parity-violating scattering from the PVDIS experiment at JLab. The DIS results were previously published in Ref. [48]. The kinematics shown include the beam energy E_b , central angle and momentum settings of the spectrometer θ_0 , E'_0 , the actual kinematics averaged from the data (cross-section-weighted) $\langle Q^2 \rangle$ and $\langle x \rangle$, the kinematics factor Y_3 [calculated using $\langle Q^2 \rangle$, $\langle x \rangle$, E_b and Eq. (2)], the PDF valence quark distribution function ratio R_V calculated from MSTW2008 [87] Leading-Order parameterization and Eq. 31, and the product $Y_3 R_V$ that provides the lever arm for isolating the C_{2q} contribution to the asymmetry. The electron asymmetries obtained from the narrow trigger of the DAQ with beam dithering corrections, $A^{\text{bc,raw}}$, were corrected for the effects from the beam polarization P_b and many systematic effects including: the beam depolarization effect \bar{f}_{depol} , the target aluminum endcap \bar{f}_{Al} , the DAQ deadtime \bar{f}_{dt} [54], the radiative correction \bar{f}_{rc} that includes effects from energy losses of incoming and scattered electrons as well as the spectrometer acceptance and detector efficiencies, and the box-diagram correction $\bar{f}_{\gamma\gamma\text{box}}$ (for DIS) and $\bar{f}_{\gamma\gamma,\gamma Z\text{boxes}}$ (for resonances). Systematic effects that do not require a correction to the asymmetry include: the charged pion and the pair production background, the beam normal asymmetry, the uncertainty in the determination of Q^2 , the re-scattering background, and the target impurity. Final results on the physics asymmetries A^{phys} are shown with their statistical, systematic, and total uncertainties.

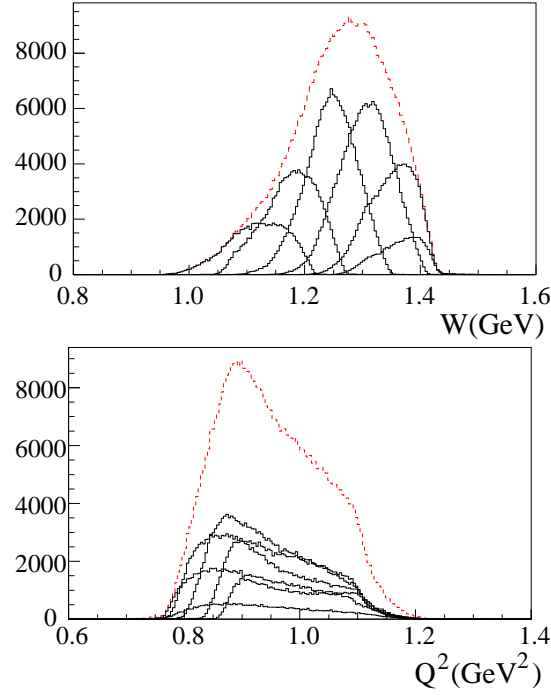


FIG. 21: (Color online) Event distributions in W (top) and Q^2 (bottom) for the six DAQ groups taken at setting RES I. The coverage in W increases monotonously from group 1 to 6. The red dashed histogram shows the global trigger events.

and the highest bins of each kinematics have larger overlaps with their adjacent bins. Figure 22 illustrates that all asymmetry data are consistent with the three resonance models and with the DIS estimation. No significant resonance structure is observed in the W -dependence of the asymmetries.

The agreement with DIS-based calculations indicates that quark-hadron duality holds for PVES asymmetries on the deuteron at the (10 – 15)% level throughout the resonance region, for Q^2 values just below 1 (GeV/c)². These results are comparable to the unpolarized electromagnetic structure function data which verified duality at the (5 – 10)% level for the proton and (15 – 20)% for the neutron at similar Q^2 values, although the unpolarized measurements provided better resolution in W and covered a broader kinematic range [40, 41, 45].

D. Extraction of electron-quark effective coupling C_{2q} from DIS asymmetries

1. Calculation of PVDIS asymmetry sensitivity to C_{2q}

In order to extract the electron-quark VA couplings C_{2q} , one must first study the sensitivity of the measured PVDIS asymmetry to C_{2q} . Equation 2 was used for this purpose. In this section, inputs to Eq. 2 will be explained in detail, including all physical constants and couplings and the structure function evaluation. Uncertainties due to higher twist effects will be discussed at the end.

Electroweak radiative corrections were applied to all couplings used in the calculation of the asymmetry. The electromagnetic fine structure constant α was evolved to the measured Q^2 -values from $\alpha_{EM}|_{Q^2=0} = 1/137.036$ [52]. The evaluation takes into account purely electromagnetic vacuum polarization. The Fermi constant is $G_F = 1.1663787(6) \times 10^{-5} \text{ GeV}^{-2}$ [52]. The $C_{1q,2q}$ were evaluated using Table 7 and Eq. (114-115) of Ref. [91] at our measured Q^2 -values in the modified minimal subtraction ($\overline{\text{MS}}$) scheme using a fixed Higgs mass $M_H = 125.5 \text{ GeV}$:

$$C_{1u}^{\text{SM}} = -0.1887 - 0.0011 \times \frac{2}{3} \ln(\langle Q^2 \rangle / 0.14 \text{ GeV}^2) \quad (86)$$

$$C_{1d}^{\text{SM}} = 0.3419 - 0.0011 \times \frac{-1}{3} \ln(\langle Q^2 \rangle / 0.14 \text{ GeV}^2) \quad (87)$$

$$C_{2u}^{\text{SM}} = -0.0351 - 0.0009 \ln(\langle Q^2 \rangle / 0.078 \text{ GeV}^2) \quad (88)$$

$$C_{2d}^{\text{SM}} = 0.0248 + 0.0007 \ln(\langle Q^2 \rangle / 0.021 \text{ GeV}^2) \quad (89)$$

Group	1	2	3	4	5	6
RES I						
$\langle Q^2 \rangle_{\text{data}} [(\text{GeV}/c)^2]$	0.992	0.966	0.948	0.940	0.931	0.940
$\langle W \rangle_{\text{data}} (\text{GeV})$	1.119	1.175	1.245	1.305	1.350	1.364
$A_{\text{dit}}^{\text{bc,raw}} (\text{ppm})$	-30.84	-57.65	-54.01	-46.12	-60.24	-95.49
(stat.)	18.31	14.34	11.51	11.33	14.41	23.85
$1 + \bar{f}_{\text{dt}}$	1.0077	1.0089	1.0105	1.0106	1.0088	1.0069
(syst.)	0.0004	0.0009	0.0004	0.0010	0.0008	0.0009
$1 + \bar{f}_{rc}$	1.359	1.150	1.045	1.024	1.011	1.010
(syst.)	0.155	0.031	0.014	0.005	0.004	0.004
$A^{\text{phys}} (\text{ppm})$	-46.95	-74.35	-63.37	-53.05	-68.26	-107.89
(stat.)	± 27.87	± 18.49	± 13.50	± 13.03	± 16.33	± 26.95
(syst.)	± 7.42	± 3.36	± 2.26	± 1.77	± 2.26	± 3.58
(total)	± 28.84	± 18.80	± 13.69	± 13.15	± 16.48	± 27.18
RES II						
$\langle Q^2 \rangle_{\text{data}} [(\text{GeV}/c)^2]$	0.856	0.849	0.834	0.820	0.808	0.819
$\langle W \rangle_{\text{data}} (\text{GeV})$	1.503	1.533	1.583	1.629	1.662	1.672
$A_{\text{dit}}^{\text{bc,raw}} (\text{ppm})$	-60.67	-55.15	-77.16	-65.46	-65.92	-61.73
(stat.)	13.24	11.18	10.55	10.57	12.95	20.71
$1 + \bar{f}_{\text{dt}}$	1.0134	1.0152	1.0160	1.0158	1.0135	1.0107
(syst.)	0.0008	0.0017	0.0006	0.0014	0.0012	0.0015
$1 + \bar{f}_{rc}$	1.032	1.017	1.012	1.000	0.995	0.995
(syst.)	0.006	0.003	0.002	< 0.001	0.001	0.001
$A^{\text{phys}} (\text{ppm})$	-70.56	-63.31	-88.21	-73.94	-73.91	-69.02
(stat.)	± 15.40	± 12.83	± 12.06	± 11.94	± 14.52	± 23.16
(syst.)	± 2.35	± 2.09	± 2.89	± 2.42	± 2.42	± 2.26
(total)	± 15.58	± 13.00	± 12.40	± 12.18	± 14.72	± 23.27
RES IV						
$\langle Q^2 \rangle_{\text{data}} [(\text{GeV}/c)^2]$	1.531	1.533	1.473	1.442	1.427	1.378
$\langle W \rangle_{\text{data}} (\text{GeV})$	1.901	1.922	1.978	2.020	2.049	2.071
$A_{\text{dit}}^{\text{bc,raw}} (\text{ppm})$	-103.29	-91.13	-82.82	-117.19	-142.95	87.30
(stat.)	32.87	32.21	27.24	27.00	37.52	96.85
$1 + \bar{f}_{\text{dt}}$	1.0057	1.0057	1.0061	1.0061	1.0055	1.0049
(syst.)	0.0003	0.0004	0.0003	0.0004	0.0004	0.0003
$1 + \bar{f}_{rc}$	1.013	1.013	1.020	1.027	1.031	1.032
(syst.)	0.003	0.003	0.004	0.005	0.006	0.006
$A^{\text{phys}} (\text{ppm})$	-118.02	-104.13	-95.32	-135.81	-166.21	101.54
(stat.)	± 37.56	± 36.80	± 31.35	± 31.29	± 43.62	± 112.65
(syst.)	± 5.43	± 4.79	± 4.39	± 6.28	± 7.70	± 4.71
(total)	± 37.95	± 37.11	± 31.66	± 31.91	± 44.30	± 112.75

TABLE XIX: From left HRS group triggers: $\langle W \rangle$ and $\langle Q^2 \rangle$ from data (cross-section weighted), beam-(dithering-)corrected raw asymmetries from narrow triggers, and group-dependent corrections. Corrections and uncertainties that do not depend on groups are the same as in Table XVIII and are not shown here. After all corrections are applied, the final asymmetries are shown in the last row for each setting.

and it is expected that the uncertainty is negligible. Equations (86-89) include the “charge radius effect” and an estimate of the interference between γ -exchange and the γZ box, but not the effect from the $\gamma\gamma$ box. The effect from the $\gamma\gamma$ box was applied as a correction to the measured asymmetry as described in previous sections.

To express the measured asymmetries in terms of $2C_{1u} - C_{1d}$ and $2C_{2u} - C_{2d}$, we calculated the $F_{1,3}^{\gamma,\gamma^Z}$ structure functions in Eqs. (2, 10, 11) and the resulting $a_{1,3}$ contribution to the asymmetry, see Table XXI. Here the approximation $Y_1 = 1$ was used, which is valid if $R^\gamma = R^{\gamma^Z}$. Also shown in Table XXI are values of $2C_{1u} - C_{1d}$ and $2C_{2u} - C_{2d}$ evaluated at the Q^2 -values of

Group	1	2	3	4	5	6	7	8
RES III								
$\langle Q^2 \rangle_{\text{data}} [(\text{GeV}/c)^2]$	0.731	0.719	0.730	0.744	0.761	0.777	0.796	0.799
$\langle W \rangle_{\text{data}} (\text{GeV})$	1.928	1.923	1.905	1.880	1.851	1.820	1.790	1.771
$A_{\text{dit}}^{\text{bc,raw}} (\text{ppm})$	-58.62	-38.74	-56.02	-56.74	-56.67	-57.15	-52.57	-35.99
(stat.)	26.82	13.05	9.95	9.57	9.58	9.97	11.13	24.24
$1 + \bar{f}_{\text{dt}}$	1.0127	1.0148	1.0169	1.0174	1.0173	1.0170	1.0161	1.0127
(syst.)	0.0011	0.0010	0.0011	0.0010	0.0010	0.0010	0.0011	0.0012
$1 + \bar{f}_{rc}$	1.022	1.021	1.024	1.026	1.025	1.024	1.020	1.010
(syst.)	0.004	0.004	0.005	0.005	0.005	0.005	0.004	0.002
$A^{\text{phys}} (\text{ppm})$	-67.50	-44.66	-64.90	-65.90	-65.75	-66.22	-60.62	-40.96
(stat.)	± 30.88	± 15.05	± 11.53	± 11.12	± 11.12	± 11.55	± 12.83	± 27.59
(syst.)	± 2.25	± 1.49	± 2.17	± 2.21	± 2.20	± 2.21	± 2.02	± 1.36
(total)	± 30.97	± 15.12	± 11.73	± 11.33	± 11.33	± 11.76	± 12.99	± 27.62

TABLE XX: From right HRS group triggers: $\langle W \rangle$ and $\langle Q^2 \rangle$ from data (cross-section-weighted), beam-(dithering-)corrected raw asymmetries from narrow triggers, and group-dependent corrections. Corrections and uncertainties that do not depend on groups are the same as in Table XVIII and are not shown here. After all corrections are applied, the final asymmetries are shown in the last row for each setting. We did not perform a group analysis for setting RES V because of the very-low statistics.

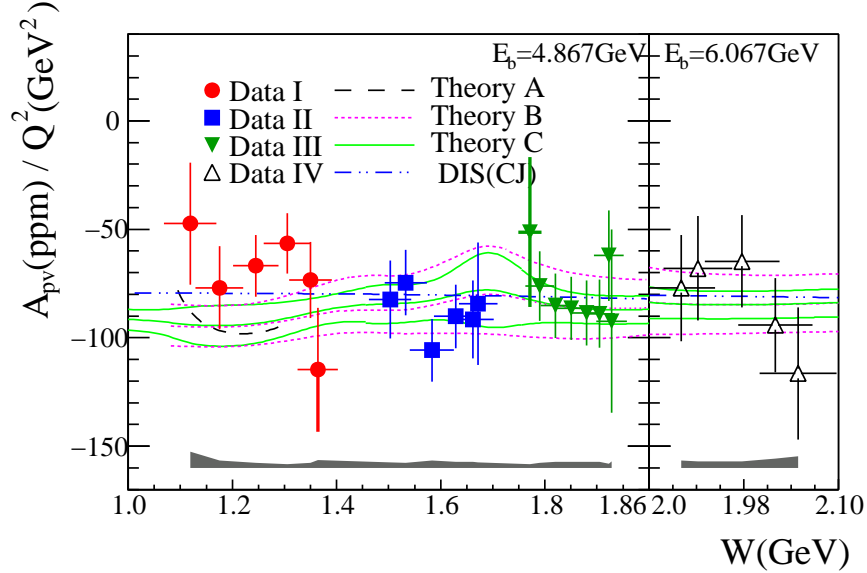


FIG. 22: (Color online) From Ref. [49]: W -dependence of the parity-violating asymmetries in $\vec{e}-^2\text{H}$ scattering in the nucleon resonance region. The physics asymmetry results A_{PV}^{phys} for the four kinematics RES I, II, III and IV (solid circles, solid squares, solid triangles, and open triangles, respectively), in parts per million (ppm), are scaled by $1/Q^2$ and compared with calculations from Ref. [85] (Theory A, dashed), Ref. [86] (Theory B, dotted), Ref. [89] (Theory C, solid) and the DIS estimation (dash-double-dotted) using Eq. (32) with the extrapolated CJ PDF [90]. The vertical error bars for the data are statistical uncertainties, while the horizontal error bars indicate the root-mean-square values of the W coverage of each bin. The experimental systematic uncertainties are shown as the shaded bands at the bottom. For each of the four kinematics, calculations were performed at the fixed E_b and Q^2 values of each of the RES I, II, III and IV settings and with a variation in W to match the coverage of the data. Theories B and C each have three curves showing the central values and the upper and the lower bounds of the calculation. Uncertainties of the DIS calculation were below 1 ppm and are not visible.

the measurement. Three different parton distribution functions (PDFs) were used: the CTEQ/JLab (“CJ”) fit [90] which provides structure functions at the next-to-leading order (NLO), the CT10 [92] (NLO only), and the leading-order (LO) MSTW2008 [87] fits. The CT10 and the MSTW2008 provide only PDF values but not the structure functions. For these two fits the quark-parton model (QPM) [Eqs. (12-14)] was used to calculate structure functions from PDFs. The parametrization most suitable for our kinematics is the CJ fit, and it provides three different sets: the medium (mid), minimum, and maximum. However the CJ fit is not applicable for Q^2 -values below 1.7 (GeV/c)^2 . From the $Q^2 = 1.901 \text{ (GeV/c)}^2$ comparison we found that the result of the LO MSTW2008 fit is closest to CJ, therefore it was used to interpret the $Q^2 = 1.085 \text{ (GeV/c)}^2$ result. Results in Table XXI were also used for uncertainty estimation: the variation between various fits (three fits for $Q^2 = 1.901 \text{ (GeV/c)}^2$ and two fits for $Q^2 = 1.085 \text{ (GeV/c)}^2$) are at the level of relative 0.5% for the a_1 term and relative 5% for the a_3 term of the asymmetry. The “valence quark only” values [Eq. (33)] are also shown in Table XXI. These values differ from the PDF-based calculation by not more than 2% and 20% for the a_1 and the a_3 terms respectively, which explains in part why the calculations are in-sensitive to the choice of the PDF fits.

	$\langle Q^2 \rangle = 1.085,$ $\langle x \rangle = 0.241$	$\langle Q^2 \rangle = 1.901,$ $\langle x \rangle = 0.295$
Physical couplings used in the Calculation		
$\alpha_{EM}(Q^2)$	1/134.45	1/134.20
C_{1u}^{SM}	-0.1902	-0.1906
C_{1d}^{SM}	0.3427	0.3429
$2C_{1u}^{\text{SM}} - C_{1d}^{\text{SM}}$	-0.7231	-0.7241
C_{2u}^{SM}	-0.0375	-0.0380
C_{2d}^{SM}	0.0276	0.0280
$2C_{2u}^{\text{SM}} - C_{2d}^{\text{SM}}$	-0.1025	-0.1039
a_1, a_3 terms in A_{SM} , in ppm		
“valence quark only”	-83.07, -5.11	-145.49, -14.28
CTEQ/JLab (CJ) full fit, mid	NA	-147.37, -12.12
min	NA	-147.41, -12.99
max	NA	-147.40, -13.07
“PDF+QPM” MSTW2008 LO	-83.61, -4.13	-146.43, -12.48
“PDF+QPM” CT10 (NLO)	-84.06, -4.35	-146.64, -12.89
coefficients for $2C_{1u} - C_{1d}, 2C_{2u} - C_{2d}$ in A_{SM} , in ppm		
“valence quark only”	114.88, 49.82	200.92, 137.51
CTEQ/JLab (CJ) full fit, mid	NA	203.52, 116.68
min	NA	203.58, 125.01
max	NA	203.56, 125.78
“PDF+QPM” MSTW2008 LO	115.63, 40.26	202.22, 120.08
“PDF+QPM” CT10 (NLO)	116.25, 42.41	202.51, 124.08

TABLE XXI: From Supplemental Tables of Ref. [48]: Comparison of Standard-Model (SM) prediction for the asymmetry, A_{SM} , using different structure functions: LO MSTW2008 [87], (NLO) CT10 [92], and the CTEQ/JLab (CJ) [90] fits. The CJ fits include 3 sets – middle, minimal, and maximal – to provide the nominal value of the PDF and the uncertainties. Values for $\alpha_{EM}(Q^2)$ were calculated using $\alpha_{EM}(Q^2 = 0) = 1/137.036$. The weak couplings at the measured Q^2 -values, $C_{1,2}^{\text{SM}}(Q^2)$, were based on Table 7 and Eq. (114-115) of Ref. [91].

As can be seen from Eq. (27, 28), the $a_{1,3}$ terms of the asymmetry are proportional to the $C_{1,2}$ couplings, respectively. This proportionality, i.e. the coefficient for $2C_{1u} - C_{1d}$ or $2C_{2u} - C_{2d}$ in the asymmetry, describes quantitatively the sensitivity to these couplings. To interpret the asymmetry results for both Q^2 values consistently, we used the MSTW2008 LO values in Table XXI as the nominal values and found for DIS setting #1, $A_{\text{SM}} = -87.7 \pm 0.7$ ppm where the uncertainty is dominated by that from the PDFs. The sensitivity to the effective couplings is

$$A_{\text{SM}} = (115.63 \text{ ppm})(2C_{1u} - C_{1d}) + (40.26 \text{ ppm})(2C_{2u} - C_{2d}) \quad (90)$$

$$= (1.156 \times 10^{-4}) [(2C_{1u} - C_{1d}) + 0.348(2C_{2u} - C_{2d})] \quad (91)$$

For DIS setting #2, $A_{\text{SM}} = (-158.9 \pm 1.0)$ ppm and

$$A_{\text{SM}} = (202.22 \text{ ppm})(2C_{1u} - C_{1d}) + (120.08 \text{ ppm})(2C_{2u} - C_{2d}) \quad (92)$$

$$= (2.022 \times 10^{-4}) [(2C_{1u} - C_{1d}) + 0.594(2C_{2u} - C_{2d})]. \quad (93)$$

The uncertainties in the sensitivity to $2C_{1u} - C_{1d}$ and $2C_{2u} - C_{2d}$ are 0.5% and 5%, respectively, as described in the previous paragraph. The resulting uncertainty in the $2C_{2u} - C_{2d}$ extraction due to the PDF fits is $\Delta(2C_{2u} - C_{2d})(\text{PDF}) = \pm 0.011$.

The above calculation used the approximation that $Y_1 = 1$ which is valid if $R^\gamma = R^{\gamma Z}$. The effect of possible differences between $R^{\gamma Z}$ and R^γ was studied in Ref. [93]: to account for a shift of 1 ppm in the asymmetry, 7.7% and 4.5% differences between $R^{\gamma Z}$ and R^γ are needed, for DIS settings #1 and #2, respectively. Such large differences were considered highly unlikely and the uncertainty in the asymmetry due to the possible difference between $R^{\gamma Z}$ and R^γ was considered to be negligible compared to the statistical uncertainties of the measurement.

The higher-twist (HT) effects refer to the interaction between quarks inside the nucleon at low Q^2 , where QCD perturbation theory breaks down. At a relatively low Q^2 , but not low enough for the effective QCD coupling to diverge, the HT effects introduce a $1/Q^2$ -dependence to the structure functions in addition to the $\ln Q^2$ perturbative QCD evolution. The HT effects modify the PVDIS asymmetry through a change in the absorption cross-section ratio R^γ in Eqs. (6,7), or through changes in the structure function ratios a_1 and a_3 of Eq. (11). The effect on R^γ was estimated in Ref. [94] and was found to be negligible. Studies of the HT effects on the PVDIS asymmetry through changes in the structure functions can be dated back to the SLAC E122 experiment [95, 96], where it was argued that the HT effects on the a_1 term of the asymmetry are very small. The most recent discussions on HT effects of the PVDIS asymmetry, represented by work in Refs. [97–99], indicated that the HT contribution to the a_1 term is at or below the order of $0.5\%/Q^2$ for the x range of this experiment, where Q^2 is in units of $(\text{GeV}/c)^2$.

There is no theoretical estimation of the HT effects on the a_3 term of the asymmetry. However, this term is bounded by data on the neutrino structure function H_3^ν [94], which has the same quark content as $F_3^{\gamma Z}$. If applying the observed H_3^ν higher-twist Q^2 -dependence to $F_3^{\gamma Z}$ alone, one expects the asymmetry to shift by +0.7 ppm and +1.2 ppm for DIS#1 and #2, respectively. We used these values as the uncertainty in the a_3 term due to HT effects.

Overall, a combination of theoretical and experimental bounds on the HT effects indicate that they do not exceed 1% of our measured asymmetry. The uncertainties in the a_1 and the a_3 terms due to HT were evaluated separately, and the corresponding uncertainty in $2C_{2u} - C_{2d}$ is ± 0.012 , and is quite small compared to the experimental uncertainties.

2. Global fit to effective couplings C_{1q} and C_{2q}

Including the two DIS points obtained by our experiment, there are enough data to perform a simultaneous fit to the three linear combinations of effective couplings, $C_{1n} \equiv C_{1u} + 2C_{1d}$, $2C_{1u} - C_{1d}$, and $2C_{2u} - C_{2d}$. To do this, we used the constraint extracted from atomic parity violation in Cs [32] as quoted in Ref. [91],

$$188 C_{1u} + 211 C_{1d} = 36.35 \pm 0.21, \quad (94)$$

where we relied on the most recent atomic structure calculation in Ref. [35]. We also employed the latest C_{1q} result from Ref. [31]:

$$2 C_{1u} + C_{1d} - 0.0004 = -0.032 \pm 0.006, \quad (95)$$

where the small adjustment on the left-hand side is from the electron charge radius [91]. Finally, we included the 11 data points of the SLAC–E122 experiment [9]. For the E122 asymmetries, we employed Eq. (32) with $\alpha = \alpha(Q^2)$ and $R_C = 0$, while the values of R_S and R_V are shown in Table XXII. To account for the different Q^2 values of these measurements, we adjusted the effective couplings using Eq. (86–89). Note that these corrections were applied to our DIS points as well, see Table XXI.

There are various E122 point-to-point errors which we added in quadrature (following the original publication [9]), and then we added the result again quadratically to the statistical errors (rather than linearly as in Ref. [9]). In addition, the polarization uncertainty was common to all data points. This resulted in a 5% correlated uncertainty in the scale of the asymmetries. We constructed the corresponding covariance matrix and included it in our fits.

As for the two DIS points of the present experiment, we erred on the conservative side and approximated their systematic (see Table XVIII) and theory uncertainties as fully correlated. The latter are composed of PDF uncertainties of 0.76% and errors originating from higher twist (quark-quark correlation) effects. The higher twist uncertainties enter separately and uncorrelated for the a_1 and the a_3 terms. As explained in the previous section, the HT uncertainty on a_1 term was taken to be $0.5\%/Q^2$ with Q^2 in $(\text{GeV}/c)^2$, or 0.39 ppm averaged over DIS#1 and #2, and that for the a_3 term was estimated from H_3^ν data to be 0.7 ppm and 1.2 ppm, respectively, for DIS#1 and DIS#2.

We then obtain the best fit result and correlation matrix,

$$\begin{array}{c|ccc} C_{1u} + 2C_{1d} = & 0.489 \pm 0.005 & 1.00 & -0.94 & 0.42 \\ 2C_{1u} - C_{1d} = & -0.708 \pm 0.016 & -0.94 & 1.00 & -0.45 \\ 2C_{2u} - C_{2d} = & -0.145 \pm 0.068 & 0.42 & -0.45 & 1.00 \end{array} \quad (96)$$

where the χ^2 per degree of freedom is 17.3/12, corresponding to a 14% probability. These results are shown in Fig. 23. Figure 23

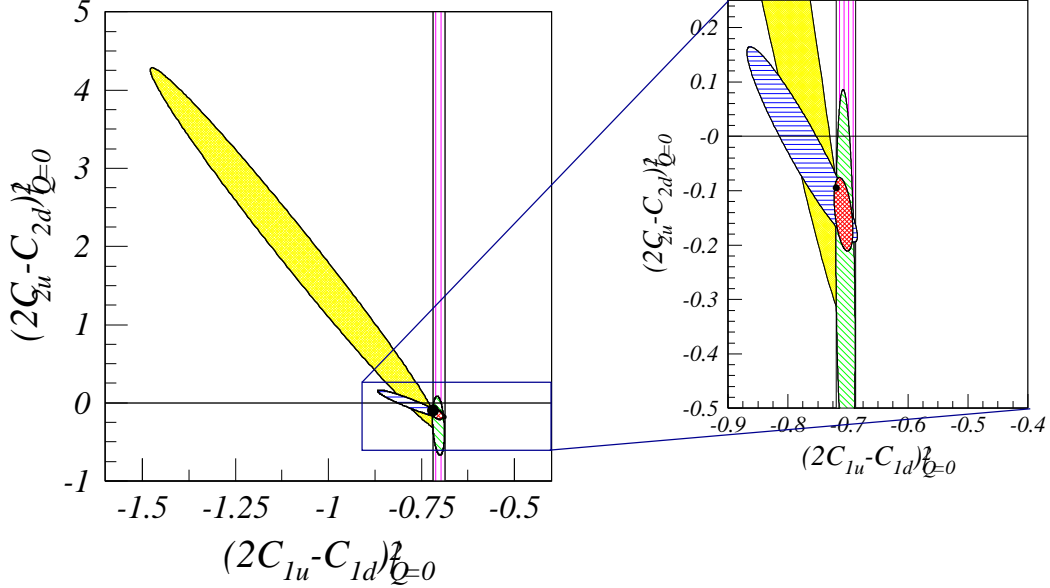


FIG. 23: (Color online) From Ref. [48]: results on $(2C_{1u} - C_{1d})|_{Q^2=0}$ and $(2C_{2u} - C_{2d})|_{Q^2=0}$ from the present experiment. The right panel shows an enlarged view with the vertical and the horizontal axis at the same scale. The new results (blue horizontal-line-hatched ellipse) are compared with SLAC E122 (yellow ellipse) [8, 9]. A fit to the latest data on C_{1q} [31] (from PVES and Atomic Cs [32–35]) is shown as the magenta vertical-line-hatched band. The green slanted-line-hatched ellipse shows a fit to the combined result of SLAC E122 and the latest C_{1q} , while the red line-cross-hatched ellipse shows a fit to the combined result of SLAC E122, the present experiment, and the latest C_{1q} . The Standard Model value $2C_{2u} - C_{2d}|_{Q^2=0} = -0.0950 \pm 0.0004$ is shown as the black dot, where the size of the dot is for visibility.

shows our results have greatly improved the uncertainty on the effective coupling $C_{2u,2d}$ and are in good agreement with the Standard Model prediction. The result on C_{2q} alone is [48]

$$(2C_{2u} - C_{2d})|_{Q^2=0} = -0.145 \pm 0.066 \text{ (exp.)} \pm 0.011 \text{ (PDF)} \pm 0.012 \text{ (HT)} \quad (97)$$

$$= -0.145 \pm 0.068 \text{ (total)}. \quad (98)$$

We note that this is the first time we observe the combination $(2C_{2u} - C_{2d})$ to be non-zero at the two standard deviation level. Because the C_{2q} is axial-vector in nature at the quark vertex, the result of Eq. (98) can be interpreted as the first direct evidence that quarks do exhibit a chirality preference when interacting with electrons through the neutral weak force [100].

3. Extracting mass limits

A comparison of the present result on $C_{1q,2q}$ with the Standard Model prediction can be used to set mass limits Λ below which new interactions are unlikely to occur. For the cases of electron and quark compositeness, we used the conventions from Ref. [101] and the procedure followed by the LEP 2 Collaborations, described in Ref. [102]. The new-physics effective Lagrangian for eq interactions is given by [101]

$$\mathcal{L}_{eq} = \frac{g^2}{\Lambda^2} \sum_{i,j=L,R} \eta_{ij} \bar{e}_i \gamma_\mu e_i \bar{q}_j \gamma^\mu q_j, \quad (99)$$

where Λ is defined [101] for strong coupling, *i.e.* relative to $g^2 = 4\pi$. For $\eta_{LL} = \eta_{RL} = -\eta_{LR} = -\eta_{RR} = 1$, and adding the SM contribution, one then obtains

$$\mathcal{L}_{eq} = \left[\frac{G_F}{\sqrt{2}} C_{2q}(\text{SM}) + \frac{g^2}{\Lambda^2} \right] \bar{e} \gamma_\mu e \bar{q} \gamma^\mu \gamma^5 q \quad (100)$$

$$\equiv \frac{C_{2q}(\text{SM}) + \delta C_{2q}(\text{new})}{2v^2} \bar{e} \gamma_\mu e \bar{q} \gamma^\mu \gamma^5 q \equiv \frac{C_{2q}}{2v^2} \bar{e} \gamma_\mu e \bar{q} \gamma^\mu \gamma^5 q, \quad (101)$$

where $\delta C_{2q}(\text{new})$ is the deviation in C_{2q} from the SM value that may be related to beyond-the-SM physics, and the quantity $v = (\sqrt{2} G_F)^{-1/2} = 246.22 \text{ GeV}$ is the Higgs vacuum expectation value which sets the electroweak scale.

If a measurement of the effective coupling, C_{2q} , or a fit to some data set, finds a central value \bar{C}_{2q} , then the best estimate of the new physics contribution would be given by

$$\frac{g^2}{\Lambda^2} = \frac{4\pi}{\Lambda^2} = \frac{\bar{C}_{2q} - C_{2q}(\text{SM})}{2v^2}. \quad (102)$$

For the expected (projected) limits, one assume $\bar{C}_{2q} = C_{2q}(\text{SM})$, in which case the 90% confidence-level (CL) central range for C_{2q} is given by

$$-1.645 \Delta C_{2q} < \delta C_{2q}(\text{new}) < 1.645 \Delta C_{2q}, \quad (103)$$

where ΔC_{2q} is the total (statistical + systematic + theoretical) 1σ uncertainty from the extraction. The endpoints of this range can be interpreted as the 95% CL upper and lower limits of C_{2q} . However, it is conventional to consider the two possible sign choices of g^2/Λ^2 as two different “models”, quoting two separate limits, Λ_\pm . Half of the probability distribution is then excluded by construction and one has to renormalize the remaining part. This amounts to the 95% CL:

$$|\delta C_{2q}(\text{new})| < 1.96 \Delta C_{2q}. \quad (104)$$

In the general case, $\bar{C}_{2q} \neq C_{2q}(\text{SM})$, we find instead the 95% CL limits,

$$|C_{2q}|^\pm = \pm [\bar{C}_{2q} - C_{2q}(\text{SM})] + \sqrt{2} \Delta C_{2q} \text{erf}^{-1} \left[0.95 \mp 0.05 \text{erf} \left(\frac{\bar{C}_{2q} - C_{2q}(\text{SM})}{\sqrt{2} \Delta C_{2q}} \right) \right],$$

where

$$\text{erf}(x) \equiv \frac{2}{\sqrt{\pi}} \int_0^x dt e^{-t^2} \quad (105)$$

is the Gauss error function and $\text{erf}^{-1}(x)$ its inverse.

A complication arises if a given observable or data set (such as the case at hand) is not sensitive to a specific flavor operator. In the case where u and d quarks are involved, we can rewrite,

$$\mathcal{L}_{eu} + \mathcal{L}_{ed} = \frac{\bar{e} \gamma_\mu e}{2v^2} [C_{2u} \bar{u} \gamma^\mu \gamma^5 u + C_{2d} \bar{d} \gamma^\mu \gamma^5 d], \quad (106)$$

in terms of two rotated operators,

$$\begin{aligned} \mathcal{L}_{eu} + \mathcal{L}_{ed} &= \frac{\bar{e} \gamma_\mu e}{2v^2} (\cos \xi C_{2u} + \sin \xi C_{2d}) (\cos \xi \bar{u} \gamma^\mu \gamma^5 u + \sin \xi \bar{d} \gamma^\mu \gamma^5 d) \\ &+ \frac{\bar{e} \gamma_\mu e}{2v^2} (-\sin \xi C_{2u} + \cos \xi C_{2d}) (-\sin \xi \bar{u} \gamma^\mu \gamma^5 u + \cos \xi \bar{d} \gamma^\mu \gamma^5 d). \end{aligned} \quad (107)$$

For example, in the operator basis in which

$$\tan \xi = -\frac{1}{2},$$

Eq. (107) becomes

$$\begin{aligned} \mathcal{L}_{eu} + \mathcal{L}_{ed} &= \frac{\bar{e} \gamma_\mu e}{2v^2} \frac{(2C_{2u} - C_{2d})}{\sqrt{5}} \frac{(2\bar{u} \gamma^\mu \gamma^5 u - \bar{d} \gamma^\mu \gamma^5 d)}{\sqrt{5}} \\ &+ \frac{\bar{e} \gamma_\mu e}{2v^2} \frac{(C_{2u} + 2C_{2d})}{\sqrt{5}} \frac{(\bar{u} \gamma^\mu \gamma^5 u + 2\bar{d} \gamma^\mu \gamma^5 d)}{\sqrt{5}}. \end{aligned} \quad (108)$$

Experiments in PVDIS on isoscalar targets are only sensitive to the operator in the first line of Eq. (108). The same applies to the analogously defined rotation angle between the couplings C_{1u} and C_{1d} . In this case, the second line turns out to be proportional to the weak charge of the neutron. In other words, the weak charge of the neutron (but not that of the proton) contains exactly orthogonal information to that provided by our experiment.

We determined the combination, $2\bar{C}_{2u} - \bar{C}_{2d}$, in the last line of the fit result in (96). Currently, the SM prediction is $[2C_{2u} - C_{2d}](\text{SM}) = -0.0949$, and so the new physics scale corresponding to this operator is bounded (at the 95% CL) by,

$$\Lambda_+ > v \sqrt{\frac{\sqrt{5} 8\pi}{|2C_{2u} - C_{2d}|^+}} = v \sqrt{\frac{\sqrt{5} 8\pi}{0.104}} = 5.7 \text{ TeV}, \quad (109)$$

$$\Lambda_- > v \sqrt{\frac{\sqrt{5} 8\pi}{|2C_{2u} - C_{2d}|^-}} = v \sqrt{\frac{\sqrt{5} 8\pi}{0.170}} = 4.5 \text{ TeV}. \quad (110)$$

Results on the new mass limits are shown in Fig. 24. The improvement on the C_{2q} mass limit is approximately a factor of $\sqrt{5}$. We note that while collider experiments have set higher limits on new compositeness that are vector-electron and axial-vector-quark in nature, their observables are sensitive to a combination of different chiral structures, and such limits can only be derived by assuming all other chiral terms are zero. Such an assumption is not necessary for the present experiment since we measured C_{2q} directly. Equations (109-110) provide model-independent mass limits on the electron-quark VA contact interactions and should be satisfied by any model of new physics.

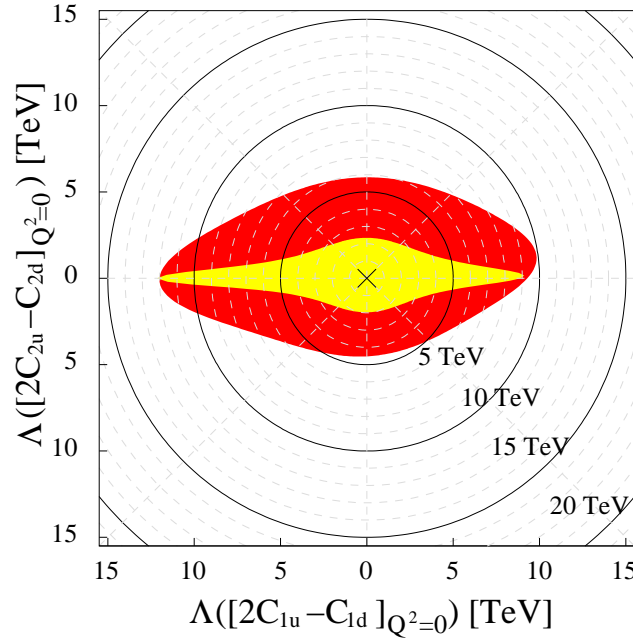


FIG. 24: (Color online) From Ref. [48]: Mass exclusion limits on the electron and quark compositeness and contact interactions obtained from the zero- Q^2 values of $2C_{1u} - C_{1d}$ and $2C_{2u} - C_{2d}$ at the 95% confidence level. The yellow contour shows the limit obtained from SLAC E122 asymmetry results [8, 9] combined with the best C_{1q} values [31]. The red contour shows the limit with our new results added.

V. SUMMARY

In this paper we document the PVDIS experiment performed at Jefferson Lab using the 6 GeV longitudinally-polarized electron beam. We archive the experimental setup, the data analysis procedure, all corrections applied to the asymmetry, and all asymmetry results. Asymmetry results from DIS settings (Table XVIII) were used to extract the electron-quark effective couplings $C_{1q,2q}$ and the associate mass limits on new contact interactions. These DIS results have been published in Ref.[48]. Our results on C_{2q} improved over existing data by a factor of five and agreed well with the Standard Model prediction. They also showed for the first time that $2C_{2u} - C_{2d}$ is non-zero at the two standard-deviation level, indicating that the parity-violating asymmetry measured in electron deep inelastic scattering does receive a contribution from the quarks' chiral preference in neutral

weak interaction. Mass limits on new electron-quark VA contact interactions were extracted from our $2C_{2u} - C_{2d}$ result, and have improved over existing limits from PVES by a factor $\sqrt{5}$. Our mass limits are valid for all new electron-quark contact interactions that have the VA chiral structure, and are complementary to limits obtained from collider experiments.

Asymmetries in the nuclear resonance region are reported in Table XVIII and their W -dependence in Tables XIX and XX. These results were published previously in Ref. [49]. Our resonance asymmetry results are in good agreement with theoretical predictions. They also agree well with DIS calculations extended to our kinematics, and do not show distinct resonance structure. This indicates that quark-hadron duality works for PVES asymmetries at the 10-15% level.

We also report on parity-violating asymmetries of inclusive pion production (Tables VIII and IX), pair production (Table XII), and beam-normal asymmetries (Table XV). The results are useful for background evaluation for other PVES experiments, including those planned for the JLab 12 GeV program.

Appendix A: Re-analysis of E122 asymmetry results

To study the sensitivity of the E122 asymmetry results to C_{2q} couplings, we show these kinematics in Table XXII including the values for Y_3 and R_V . Calculations of R_V were based on the MSTW2008 parameterization [87] of the parton distribution functions. Also shown are the simplified value of Y_3 which were used in the original analysis [9]:

$$Y_3^{\text{simplified}} = \frac{1 - (1 - y)^2}{1 + (1 - y)^2}, \quad (\text{A1})$$

and which we continued to use in this re-analysis. Note, however, that the use of Eq. (A1) tends to overestimate the already small sensitivity to the C_{2q} . Equation (32) illustrates that the product $Y_3 R_V$ provides the lever arm to isolate the C_{2q} contribution to the asymmetry. The relatively small values and coverage of $Y_3 R_V$ in E122 were largely due to the small and fixed scattering angle (4°), and were not ideal for isolating the C_{2q} term.

E_b (GeV)	Q^2 (GeV/c) ²	x	y	Y_3	$Y_3^{\text{simplified}}$	R_S	R_V	$Y_3^{\text{simplified}} R_V$
16.2	0.92	0.14	0.22	0.19	0.24	0.071 ± 0.014	0.623 ± 0.014	0.152
19.4	1.53	0.28	0.15	0.15	0.16	0.022 ± 0.005	0.859 ± 0.012	0.138
19.4	1.52	0.26	0.16	0.16	0.17	0.027 ± 0.006	0.836 ± 0.012	0.144
19.4	1.33	0.16	0.23	0.21	0.26	0.068 ± 0.012	0.671 ± 0.014	0.171
19.4	1.28	0.14	0.25	0.23	0.28	0.082 ± 0.013	0.630 ± 0.014	0.176
19.4	1.25	0.13	0.26	0.24	0.29	0.090 ± 0.013	0.608 ± 0.013	0.178
19.4	1.16	0.11	0.29	0.26	0.33	0.107 ± 0.013	0.563 ± 0.013	0.186
19.4	1.07	0.09	0.32	0.29	0.37	0.127 ± 0.014	0.518 ± 0.012	0.190
19.4	0.93	0.07	0.36	0.33	0.42	0.148 ± 0.017	0.471 ± 0.011	0.197
22.2	1.96	0.28	0.17	0.17	0.18	0.027 ± 0.005	0.860 ± 0.011	0.158
22.2	1.66	0.15	0.26	0.24	0.29	0.081 ± 0.012	0.654 ± 0.014	0.191

TABLE XXII: Kinematics for the SLAC E122 experiment. Values for E_b , Q^2 , x and y are from Ref. [9]. Values for R_S and R_V are calculated using the MSTW2008 [87] leading-order parameterization. The product $Y_3 R_V$ provides the lever arm for isolating the C_{2q} contribution to the asymmetry. We used $Y_3^{\text{simplified}}$ in line with the original publication [9].

Appendix B: Formalism for beam depolarization calculation

The beam depolarization was calculated using Eq.(9.11) of Ref. [80]:

$$D(\vec{p}_1, \vec{\zeta}_1) = \frac{k^2 [\psi_1 - \zeta_{1z}^2 (\psi_1 - \frac{2}{3}\psi_2)]}{(\epsilon_1^2 + \epsilon_2^2)\psi_1 - \frac{2}{3}\epsilon_1\epsilon_2\psi_2} \quad (\text{B1})$$

where $\epsilon_{1,2}$ are the energy of the electron before and after bremsstrahlung in unit of the electron mass $m_e c^2$, k is the bremsstrahlung photon energy in units of $m_e c^2$, $\vec{\zeta}$ is the polarization vector of the electron with $\zeta_{1z} = 1$ for longitudinally

polarized electrons, and $\psi_{1,2}$ are given in the “complete screening” limit by

$$\psi_1 = 4 \ln(111Z^{-1/3}) + 2 - 4f(Z) = 4[\ln(183Z^{-1/3}) - f(Z)], \quad (\text{B2})$$

$$\psi_2 = 4[\ln(183Z^{-1/3}) - f(Z)] - \frac{2}{3}. \quad (\text{B3})$$

The function $f(Z)$ is

$$f(Z) = a^2 \sum_{n=1}^{\infty} \frac{1}{n(n^2 + a^2)}, \quad (\text{B4})$$

with $a = (Ze^2/\hbar c)$.

The “complete screening” limit is defined as $\beta_i \xi / \delta \gg 1$ where $\beta_i = (Z^{1/3}/121)b_i$ with $b_1 = 6$, $b_2 = 1.2$ and $b_3 = 0.3$; $\xi \equiv 1/(1+u^2)$ with $u = p_1\theta_1$; and $\delta \equiv k/(2\epsilon_1\epsilon_2)$. Here \vec{p}_1, \vec{p}_2 are the momenta of the electron before and after bremsstrahlung in units of $m_e c$, and θ_1, θ_2 are the angles between \vec{p}_1, \vec{p}_2 and the photon \vec{k} , respectively. Because for high energy electrons θ_1 is very small, $u \approx 0$ and $\xi \approx 1$. Putting all notations together, the complete screening limit is

$$\frac{\beta_i \xi}{\delta} = \frac{\frac{Z^{1/3}}{121} b_i}{(1 + \epsilon_1^2 \theta_1^2) \frac{k}{2\epsilon_1\epsilon_2}} \approx \frac{\frac{Z^{1/3}}{121} b_i}{\frac{k}{2\epsilon_1\epsilon_2} + \frac{1}{2} k \theta_1^2} \gg 1 \quad (\text{B5})$$

where the approximation is valid if $k \ll \epsilon_1$ (which implies $\epsilon_1 \approx \epsilon_2$ and $k \ll \epsilon_2$) and the complete screening condition is satisfied if $\epsilon_{1,2} \gg 1$. For the 6-GeV beam used in this experiment, $\epsilon_1 \approx 12000$ and $k \ll \epsilon_1$, therefore the complete screening limit can be used.

Acknowledgments

The authors would like to thank the personnel of Jefferson Lab for their efforts which resulted in the successful completion of the experiment, and A. Accardi, P. Blunden, W. Melnitchouk and their collaborators for carrying out the calculations necessary for the completion of the data analysis. X. Zheng would like to thank the Medium Energy Physics Group at the Argonne National Lab for supporting her during the initial work of this experiment. The work of J. Erler was supported by PAPIIT (DGAPAUNAM) project IN106913 and CONACyT (México) project 151234, and he gratefully acknowledges the hospitality and support by the Mainz Institute for Theoretical Physics (MITP) where part of his work was completed. This work was supported in part by the Jeffress Memorial Trust under Award No. J-836, the U.S. National Science Foundation under Award No. 0653347, and the U.S. Department of Energy under Award No. DE-SC0003885 and DE-AC02-06CH11357. **Notice:** Authored by Jefferson Science Associates, LLC under U.S. DOE Contract No. DE-AC05-06OR23177. The U.S. Government retains a non-exclusive, paid-up, irrevocable, world-wide license to publish or reproduce this manuscript for U.S. Government purposes.

-
- [1] T.D. Lee and C.-N. Yang, Phys. Rev. **104**, 254 (1956).
 - [2] C.S. Wu *et al.*, Phys. Rev. **105**, 1413 (1957).
 - [3] S. L. Glashow, Nucl. Phys. **22**, 579 (1961).
 - [4] S. Weinberg, Phys. Rev. Lett. **19**, 1264 (1967).
 - [5] A. Salam, Conf. Proc. C **680519**, 367 (1968).
 - [6] F. J. Hasert *et al.*, Phys. Lett. B **46**, 121 (1973).
 - [7] F. J. Hasert *et al.* [Gargamelle Neutrino Collaboration], Nucl. Phys. B **73**, 1 (1974).
 - [8] C. Y. Prescott *et al.*, Phys. Lett. B **77**, 347 (1978).
 - [9] C. Y. Prescott *et al.*, Phys. Lett. B **84**, 524 (1979).
 - [10] R. D. Mckeown, Phys. Lett. B **219**, 140 (1989).
 - [11] R. Hasty *et al.* [SAMPLE Collaboration], Science **290**, 2117 (2000).
 - [12] D. T. Spayde *et al.* [SAMPLE Collaboration], Phys. Lett. B **583**, 79 (2004).
 - [13] T. M. Ito *et al.* [SAMPLE Collaboration], Phys. Rev. Lett. **92**, 102003 (2004).
 - [14] E. J. Beise, M. L. Pitt and D. T. Spayde, Prog. Part. Nucl. Phys. **54**, 289 (2005).
 - [15] F. E. Maas *et al.* [A4 Collaboration], Phys. Rev. Lett. **93**, 022002 (2004).
 - [16] F. E. Maas *et al.*, Phys. Rev. Lett. **94**, 152001 (2005).
 - [17] S. Baunack *et al.*, Phys. Rev. Lett. **102**, 151803 (2009).

- [18] K. A. Aniol *et al.* [HAPPEX Collaboration], Phys. Lett. B **509**, 211 (2001).
- [19] K. A. Aniol *et al.* [HAPPEX Collaboration], Phys. Rev. C **69**, 065501 (2004).
- [20] K. A. Aniol *et al.* [HAPPEX Collaboration], Phys. Rev. Lett. **96**, 022003 (2006).
- [21] K. A. Aniol *et al.* [HAPPEX Collaboration], Phys. Lett. B **635**, 275 (2006).
- [22] A. Acha *et al.* [HAPPEX Collaboration], Phys. Rev. Lett. **98**, 032301 (2007).
- [23] Z. Ahmed *et al.* [HAPPEX Collaboration], Phys. Rev. Lett. **108**, 102001 (2012).
- [24] D. H. Beck, Phys. Rev. D **39**, 3248 (1989).
- [25] D. S. Armstrong *et al.* [G0 Collaboration], Phys. Rev. Lett. **95**, 092001 (2005).
- [26] D. Androic *et al.* [G0 Collaboration], Phys. Rev. Lett. **104**, 012001 (2010).
- [27] S. Abrahamyan *et al.*, Phys. Rev. Lett. **108**, 112502 (2012).
- [28] C. J. Horowitz *et al.*, Phys. Rev. C **85**, 032501 (2012).
- [29] P.L. Anthony *et al.*, [SLAC E158 Collaboration], Phys. Rev. Lett. **95**, 081601 (2005).
- [30] A. Czarnecki and W.J. Marciano, Nature **435**, 437-438 (2005).
- [31] D. Androic *et al.* [Qweak Collaboration], Phys. Rev. Lett. **111**, 141803 (2013).
- [32] C.S. Wood *et al.*, Science **275**, 1759 (1997).
- [33] S.C. Bennett and C.E. Wieman, Phys. Rev. Lett. **82**, 2484 (1999) [Erratum-ibid. **83**, 889 (1999)].
- [34] J.S.M. Ginges and V.V. Flambaum, Phys. Rept. **397**, 63 (2004).
- [35] V.A. Dzuba, J.C. Berengut, V.V. Flambaum and B. Roberts, Phys. Rev. Lett. **109**, 203003 (2012).
- [36] E. D. Bloom and F. J. Gilman, Phys. Rev. Lett. **25**, 1140 (1970).
- [37] I. Niculescu *et al.*, Phys. Rev. Lett. **85**, 1186 (2000).
- [38] Y. Liang *et al.*, nucl-ex/0410027.
- [39] A. Psaker, W. Melnitchouk, M. E. Christy, and C. Keppel, Phys. Rev. C **78**, 025206 (2008).
- [40] S. P. Malace, Y. Kahn, W. Melnitchouk and C. E. Keppel, Phys. Rev. Lett. **104**, 102001 (2010).
- [41] S. P. Malace *et al.*, Phys. Rev. C **80**, 035207 (2009).
- [42] A. Airapetian *et al.* (HERMES Collaboration), Phys. Rev. Lett. **90**, 092002 (2003).
- [43] P. E. Bosted *et al.*, Phys. Rev. C **75**, 035203 (2007).
- [44] P. Solvignon *et al.*, Phys. Rev. Lett. **101**, 182502 (2008).
- [45] S. P. Malace, W. Melnitchouk, and A. Psaker, Phys. Rev. C **83**, 035203 (2011).
- [46] T. Navasardyan *et al.*, Phys. Rev. Lett. **98**, 022001 (2007).
- [47] C. E. Carlson and N. C. Mukhopadhyay, Phys. Rev. D **47**, 1737 (1993).
- [48] D. Wang *et al.* [PVDIS Collaboration], Nature **506**, no. 7486, 67 (2014).
- [49] D. Wang *et al.* [Jefferson Lab Hall A Collaboration], Phys. Rev. Lett. **111**, 082501 (2013).
- [50] R. N. Cahn and F. J. Gilman, Phys. Rev. D **17**, 1313 (1978).
- [51] L. T. Brady, A. Accardi, T. J. Hobbs and W. Melnitchouk, Phys. Rev. D **84**, 074008 (2011) [Erratum-ibid. D **85**, 039902 (2012)].
- [52] J. Beringer *et al.* (Particle Data Group), Phys. Rev. D **86**, 010001 (2012).
- [53] J. Alcorn *et al.*, Nucl. Instrum. Meth. A **522**, 294 (2004).
- [54] R. Subedi *et al.*, Nucl. Instrum. Meth. A **724**, 90 (2013).
- [55] C. K. Sinclair *et al.* Phys. Rev. ST Accel. Beams **10**, 023501 (2007); J. Hansknecht *et al.* Phys. Rev. ST Accel. Beams **13**, 010101 (2010).
- [56] K. D. Paschke, Eur. Phys. J. A **32**, 549 (2007).
- [57] J. Grames *et al.*, Accelerator Conference, New York, New York (2011).
- [58] W. Barry, Nucl. Instrum. Meth. A **301** (1991) 407; T. Powers, L. Doolittle, R. Ursic, and J. Wagner, Proc. 7th Workshop on Beam Instrumentation, AIP Conf. Proc. **390**, Ed. A. Lumpkin and C.E. Eyberger (1997); JLAB-TN-96-021.
- [59] J. S. Price *et al.*, In Protvino 1998, High energy spin physics 554-556
- [60] J. S. Price *et al.*, In Urbana 1997, Polarized gas targets and polarized beams 446.
- [61] J. S. Price *et al.*, prepared for Conference: C96-09-10, p.727 Proceedings.
- [62] M. Steigerwald, http://www.jlab.org/accel/inj_group/mott/mott.pdf
- [63] D. Neyret *et al.*, Nucl. Instrum. Meth. A **443**, 231 (2000).
- [64] M. Baylac *et al.*, Phys. Lett. B **539**, 8 (2002).
- [65] M. Friend *et al.*, Nucl. Instrum. Meth. A **676**, 96 (2012).
- [66] J. P. Jorda *et al.*, Nucl. Instrum. Meth. A **412**, 1 (1998).
- [67] N. Falletto *et al.* [HAPPEX Collaboration], Nucl. Instrum. Meth. A **459**, 412 (2001).
- [68] D. S. Parno *et al.*, Nucl. Instrum. Meth. A **728**, 92 (2013).
- [69] N. Liyanage, Optics Calibration of the Hall A High Resolution Spectrometers using the C Optimizer, JLab-TN-02-012, 2002.
- [70] P. E. Bosted and M. E. Christy, Phys. Rev. C **77**, 065206 (2008).
- [71] J. J. Aubert *et al.* [European Muon Collaboration], Phys. Lett. B **123**, 275 (1983).
- [72] J. Gomez *et al.*, Phys. Rev. D **49**, 4348 (1994).
- [73] S. Stein *et al.*, Phys. Rev. D **12**, 1884 (1975).
- [74] S. Rock and P. E. Bosted, Phys. Lett. B **518**, 34 (2001).
- [75] I. Sick and D. Day, Phys. Lett. B **274**, 16 (1992).
- [76] S. Malace, D. Gaskell, D. W. Higinbotham and I. Cloet, Int. J. Mod. Phys. E **23**, 1430013 (2014) [arXiv:1405.1270 [nucl-ex]].
- [77] S. Abrahamyan *et al.* [HAPPEX and PREX Collaborations], Phys. Rev. Lett. **109**, 192501 (2012).
- [78] A. Afanasev, priv. communication.
- [79] M. Seely, *Gas Chromatograph Analysis for Deuterium Sample*, July 26, 2002.

- [80] H. Olsen and L. C. Maximon, Phys. Rev. **114**, 887 (1959).
- [81] L. W. Mo and Y. -S. Tsai, Rev. Mod. Phys. **41**, 205 (1969).
- [82] R. Michaels, Formulas for Hall A Monte Carlo (2008), URL: http://hallaweb.jlab.org/parity/prex/hamc/hamc_formulas.pdf
- [83] D. Abbott *et al.* [JLAB t20 Collaboration], Eur. Phys. J. A **7**, 421 (2000).
- [84] S. J. Pollock, Phys. Rev. D **42**, 3010 (1990) [Erratum-ibid. D **43**, 2447 (1991)].
- [85] K. Matsui, T. Sato and T. -S. H. Lee, Phys. Rev. C **72**, 025204 (2005).
- [86] M. Gorchtein, C. J. Horowitz and M. J. Ramsey-Musolf, Phys. Rev. C **84**, 015502 (2011).
- [87] A. D. Martin, W. J. Stirling, R. S. Thorne and G. Watt, Eur. Phys. J. C **63**, 189 (2009).
- [88] M. Arneodo *et al.* [New Muon Collaboration], Phys. Lett. B **364**, 107 (1995).
- [89] N. L. Hall, P. G. Blunden, W. Melnitchouk, A. W. Thomas and R. D. Young, Phys. Rev. D **88**, 013011 (2013).
- [90] J. F. Owens, A. Accardi and W. Melnitchouk, Phys. Rev. D **87**, 094012 (2013).
- [91] J. Erler and S. Su, Prog. Part. Nucl. Phys. **71**, 119 (2013).
- [92] H. -L. Lai *et al.*, Phys. Rev. D **82**, 074024 (2010).
- [93] T. Hobbs and W. Melnitchouk, Phys. Rev. D **77**, 114023 (2008).
- [94] S. Alekhin, S. A. Kulagin and R. Petti, AIP Conf. Proc. **967**, 215 (2007).
- [95] J. D. Bjorken, Phys. Rev. D **18**, 3239 (1978).
- [96] L. Wolfenstein, Nucl. Phys. B **146**, 477 (1978).
- [97] S. Mantry, M. J. Ramsey-Musolf and G. F. Sacco, Phys. Rev. C **82**, 065205 (2010).
- [98] A. V. Belitsky, A. Manashov and A. Schafer, Phys. Rev. D **84**, 014010 (2011).
- [99] C. -Y. Seng and M. J. Ramsey-Musolf, Phys. Rev. C **88**, no. 1, 015202 (2013).
- [100] W. J. Marciano, Nature **506**, 43 (2014).
- [101] E. J. Eichten, K. D. Lane and M. E. Peskin, Phys. Rev. Lett. **50**, 811 (1983).
- [102] S. Schael *et al.* [ALEPH and DELPHI and L3 and OPAL and LEP Electroweak Collaborations], Phys. Rept. **532**, 119 (2013).